

Dissertation presented to the Instituto Tecnológico de Aeronáutica, in partial fulfillment of the requirements for the degree of Master of Science in the Graduate Program of Aeronautical and Mechanical Engineering, Field of Aeronautical Design, Aerospace Systems and Structures.

Gustavo Monteiro Farias

**A HIERARCHICAL RAYLEIGH-RITZ BASED
MODEL FOR AEROELASTIC ANALYSIS OF
WIND TURBINE BLADES**

Dissertation approved in its final version by signatories below:

Prof. Dr. Maurício Vicente Donadon

Advisor

Prof. Dr. Roberto Gil Annes da Silva

Co-advisor

Prof. Dr. Pedro Teixeira Lacava

Dean for Graduate Education and Research

Campo Montenegro
São José dos Campos, SP - Brazil
2018

Cataloging-in Publication Data
Documentation and Information Division

Farias, Gustavo Monteiro
A hierarchical Rayleigh-Ritz based model for aeroelastic analysis of wind turbine blades /
Gustavo Monteiro Farias.
São José dos Campos, 2018.
85f.

Dissertation of Master of Science – Course of Aeronautical and Mechanical Engineering. Area of Aeronautical Design, Aerospace Systems and Structures – Instituto Tecnológico de Aeronáutica, 2018. Advisor: Prof. Dr. Maurício Vicente Donadon. Co-advisor: Prof. Dr. Roberto Gil Annes da Silva.

1. Hierarchical Rayleigh-Ritz. 2. Aeroelastic analysis. 3. Wind turbine blades. I. Instituto Tecnológico de Aeronáutica. II. Title.

BIBLIOGRAPHIC REFERENCE

FARIAS, Gustavo Monteiro. **A hierarchical Rayleigh-Ritz based model for aeroelastic analysis of wind turbine blades**. 2018. 85f. Dissertation of Master of Science – Instituto Tecnológico de Aeronáutica, São José dos Campos.

CESSION OF RIGHTS

AUTHOR'S NAME: Gustavo Monteiro Farias

PUBLICATION TITLE: A hierarchical Rayleigh-Ritz based model for aeroelastic analysis of wind turbine blades.

PUBLICATION KIND/YEAR: Dissertation / 2018

It is granted to Instituto Tecnológico de Aeronáutica permission to reproduce copies of this dissertation and to only loan or to sell copies for academic and scientific purposes. The author reserves other publication rights and no part of this dissertation can be reproduced without the authorization of the author.

Gustavo Monteiro Farias
Av. Pio Corrêa Pinheiro, 651
14807-031 – Araraquara-SP

A HIERARCHICAL RAYLEIGH-RITZ BASED MODEL FOR AEROELASTIC ANALYSIS OF WIND TURBINE BLADES

Gustavo Monteiro Farias

Thesis Committee Composition:

Prof. Dr. Flavio Luiz Cardoso Ribeiro	Chairman	-	ITA
Prof. Dr. Maurício Vicente Donadon	Advisor	-	ITA
Prof. Dr. Roberto Gil Annes da Silva	Co-advisor	-	ITA
Prof. Dr. Antônio Bernardo Guimarães Neto	Internal examiner	-	ITA
Prof. Dr. Antônio Marcos Gonçalves de Lima	External examiner	-	UFU

Acknowledgments

Primeiramente gostaria de agradecer a minha mãe Adriana Monteiro por todo o suporte mesmo não estando fisicamente ao meu lado, pois sempre me incentivou e teve a paciência de me ouvir nos momentos mais difíceis.

Aos meus avós Monteiro e Solange, pois igual a minha mãe sempre me deram todo o apoio.

Ao meu tio Fábio Monteiro por ter me acolhido em sua casa e dado um suporte crucial nas etapas finais do mestrado.

Ao meu orientador professor Maurício Donadon, por sua paciência em discutir e me explicar assuntos complexos voltados a este trabalho.

Ao meu co-orientador professor Roberto Gil Annes da Silva por suas contribuições principalmente voltadas a modelagem aerodinâmica.

A todos os membros da banca pelas suas contribuições e comentários que ajudaram a melhorar este trabalho.

A todos os professores do ITA por quem eu tive a oportunidade de assistir suas aulas, aprendizado que vou levar durante toda a vida.

E não por último a todos os meus amigos que eu conheci em São José dos Campos, muito obrigado.

This work was financed by the national research council CNPq, Grant 301053/2016-2 and FINEP/CAPTAER II, Grant 0109020700.

Resumo

O presente trabalho propõe um modelo de Rayleigh-Ritz hierárquico para análise da resposta aeroelástica de pás de aerogeradores. A pá é modelada como uma viga em balanço, o modelo estrutural leva em consideração as pre-cargas induzidas pelas forças centrífugas e gravitacionais. A formulação é baseada no princípio de Hamilton combinado com o método de Rayleigh-Ritz. Um modelo aerodinâmico não estacionário é utilizado para calcular o incremento das forças aerodinâmicas no domínio da frequência utilizando as funções de Theodorsen e Loewy. A solução resultante de um problema de autovalor é baseado no método PK. A ocorrência do *flutter* aeroelástico é observada nos diagramas $\Omega - \omega$ e $\Omega - g$ em função da rotação das pás e da velocidade do vento. Os resultados numéricos previstos utilizando o modelo semi-analítico proposto foram comparados com resultados numéricos reportados na literatura para a pá projetada por Sandia National Laboratories, confeccionada em fibra de vidro e de 100 metros de comprimento. No geral uma boa concordância entre as previsões obtidas utilizando o modelo proposto e os resultados reportados na literatura foi obtida.

Abstract

The present work presents a hierarchical Rayleigh-Ritz based model to analyze the aeroelastic response of wind turbine blades. The blade is modeled as a cantilever beam, its structural model takes into account the pre-stress loads induced by centrifugal and gravitational forces. The formulation is based on the Hamilton's principle combined with the Rayleigh-Ritz method. An unsteady aerodynamic model is used to calculate the incremental aerodynamic forces in the frequency domain using Theodorsen's and Loewy's formulations. The solution of the resultant eigenvalue problem is based on the PK method. The occurrence of aeroelastic flutter is observed in $\Omega - \omega$ and $\Omega - g$ by varying the blade rotation and wind velocity. Numerical predictions obtained using the proposed semi-analytical model have been compared with numerical results reported in the literature for the Sandia 100-meter glass made wind turbine blade. An overall good agreement between predictions obtained using the proposed model and results reported in the open literature is found.

List of Figures

FIGURE 2.1 – The three blade regions (SCHUBEL; CROSSLEY, 2012).	21
FIGURE 2.2 – Representative airfoil cross section with two shear webs (GRIFFITH; ASHWILL, 2011).	22
FIGURE 2.3 – Typical modern HAWT blade with multiple airfoil profiles, twist and linear chord length increase (SCHUBEL; CROSSLEY, 2012).	23
FIGURE 3.1 – Simplified schematics of a rotating wind turbine blade and the acting forces.	28
FIGURE 3.2 – Flowchart explaining the PK method adapted to a rotating wing. . .	46
FIGURE 4.1 – Mode shapes of the SNL 100-00 blade due centrifugal loads.	49
FIGURE 4.2 – Aeroelastic prediction of SNL100-00 blade using Theodorsen func- tion in rotation only.	51
FIGURE 4.3 – Aeroelastic prediction of SNL100-00 blade using Theodorsen func- tion with $V_\infty = 10$ m/s.	52
FIGURE 4.4 – Aeroelastic prediction of SNL100-00 blade using Theodorsen func- tion with $V_\infty = 20$ m/s.	53
FIGURE 4.5 – Aeroelastic prediction of SNL100-00 blade using Loewy function with $V_\infty = 10$ m/s.	55
FIGURE 4.6 – Aeroelastic prediction of SNL100-00 blade using Loewy function with $V_\infty = 20$ m/s.	56
FIGURE 4.7 – Theodorsen’s and Loewy’s function with different μ ’s and γ ’s. . . .	57
FIGURE 5.1 – Simplified dynamic model of a gas turbine rotor, (DONADON <i>et al.</i> , 2010).	58
FIGURE 5.2 – Bending modes.	60

FIGURE 5.3 – Half-wing with a ballast on the tip.	61
FIGURE 5.4 – Flowchart explaining the PK method for a fixed wing.	67
FIGURE 5.5 – Modes.	68
FIGURE 5.6 – Aeroelastic prediction of the half-wing where $d_{\text{offset}} = -5$ mm.	70
FIGURE B.1 – Inertial and mass properties.	78
FIGURE B.2 – Geometric properties.	79
FIGURE B.3 – Planform of Sandia 100-m Baseline Blade with Laminate Designations (Blue: Spar Cap, Orange: trailing edge reinforcement, Red: Third Shear Web).	79
FIGURE C.1 – Geometric shape of the SNL100-00 blade.	82
FIGURE C.2 – Reynolds number.	83
FIGURE C.3 – Mach number.	85
FIGURE C.4 – Curve slopes.	85

List of Tables

TABLE 4.1 –	Modal frequencies of the SNL 100-00 blade with different blade angle position.	47
TABLE 4.2 –	Modal frequencies of the SNL 100-00 blade in the position of 0 rad.	48
TABLE 4.3 –	Flutter speed comparison with other authors.	50
TABLE 5.1 –	Material properties of the cantilever beam.	59
TABLE 5.2 –	$\Omega = 0$ rpm.	59
TABLE 5.3 –	$\Omega = 9550$ rpm	60
TABLE 5.4 –	Material and geometric properties of the half-wing and ballast.	61
TABLE 5.5 –	Frequency response for each mode.	68
TABLE 5.6 –	Aeroelastic results.	69
TABLE B.1 –	Laminate Schedule for Sandia 100-m Baseline Blade (* indicates termination)	80
TABLE B.2 –	Materials Usage Summary for Sandia 100-m Baseline Blade.	81
TABLE B.3 –	Bill of Materials for Sandia 100-m Baseline Blade.	81
TABLE B.4 –	General SNL wind turbine properties.	81
TABLE C.1 –	Parameters of the air.	82
TABLE C.2 –	Sandia 100-m Baseline Blade Airfoil and Chord Properties.	84

List of Abbreviations and Acronyms

BEMT	Blade Element Momentum Theory
BLAST	BLade Aeroelastic Stability Tool
BTC	Bend-Twist Coupling
HAWT	Horizontal Axis Wind Turbine
NREL	National Renewable Energy Laboratory
SNL	Sandia National Laboratories

List of Symbols

β	Local twist around x -axis
ΔV_{∞}^+	Increment of wind speed
$\Delta \Omega^+$	Increment of rotation speed
Γ	Warping constant
γ	Vertical distance between successive rows of vorticity
λ	Eigenvalue
\mathbf{B}	Aerodynamic damping matrix
\mathbf{C}	Aerodynamic stiffness matrix
\mathbf{D}	Structural damping matrix
\mathbf{I}	Identity matrix
\mathbf{K}_{β_1}	Torsional stiffness matrix
\mathbf{K}_{β_2}	Warping stiffness matrix
\mathbf{K}_p	Pre-load stiffness matrix
$\mathbf{K}_{u,w}$	Axial and bending stiffness matrix
\mathbf{M}_{β}	Torsional mass matrix
$\mathbf{M}_{u,w}$	Axial and bending mass matrix
\mathcal{A}_{β}	Rayleigh-Ritz coefficients vector associated with twist displacement field
\mathcal{A}_u	Rayleigh-Ritz coefficients vector associated with axial displacement field
\mathcal{A}_w	Rayleigh-Ritz coefficients vector associated with bending displacement field

\mathcal{B}	Vector of uncoupled modes in twisting
\mathcal{F}	Real Part of Theodorsen/Loewy Function
\mathcal{G}	Imaginary Part of Theodorsen/Loewy Function
\mathcal{H}	Third order Bessel function or Hankel function
\mathcal{J}	First order Bessel function
\mathcal{N}	Vector of linear dependent shape functions
\mathcal{V}	Displacement field of interest
\mathcal{W}	Vector of uncoupled modes in bending
\mathfrak{m}	Number of bending modes
\mathfrak{n}	Number of torsion modes
μ	Frequency ratio
Ω	Rotation speed
ω	Flutter/vibration frequency
ϕ_β	Harmonic coefficients vector associated with twist displacement field
ϕ_u	Harmonic coefficients vector associated with axial displacement field
ϕ_w	Harmonic coefficients vector associated with bending displacement field
Π_P	Total potential energy
ρ_f	Fluid density
ρ_{st}	Structural density
σ	Stress
$\theta(x, t)$	Pitch function in time and space domain
$\underline{\theta}_i(t)$	Heave function in the time domain related to the bending mode of interest
$\underline{h}_i(t)$	Pitch function in the time domain related the torsion mode of interest
\underline{q}	Vector of heave and pitch functions in the time domain
Υ	Wake weighting function

ε_L	Linear strain
ε_{NL}	Non-linear strain
φ	Angle position of the wind turbine blade in relation to the rotor
$\xi(x)$	Non-dimensional coordinate
ζ	Damping ratio
A	Blade cross-section area
a	Nondimensional distance from the midchord to the elastic axis, positive rearward, fraction of semi-chord b
$a.a$	Aerodynamic axis
$a_{c,n}$	Nondimensional distance from the midchord to the local aerodynamic center, positive rearward, fraction of semi-chord b
b	Semi-chord
b_{hw}	Width of the half-wing
C	Theodorsen's lift deficiency function
C'	Loewy's lift deficiency function
$c.g$	Center of gravity
c_h	Heave structural damping
c_θ	Pitch structural damping
$c_{l,\alpha}$	Local lift curve slope
d_{offset}	Distance from the center line of the half-wing
E	Elastic modulus
$e.a$	Elastic axis
$f_i^\theta(x)$	Pitch function in the space domain related the torsion mode of interest
$f_i^h(x)$	Heave function in the space domain related to the bending mode of interest
F_c	Centrifugal force
$f_\theta(x)$	Pitch function in the space domain

F_{gx}	Gravitational force acting on z -axis
F_{gy}	Gravitational force acting on y -axis
$f_h(x)$	Heave function in the space domain
G	Shear modulus
g	Gravity
$h(x, t)$	Heave function in time and space domain
h_{hw}	Thickness of the half-wing
I	Second moment of area
I_θ	Polar moment of inertia
I_θ^{bl}	Polar moment of inertia of the ballast
J	Saint-Venant torsional constant
j	Current linear dependent shape function
k	Reduced frequency, $\frac{\omega b}{V_{rel}}$
L	Lift
L_e	Blade length
L_{hw}	Length of the half-wing
M	Moment
m	Structural linear mass
m_{bl}	Mass of the ballast
n	Total number of shape functions
N_{bl}	Number of blades
R	Rotor radius
R_0	Hub radius
s	Twice the number of all modes
S_{sc}	Static mass moment per unit span about the elastic axis

S_{sc}^{bl}	Static mass moment of the ballast
t	Time
T_β	Torsional kinetic energy
$T_{u,w}$	Axial and bending kinetic energy
$T_{w,\beta}$	Bend and twist kinetic energy
u, v, w	Displacements in x, y, z axis
U_β	Torsional strain energy
U_p	Pre-load strain energy
$U_{u,w}$	Axial and bending strain energy
$U_{w,\beta}$	Bend and twist strain energy
V	Volume
V_D	Damping kinetic energy
V_∞	Free-stream velocity
V_{rel}	Relative velocity
W_p	External work
W_{NC}	Non-conservative work

Subscripts

$_{,x}$	Spatial derivative, $\frac{\partial}{\partial x}$
---------	---

Superscripts

\cdot	Time derivative, $\frac{\partial}{\partial t}$
$*$	Total displacement

Contents

1	INTRODUCTION	18
1.1	Background	18
1.2	Motivation	19
1.3	Objectives	19
1.4	Dissertation structure	19
2	OVERVIEW OF WIND TURBINE BLADES	21
2.1	Typical wind turbine blade	21
2.2	Wind turbine blade loads	24
2.3	Aeroelasticity of wind turbine blades	24
3	WIND TURBINE BLADE MODEL	27
3.1	Structural model formulation	27
3.1.1	Inclusion of stress stiffening effects on the wind turbine blade	27
3.1.2	Axial-bending vibration model with pre-stress	32
3.1.3	Torsional vibration model	34
3.2	Unsteady aerodynamic model formulation	36
3.3	Aeroelastic model formulation	39
4	RESULTS AND DISCUSSION	47
4.1	Modal analysis	47
4.2	Aeroelastic analysis using Theodorsen's function	50
4.3	Aeroelastic analysis using Loewy's function	54
5	OTHER APPLICATIONS	58

5.1	Gas turbine blade	58
5.1.1	Modal analysis	59
5.2	Half plate like wing with a ballast on the tip	60
5.2.1	Bending vibration model	61
5.2.2	Torsional vibration model	62
5.2.3	Unsteady aerodynamic model formulation	63
5.2.4	Aeroelastic model formulation	65
5.2.5	Modal analysis	68
5.2.6	Aeroelastic analysis	69
6	CONCLUSION	71
6.1	Future works	72
BIBLIOGRAPHY		73
APPENDIX A – HIERARCHICAL FUNCTIONS		77
APPENDIX B – BLADE INFORMATION		78
APPENDIX C – BLADE AIRFOIL SECTIONS CURVE SLOPE		82

1 Introduction

1.1 Background

In recent years the trend of large wind turbine rotors for wind energy harvesting, has driving aeroelastic instability as a discussing issue in the design. In the current scenario, aeroelastic instabilities are rarely observed on wind turbine blades, but as the wind turbine rotor increases more flexible the blades become due to the increase of material weight and lower stiffness, which are factors that may cause flutter. The classical flutter occurs as a result of the interaction between aerodynamic, inertial and structural forces acting on the structure in association with motion of two modes in vibration causing the modes to couple in unfavorable manner (BISPLINGHOFF *et al.*, 1955; FUNG, 1969; WRIGHT; COOPER, 2015). The coupled-mode flutter is a major problem in the aircraft industry that can lead fatigue damage and catastrophic failure. In the case of a wind turbine blades, the coupling between bend and twist modes in the flutter regime can result in negative angles of attack due oscillations while it is twisting, which may induce a local opposing lift that decelerate the blades rotation, and also can lead to high angles of attack inducing local stall (LARWOOD *et al.*, 2001). Those effects can reduce the energy harvested by the wind turbine (RAFIEE *et al.*, 2016), but studies have revealed that the bend-twist coupling effect can act as a passive mechanism for the blade to self-alleviate the higher aerodynamic loads and prevent damage on the structure (BOTTASSO *et al.*, 2012; FARSADI; KAYRAN, 2016; HAYAT *et al.*, 2016). Another concern is about the nature of a rotating blade wake, because the shed vorticity of a blade in revolution could actually influence the flow seen by all the rotor blades depending on the rotation and the wind velocity, this effect is shown in the work of (LOEWY, 1957) and it has been accounted for in the aeroelastic modeling approaches developed by several researchers in last years (FILIPPI; CARRERA, 2015; SICARD; SIROHI, 2016). Most of recent studies about the aeroelastic response of wind turbine blades does not compute the wake effect in the analysis, so no influence from shed vorticity of rotating blades is considered and the blade essentially encounter a still air flow in its analysis.

1.2 Motivation

The main motivation of this work is the continuous increase of MW-sized wind turbine blades, which is well discussed in the literature that as larger the wind turbine gets more energy can be harvested from the wind. Ultimately MW-sized wind turbine blades have been pitch controlled, using actuators at the blade root (SCOTT *et al.*, 2017). However new concepts have been under investigation to mitigate fatigue loads in larger blades by introducing a bend-twist coupling (BTC) which acts as a passive control (LOBITZ; LAINO, 1999; BOTTASSO *et al.*, 2012; HAYAT; HA, 2015). The structural BTC describes a coupled behavior between bending and torsional deformations of a beam-like structure: the bending deformation imposed by a bending moment will induce a torsional twist. A wind turbine blade possessing the structural BTC feature is called an adaptive blade. The practice of achieving the desired structural BTC effect by modifying the anisotropic mechanical properties of a structure to control an aeroelastic deformation, is known as aeroelastic tailoring. Under the influence of aerodynamic loads, the adaptive blade twists as it bends, causing a change in the angle of attack, thus directly altering wind-induced loads (GOEIJ *et al.*, 1999).

Higher structural BTC is desirable as it makes possible the greatest fatigue load reduction (HAYAT; HA, 2015). However, it may also increase the risk of dynamic instabilities as classical flutter and related to this issue the present work contribution takes place.

1.3 Objectives

- The main objective is to present a model to predict the aeroelastic flutter of a wind turbine blade.
- Validate the model with the Sandia 100-meter all-glass baseline wind turbine blade (GRIFFITH; ASHWILL, 2011).
- Show the application and capabilities of the proposed hierarchical Rayleigh-Ritz method to predict the modal and aeroelastic response of typical rotating and fixed plate-like wings.

1.4 Dissertation structure

The dissertation has been divided into 6 chapters. The first is the introduction in Chapter 1 and the second is an overview of wind turbine blades in Chapter 2 to provide more background for a critical view of the reader in the following chapters.

Chapter 3 presents the proposed aeroelastic model formulation for a single wind turbine blade.

The results are presented in Chapter 4. The first part of the chapter presents a detailed modal analysis performed using the proposed model comparing the model predictions with results available in the open literature for the SNL 100-00 wind turbine blade. These analyses are followed by aeroelastic analyses where the rotation-damping and rotation-frequency diagrams are shown in order to define the flutter and divergence velocities for the SNL 100-00 wind turbine blade.

In Chapter 5 two other applications of the proposed model are presented, one is the modal analysis of a gas turbine blade and the second application consists of an aeroelastic and modal analysis of a half-wing with a ballast in the tip, both applications use the same hierarchical Rayleigh-Ritz method used in the SNL 100-00 blade.

Finally the conclusions and future works are presented in Chapter 6.

2 Overview of wind turbine blades

This chapter presents briefly some important concepts and definitions about wind turbine blades. Issues regarding topology, airfoil selection, material composition, loads on the blade are presented and discussed. Additionally, comments regarding aeroelasticity of wind turbine blades which is the focus of this work are also presented and discussed.

2.1 Typical wind turbine blade

The conventional HAWT blade can be divided into three main areas classified by the most requested aerodynamic and structural properties along the length, as show on Fig. 2.1 (SCHUBEL; CROSSLEY, 2012).

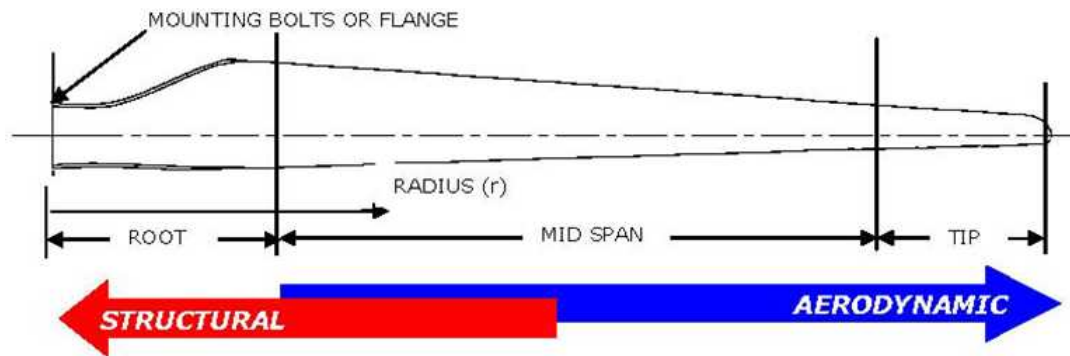


FIGURE 2.1 – The three blade regions (SCHUBEL; CROSSLEY, 2012).

The blade root is the transition between the circular mount and the first airfoil, this section carries the highest loads and from the transition it typically consists of thick airfoil sections with low aerodynamic efficiency. The mid span which is more aerodynamically significant, uses the thinnest possible airfoil sections that the blade structure allows. The tip which is the most critical region regarding aerodynamic performance, uses slender airfoils and specially designed tip geometries to reduce noise and losses.

As describe in (MANWELL *et al.*, 2009), the basic shape and dimensions of the blades are determined primarily by the overall topology of the turbine and the aerodynamic characteristics. Details in the shape, particularly near the root, are also influenced by

structural considerations. For example, the planform of most real wind turbines differs significantly from the optimum shape, because the costs associated with blade manufacturing would otherwise be too high. Material characteristics and available methods of fabrication are also particularly important in deciding upon the exact shape of the blades.

A typical wind turbine blade cross section is shown in Fig. 2.2. As shown in the figure, an interior spar provides the interior strength, primarily via forward and aft shear webs. Spar caps transfer loads from the outer skin to the shear webs. In order to provide sufficient strength, particularly near the root of the blade, inboard sections are relatively thick. Wind turbine blades frequently do not have just one airfoil shape along the entire length, for example Fig. 2.3. More commonly (but not always), the airfoils are all of the same family, but the relative thickness varies. Thicker airfoils near the root provide greater strength, and can do so without seriously degrading the overall performance of the blade.

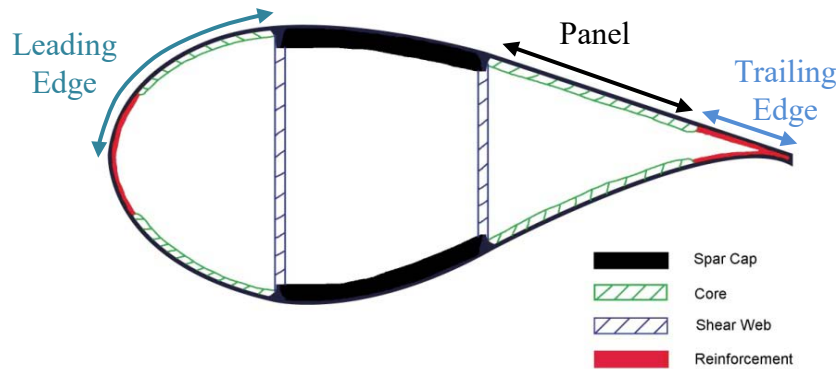


FIGURE 2.2 – Representative airfoil cross section with two shear webs (GRIFFITH; ASHWILL, 2011).

With the increasing advances on manufacturing techniques it is generally advantageous to have as few blades as possible. This is primarily because of the fixed costs in fabricating the blades. In addition, when there are more blades (for a given solidity) they will be less stiff and may have higher stresses at the roots. Solidity is the area of the rotor in the plane of rotation divided total swept area of the rotor. Currently all commercial wind turbines have either two or three blades. Two-bladed wind turbines have historically had a lower solidity than three-bladed machines. This keeps the blade cost low, which is one of the presumed advantages of two blades over three blades.

The method of power control (stall or variable pitch) has a significant effect on the design of the blades, particularly in regard to the choice of the airfoil. A stall-controlled turbine depends on the loss of lift which accompanies stall to reduce the power output in high velocity wind conditions. It is highly desirable that the blades have good stall characteristics. They should stall gradually as the wind velocity increases, and they should be relatively free of transient effects, such as are caused by dynamic stall. In pitch-controlled turbines, stall characteristics are generally much less important. On the other

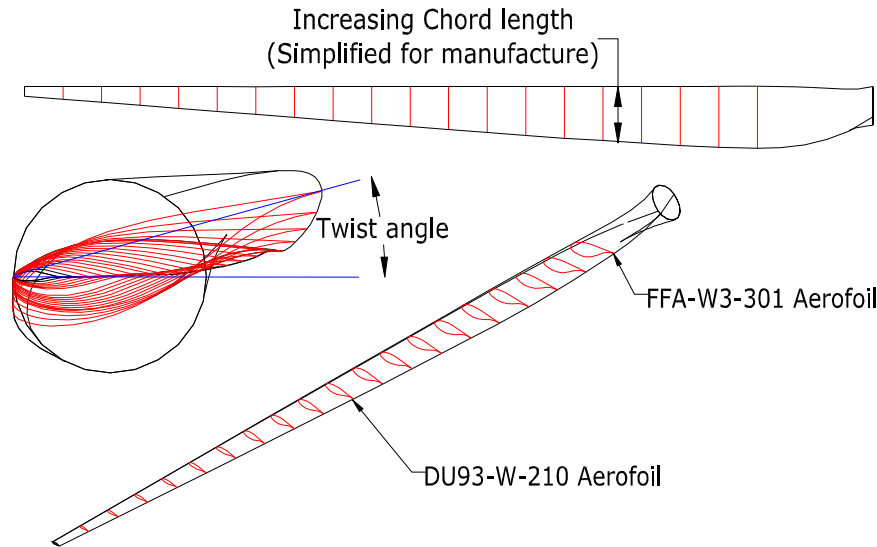


FIGURE 2.3 – Typical modern HAWT blade with multiple airfoil profiles, twist and linear chord length increase (SCHUBEL; CROSSLEY, 2012).

hand, it is important to know that the blades perform acceptably when being pitched in high velocity wind conditions. It is also worth noting that blades can be pitched towards either feather (decreasing angle of attack) or stall (increasing angle of attack).

The rotor orientation with respect to the tower has some effect on the geometry of the blades, but mostly in a secondary manner related to the preconing of the blades. This preconing is a tilting of the blades away from a plane of rotation. Most downwind turbines have historically operated with free yaw. The blades then must be coned away from the plane of rotation to enable the rotors to track the wind and maintain some yaw stability. Some upwind rotors also have preconed blades. In this case, the preconing is in the upwind direction and the purpose is to keep the blades from hitting the tower.

Properties of the overall blade, such as total weight, stiffness, and mass distributions, and moments of inertia are needed in the structural analysis of the rotor. Important concerns from the blades are the strength, tendency to deflect under load, natural vibration frequencies, and resistance to fatigue. Some of the blade properties can be difficult to obtain due to the complex geometry of the blade, which varies from root to tip. The usual method used is to divide the blade into sections, the properties for each section are found, based on the dimensions and material distribution, and then combined to find values for the entire blade.

For the current work the blade structure and aerodynamic properties are given in Appendices B and C.

2.2 Wind turbine blade loads

Under operational scenarios the main sources of blade loading are aerodynamic, gravitational, centrifugal, gyroscopic and operational loads (BURTON *et al.*, 2001).

Aerodynamic loads are unavoidable and vital to the function of the turbine. Aerodynamic load is generated by lift and drag of the blades airfoil section, which is dependent on wind velocity, blade velocity, surface finish, angle of attack and yaw. The angle of attack is dependent on blade twist, pitch and wind flow direction. The aerodynamic lift and drag produced are converted into useful thrust in the direction of rotation which is imparted to the generator, powertrain and reaction forces on the blade. The reaction forces act substantially in the flapwise bending plane, and must be resisted by the blade with limited deformation.

Gravitational and centrifugal forces are mass dependent which is generally thought to increase cubically with increasing turbine diameter (BRØNDSTED *et al.*, 2005). Therefore, turbines under ten meters diameter have negligible inertial loads, which are marginal for 20 meters upward, and critical for 70 meter rotors and above (BRØNDSTED *et al.*, 2005). The gravitational force is defined simply as mass multiplied by the gravitational constant, although its direction remains constant acting towards the center of the earth which causes an alternating cyclic load case. The centrifugal force is a product of rotational velocity squared, radius, mass and always acts radial outward, hence the increased load demands of higher tip speeds. Centrifugal and gravitational loads are superimposed to give a positively displaced alternating condition with a wavelength equal to one blade revolution.

Gyroscopic loads result from yawing during operation. They are system dependent and generally less intensive than gravitational loads. Operational loads are also system dependent, resulting from pitching, yawing, braking, generator load torque and can be intensive during emergency stop or grid loss scenarios (SCHUBEL; CROSSLEY, 2012). Gyroscopic and operational loads can be reduced by adjusting system parameters. Blades which can withstand aerodynamic, gravitational and centrifugal loads are generally capable of withstanding these reduced loads (SCHUBEL; CROSSLEY, 2012). Therefore, gyroscopic and operational loads are not considered within this work.

2.3 Aeroelasticity of wind turbine blades

Higher energy extraction from wind turbine systems requires larger turbines, with blade sizes over 100 m and associated with optimized structural and mechanical components to accomplish improved stiffness, increased fatigue life, and reliability. To attain

these goals, loads that occur due to the aeroelastic effects on the wind turbine blades must be reduced. This can also be achieved passively by using the anisotropy of composite materials. The anisotropic behavior of composite materials has led to new concept blades with aeroelastic tailoring as a passive control mechanism. The passive control mechanism is called bend-twist coupling (BTC). As the name suggests, BTC creates a coupling between bending and twist of the blade. The coupling links the aerodynamic forces, which induce bending in the blade, with the twist of the blade. The twist of the blade in turn changes the angle of attack and thereby the aerodynamic forces. This feedback loop, when twisting towards a lower angle of attack, enables the blade to self-alleviate sudden inflow changes, as in gusty or turbulent conditions, leading to a reduction in ultimate and fatigue loads. However, the phase difference between the deformations of the structure and the aerodynamic loads causes energy absorption by the structure from the air. The energy transmission from aerodynamic loads to the structure may result in oscillations with growing amplitude. The worst case scenario is the failure of the structure due classical flutter.

Classical flutter is a dynamic aeroelastic instability generated by the coupling of torsion and flapwise bending deformations. When classical flutter arises, time response grows exponentially till failure. Classical flutter is well known in aerospace and civil engineering. Occurrence of the classical flutter event has not been reported for commercial wind turbine so far. With an increase in length of wind turbines blade in the future wind turbines, it is more likely to happen (LOBITZ, 2004).

For large wind turbines blade in low angle of attacks and attached flow, the classical flutter becomes a serious problem. It is recommended by (HANSEN *et al.*, 2006) to include classical flutter calculations in the preliminary design for 50 m blades and above due to decrease in the flapwise and the torsional stiffness.

Obtaining accurate and efficient aerodynamic models has been an important goal of research efforts in wind turbine industry over the past years. Aerodynamic models are necessary to design the wind turbine blade, to evaluate aeroelastic stability and the response. The unsteady aerodynamics provides a good level of accuracy in prediction of the flutter rotational speeds of the wind turbine blade when the correct models with both circulatory and non-circulatory components on the aerodynamic forces computations are employed. Among the wide range of unsteady aerodynamic models in the literature the classical models of Theodorsen in frequency domain and its time domain counterpart, indicial aerodynamics remain widely used and provide a benchmark for the linear models both in fixed and rotating blades. Several studies have been conducted with the use of these approaches to investigate the aeroelastic characteristics of the wind turbine blades (RESOR *et al.*, 2012; OWENS *et al.*, 2013; POURAZARM *et al.*, 2016).

For the current work it is introduced a Rayleigh-Ritz method to perform a modal

analysis in the wind turbine blade accounting for pre-stress stiffening effects and extract its eigenvalues and eigenvectors to be use in the aeroelastic analysis. The method is based in hierarchical polynomial function presented in the work of (BARDELL, 1991), which has been recently employed in the free vibration and aeroelastic analyses of hybrid stiffened composite panels by (de MATOS JUNIOR *et al.*, 2017). In this work the wind turbine blade is considered as a cantilever beam with a gravitational and centrifugal forces acting along its span as non-linear terms. The unsteady aerodynamic loads are included into the formulation by using Theodorsen and Loewy formulations, and comparisons of the results evidence the relevance of taking the vortex shedding into account in aeroelastic analyses of rotating blades. The model is employed to predict the aeroelastic response of the Sandia 100-meter all-glass baseline wind turbine blade SNL100-00, developed by (GRIFFITH; ASHWILL, 2011). The first aeroelastic analysis of the current blade was developed by (RESOR *et al.*, 2012) for a 1.5 MW rotor blade using a tool present in the work of (LOBITZ, 2004), which was firstly designed to analyze the aeroelastic instability of vertical axis wind turbine blades in the work of (LOBITZ; ASHWILL, 1986). (RESOR *et al.*, 2012) considered constant the semi-chord, the aerodynamic center and the elastic center along the blade span in its unsteady aerodynamic model and they found a flutter condition at 9.37 rpm which is 1.27 times the operational velocity of the wind turbine. (OWENS *et al.*, 2013) have also carried out further analyses in the SNL100-00 blade, using the BLade Aeroelastic Stability Tool (BLAST), which is an extension tool used in the work of (LOBITZ, 2004) and (RESOR *et al.*, 2012), and they found a critical rotor angular speed around 13 rpm. More recently (POURAZARM *et al.*, 2016) carried out parametric aeroelastic analyses in the SNL100-00 blade using the Galerkin method based in the equations originally derived by (HODGES; DOWELL, 1974) and found a critical flutter angular velocity of 16.91 rpm.

Within this context, as an alternative to (RESOR *et al.*, 2012; OWENS *et al.*, 2013; POURAZARM *et al.*, 2016), this work presents a semi-analytical model based on the hierarchical finite element formulation to predict the aeroelastic stability of the Sandia 100-meter all-glass baseline wind turbine blade SNL100-00.

3 Wind turbine blade model

This chapter describes the structural, aerodynamic and aeroelastic model formulations. First is shown how to compute and include the stress stiffening effect due to rotation and position of the blade in a structural dynamic model. Subsequently an unsteady aerodynamic model using the approach of (WRIGHT; COOPER, 2015) where they reduce the complex form of Theodorsen's into the lift and moment equations to real coefficients, considering the $C_{l,\alpha}$ and the offset of the aerodynamic center describe by (YATES Jr, 1966). Finally, a solution method based on a modified version of the PK method is presented in order to take into account the blade rotational velocity.

3.1 Structural model formulation

This section presents how to include the stress stiffening effect in the bending vibration model of the wind turbine blade, well as the torsional vibration model which composes the structural dynamic model. The frequencies and mode shapes obtained from the bending and torsion vibration problems will be use afterwards in the aeroelastic model.

3.1.1 Inclusion of stress stiffening effects on the wind turbine blade

The total potential energy for a single blade can be written in terms of the blade strain energy (U_p) and the work done by the external load (W_p) as follows,

$$\Pi_P = U_p - W_p \quad (3.1)$$

where the blade is idealized as a rotating beam with symmetrical cross-section and no pre-twist (Fig. 3.1). The problem is solved as a uncoupled manner and the displacement field is computed in a 2D plane x - y local coordinates of the blade to compute the effect of the gravitational force, as the centrifugal force as shown on Fig. 3.1 then,

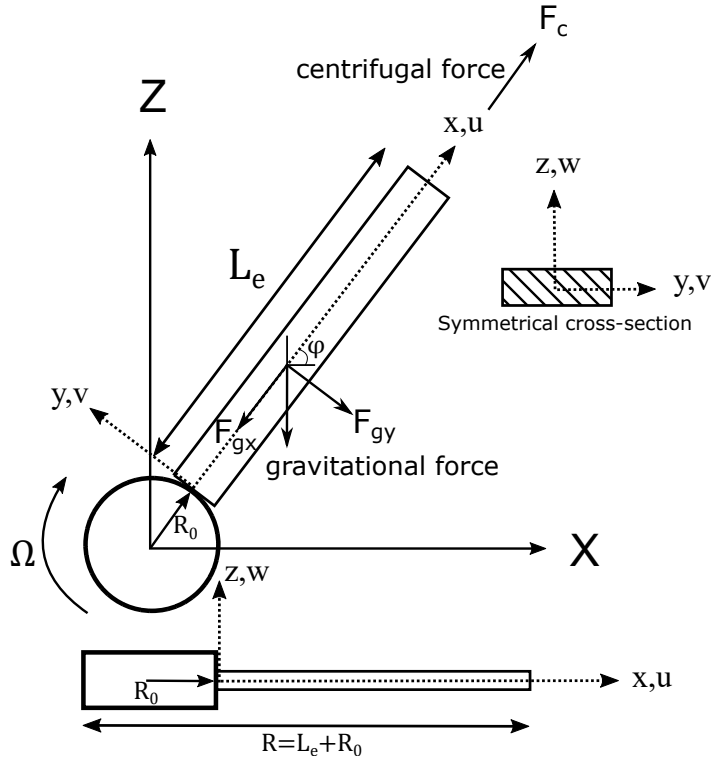


FIGURE 3.1 – Simplified schematics of a rotating wind turbine blade and the acting forces.

$$\begin{aligned}
 U_p &= \frac{1}{2} \int_V (\varepsilon_L + \varepsilon_{NL}) \sigma dV = \frac{1}{2} \int_V (\varepsilon_L + \varepsilon_{NL}) E (\varepsilon_L + \varepsilon_{NL}) dV \\
 &= \frac{1}{2} \int_V E (\varepsilon_L)^2 dV + \int_V E \varepsilon_{NL} \varepsilon_L dV + \frac{1}{2} \int_V E (\varepsilon_{NL})^2 dV
 \end{aligned} \tag{3.2}$$

where $\sigma = E(\varepsilon_L + \varepsilon_{NL})$ and for moderate displacements $(\varepsilon_{NL})^2$ is too small, then it is neglected. The external loads acting on the plane are,

$$\begin{aligned}
 W_p &= \int_{R_0}^R F_c u dx + \int_{R_0}^R F_{gx} u dx + \int_{R_0}^R F_{gy} v dx \\
 &= \int_{R_0}^R A \rho_{st} \Omega^2 x u dx - \int_{R_0}^R g \rho_{st} A \sin \varphi u dx + \int_{R_0}^R g \rho_{st} A \cos \varphi v dx
 \end{aligned} \tag{3.3}$$

The kinematic relationship are defined based on the Euler-Bernoulli beam theory given as follows,

$$u^* = u + y \frac{\partial v}{\partial x}; \quad v^* = v; \quad \varepsilon_L = \frac{\partial u^*}{\partial x} = \frac{\partial u}{\partial x} + y \frac{\partial^2 v}{\partial x^2}; \quad \varepsilon_{NL} = \frac{1}{2} \left(\frac{\partial v}{\partial x} \right)^2 \tag{3.4}$$

Replacing the kinematic assumptions given by Eq. (3.4) into Eq. (3.2), and assuming symmetry along the y -direction, the strain energy can be written as follows,

$$\begin{aligned}
 U_p = & \frac{1}{2} \int_{R_0}^R E \left(\int_A dA \right) \left(\frac{\partial u}{\partial x} \right)^2 dx + \frac{1}{2} \int_{R_0}^R E \left(\int_A y^2 dA \right) \left(\frac{\partial^2 v}{\partial x^2} \right)^2 dx \\
 & + \int_{R_0}^R E \frac{\partial^2 v}{\partial x^2} \frac{\partial u}{\partial x} dx \left(\int_A y dA \right) + \frac{1}{2} \int_{R_0}^R E \frac{\partial^2 v}{\partial x^2} \left(\frac{\partial v}{\partial x} \right)^2 dx \left(\int_A y dA \right) \\
 & + \frac{1}{2} \int_{R_0}^R E \left(\int_A dA \right) \left(\frac{\partial u}{\partial x} \right) \left(\frac{\partial v}{\partial x} \right)^2 dx
 \end{aligned} \quad (3.5)$$

Due symmetry assumption along the y -direction $\int_A y dA = 0$. The resultant equilibrium equations are obtained by taking the first variation on the total potential energy.

$$\begin{aligned}
 \delta \Pi_P = & \int_{R_0}^R EA \left(\frac{\partial u}{\partial x} \right) \left(\frac{\partial \delta u}{\partial x} \right) dx + \int_{R_0}^R EI \left(\frac{\partial^2 v}{\partial x^2} \right) \left(\frac{\partial^2 \delta v}{\partial x^2} \right) dx \\
 & + \int_{R_0}^R EA \left(\frac{\partial u}{\partial x} \right) \left(\frac{\partial v}{\partial x} \right) \left(\frac{\partial \delta v}{\partial x} \right) dx \\
 & - \int_{R_0}^R (A \rho_{st} \Omega^2 x - g \rho_{st} A \sin \varphi) \delta u dx - \int_{R_0}^R g \rho_{st} A \cos \varphi \delta v dx = 0
 \end{aligned} \quad (3.6)$$

Using the integration by parts, yields:

$$\begin{aligned}
 \delta \Pi_P = & EA \left(\frac{\partial u}{\partial x} \right) \delta u \Big|_{R_0}^R - \int_{R_0}^R EA \left(\frac{\partial^2 u}{\partial x^2} \right) \delta u dx + EI \frac{\partial^2 v}{\partial x^2} \frac{\partial \delta v}{\partial x} \Big|_{R_0}^R \\
 & - EI \frac{\partial^3 v}{\partial x^3} \delta v \Big|_{R_0}^R + \int_{R_0}^R EI \left(\frac{\partial^4 v}{\partial x^4} \right) \delta v dx + EA \left(\frac{\partial u}{\partial x} \right) \left(\frac{\partial v}{\partial x} \right) \delta v \Big|_{R_0}^R \\
 & - \int_{R_0}^R EA \left(\frac{\partial u}{\partial x} \right) \left(\frac{\partial^2 v}{\partial x^2} \right) \delta v dx - \int_{R_0}^R (A \rho_{st} \Omega^2 x - g \rho_{st} A \sin \varphi) \delta u dx \\
 & - \int_{R_0}^R g \rho_{st} A \cos \varphi \delta v dx = 0
 \end{aligned} \quad (3.7)$$

Writing the integral terms in a matrix form and separating the boundary terms, yields:

$$\begin{aligned}
\delta\Pi_P = & \int_{R_0}^R \begin{bmatrix} -EAu_{,xx} - A\rho_{st}(\Omega^2 x - g \sin \varphi) & 0 \\ 0 & EIv_{,xxxx} - EAu_{,x}v_{,xx} - \rho_{st}Ag \cos \varphi \end{bmatrix} \begin{Bmatrix} \delta u \\ \delta v \end{Bmatrix} dx \\
& + EI \frac{\partial^2 v}{\partial x^2} \frac{\partial \delta v}{\partial x} \Big|_{R_0}^R - EI \frac{\partial^3 v}{\partial x^3} \delta v \Big|_{R_0}^R + EA \left(\frac{\partial u}{\partial x} \right) \delta u \Big|_{R_0}^R \\
& + EA \left(\frac{\partial u}{\partial x} \right) \left(\frac{\partial v}{\partial x} \right) \delta v \Big|_{R_0}^R = 0
\end{aligned} \tag{3.8}$$

The solution of the differential equations must comply with the natural (load/stress) and essential (displacement) boundary conditions:

$$\begin{aligned}
EI \frac{\partial^3 v}{\partial x^3} \Big|_{R_0} = 0 \quad \text{or} \quad \delta v|_{R_0} = 0 \quad & EI \frac{\partial^2 v}{\partial x^2} \Big|_{R_0} = 0 \quad \text{or} \quad \frac{\partial \delta v}{\partial x} \Big|_{R_0} = 0 \\
EA \frac{\partial u}{\partial x} \Big|_{R_0} = 0 \quad \text{or} \quad \delta u|_{R_0} = 0 \quad & EA \left(\frac{\partial u}{\partial x} \right) \left(\frac{\partial v}{\partial x} \right) \Big|_{R_0} = 0 \quad \text{or} \quad \delta v|_{R_0} = 0 \\
EI \frac{\partial^3 v}{\partial x^3} \Big|_R = 0 \quad \text{or} \quad \delta v|_R = 0 \quad & EI \frac{\partial^2 v}{\partial x^2} \Big|_R = 0 \quad \text{or} \quad \frac{\partial \delta v}{\partial x} \Big|_R = 0 \\
EA \frac{\partial u}{\partial x} \Big|_R = 0 \quad \text{or} \quad \delta u|_R = 0 \quad & EA \left(\frac{\partial u}{\partial x} \right) \left(\frac{\partial v}{\partial x} \right) \Big|_R = 0 \quad \text{or} \quad \delta v|_R = 0
\end{aligned} \tag{3.9}$$

As the wind turbine blade is idealized as a cantilever beam, which has one edge clamped and the other free, where on the clamped edge the displacement and rotation are zero and on the free edge the bending moment, shear stress and axial load are zero, then:

$$\begin{aligned}
\delta u|_{R_0} = 0, \quad & EA \frac{\partial u}{\partial x} \Big|_R = EA \left(\frac{\partial u}{\partial x} \right) \left(\frac{\partial v}{\partial x} \right) \Big|_R = 0 \\
\delta v|_{R_0} = \frac{\partial \delta v}{\partial x} \Big|_{R_0} = 0, \quad & EI \frac{\partial^2 v}{\partial x^2} \Big|_R = EI \frac{\partial^3 v}{\partial x^3} \Big|_R = 0
\end{aligned} \tag{3.10}$$

For all non-zero displacement ($\delta u \neq 0$ and $\delta v \neq 0$), the matrix terms of Eq. (3.8) becomes:

$$-EAu_{,xx} - \rho_{st}A(\Omega^2 x - g \sin \varphi) = 0 \tag{3.11}$$

$$EIv_{,xxxx} - EAu_{,x}v_{,xx} - \rho_{st}Ag \cos \varphi = 0 \quad (3.12)$$

Taking the first integral of Eq. (3.11), yields:

$$-EAu_{,x} - \rho_{st}A \left(\Omega^2 \frac{x^2}{2} - \sin \varphi gx \right) + c_1 = 0 \quad (3.13)$$

Then by using the boundary terms of Eq. (3.10):

$$c_1 = \rho_{st}A \left(\Omega^2 \left(\frac{R^2}{2} \right) - g \sin \varphi R \right) \quad (3.14)$$

Replacing Eq. (3.14) in Eq. (3.13), yields:

$$EAu_{,x} = \rho_{st}A \left(\Omega^2 \frac{R^2 - x^2}{2} + g \sin \varphi (R - x) \right) \quad (3.15)$$

Now for Eq. (3.12), taking its first and second integral, yields:

$$\begin{aligned} EIv_{,xxx} - EAu_{,x}v_{,x} - \rho_{st}Ag \cos \varphi x + c_1 &= 0 \\ EIv_{,xx} - EAu_{,x}v - \rho_{st}Ag \cos \varphi \frac{x^2}{2} + c_1x + c_2 &= 0 \end{aligned} \quad (3.16)$$

Applying the boundary conditions, yields:

$$\begin{aligned} c_1 &= \rho_{st}Ag \cos \varphi R \\ c_2 &= \rho_{st}Ag \cos \varphi \frac{R^2}{2} - \rho_{st}Ag \cos \varphi R^2 \end{aligned} \quad (3.17)$$

Replacing Eq. (3.17) in Eq. (3.16), yields:

$$EIv_{,xx} - EAu_{,x}v = \frac{\rho_{st}Ag \cos \varphi}{2} (x^2 - R^2) + \rho_{st}Ag \cos \varphi (R^2 - Rx) \quad (3.18)$$

The boundary conditions formulated from the variational approach leads to Eqs. (3.15) and (3.18) which is the axial and transverse pre-load acting on the blade.

3.1.2 Axial-bending vibration model with pre-stress

The axial-bending vibration model including pre-stress effects is obtained using the Hamilton principle, given as follows,

$$\delta \int_{t_1}^{t_2} (T_{u,w} - U_{u,w}) dt = 0 \quad (3.19)$$

where,

$$T_{u,w} = \frac{1}{2} \int_V \rho_{st} (\dot{u})^2 dV + \frac{1}{2} \int_V \rho_{st} (\dot{w})^2 dV \quad (3.20)$$

$$\begin{aligned} U_{u,w} &= \frac{1}{2} \int_V (\varepsilon_L + \varepsilon_{NL}) \sigma dV = \frac{1}{2} \int_V (\varepsilon_L + \varepsilon_{NL}) E (\varepsilon_L + \varepsilon_{NL}) dV \\ &= \frac{1}{2} \int_V E (\varepsilon_L)^2 dV + \int_V E \varepsilon_{NL} \varepsilon_L dV + \frac{1}{2} \int_V E (\varepsilon_{NL})^2 dV \end{aligned} \quad (3.21)$$

the kinematic relations are,

$$u^* = u + z \frac{\partial w}{\partial x}; \quad w^* = w; \quad \varepsilon_L = \frac{\partial u^*}{\partial x} = \frac{\partial u}{\partial x} + z \frac{\partial^2 w}{\partial x^2}; \quad \varepsilon_{NL} = \frac{1}{2} \left(\frac{\partial w}{\partial x} \right)^2 \quad (3.22)$$

$(\varepsilon_{NL})^2 = 0$ because it is negligible for small displacements, then Eqs. (3.20) and (3.21) can be expressed as:

$$T_{u,w} = \frac{1}{2} \int_{R_0}^R \rho_{st} A (\dot{u})^2 dx + \frac{1}{2} \int_{R_0}^R \rho_{st} A (\dot{w})^2 dx \quad (3.23)$$

$$\begin{aligned} U_{u,w} &= \frac{1}{2} \int_{R_0}^R EA \left(\frac{\partial u}{\partial x} \right)^2 dx + \frac{1}{2} \int_{R_0}^R EI \left(\frac{\partial^2 w}{\partial x^2} \right)^2 dx \\ &\quad + \frac{1}{2} \int_{R_0}^R N_x \left(\frac{\partial w}{\partial x} \right)^2 dx \\ &\quad + \frac{1}{2} \int_{R_0}^R \left(\int_A z dA \right) E \frac{\partial^2 w}{\partial x^2} \left(\frac{\partial w}{\partial x} \right)^2 dx \end{aligned} \quad (3.24)$$

where $N_x = EAu_{,x}$ from Eq. (3.15) and the term $\int_A z dA = 0$ due the symmetry of the cross-section along the z -direction. Assuming a Ritz solution given in hierarchical terms

as written as follows,

$$u = \sum_{j=1}^n \mathcal{N}_j^u(\xi(x)) \phi_j^u(t) = [\mathcal{N}^u] \{\phi_u\} \quad (3.25)$$

$$w = \sum_{j=1}^n \mathcal{N}_j^w(\xi(x)) \phi_j^w(t) = [\mathcal{N}^w] \{\phi_w\} \quad (3.26)$$

$$\{\phi\} = \begin{Bmatrix} \{\phi_u\} \\ \{\phi_w\} \end{Bmatrix} \quad (3.27)$$

where the combination of hierarchical functions $N_j^u(\xi(x))$ and $N_j^w(\xi(x))$ is given in Appendix A. The solution of Eq. (3.19) based on these solutions result in,

$$\begin{aligned} & \int_{t_1}^{t_2} \delta \left[\frac{1}{2} \{\dot{\phi}\}^T [\mathbf{M}_{u,w}] \{\dot{\phi}\} - \frac{1}{2} \{\phi\}^T [\mathbf{K}_{u,w}] \{\phi\} \right. \\ & \left. - \frac{1}{2} \{\phi\}^T [\mathbf{K}_p] \{\phi\} \right] dt = \{0\} \end{aligned} \quad (3.28)$$

where the matrices of Eq. (3.28) are,

$$[\mathbf{M}_{u,w}] = \rho_{st} A \int_{R_0}^R \begin{bmatrix} [\mathcal{N}^u]^T [\mathcal{N}^u] & [0] \\ [0] & [\mathcal{N}^w]^T [\mathcal{N}^w] \end{bmatrix} dx \quad (3.29)$$

$$[\mathbf{K}_{u,w}] = \int_{R_0}^R \begin{bmatrix} EA [\mathcal{N}_{,x}^u]^T [\mathcal{N}_{,x}^u] & [0] \\ [0] & EI [\mathcal{N}_{,xx}^w]^T [\mathcal{N}_{,xx}^w] \end{bmatrix} dx \quad (3.30)$$

$$[\mathbf{K}_p] = \int_{R_0}^R \begin{bmatrix} [0] & [0] \\ [0] & [\mathcal{N}_{,x}^w]^T [\mathcal{N}_{,x}^w] \end{bmatrix} (N_x) dx \quad (3.31)$$

then,

$$\begin{aligned} & \int_{t_1}^{t_2} \left[\{\delta \dot{\phi}\}^T [\mathbf{M}_{u,w}] \{\dot{\phi}\} - \{\delta \phi\}^T [\mathbf{K}_{u,w}] \{\phi\} \right. \\ & \left. - \{\delta \phi\}^T [\mathbf{K}_p] \{\phi\} \right] dt = \{0\} \end{aligned} \quad (3.32)$$

$$\begin{aligned} \{\delta\phi\}^T [\mathbf{M}_{u,w}] \left\{ \dot{\phi} \right\} \Big|_{t_2}^{t_1} + \{\delta\phi\}^T \int_{t_1}^{t_2} \left[-[\mathbf{M}_{u,w}] \left\{ \ddot{\phi} \right\} \cdots \right. \\ \left. - [\mathbf{K}_{u,w}] \left\{ \phi \right\} - [\mathbf{K}_p] \left\{ \phi \right\} \right] dt = \{0\} \end{aligned} \quad (3.33)$$

$$\int_{t_1}^{t_2} \{\delta\phi\}^T \underbrace{\left[[\mathbf{M}_{u,w}] \left\{ \ddot{\phi} \right\} + [\mathbf{K}_{u,w}] \left\{ \phi \right\} + [\mathbf{K}_p] \left\{ \phi \right\} \right]}_{\text{non-trivial solution} = \{0\}} dt = \{0\} \quad (3.34)$$

$\{\delta\phi\}^T [\mathbf{M}_{u,w}] \left\{ \dot{\phi} \right\} \Big|_{t_2}^{t_1} = 0$, due the assumption of stationarity. Assuming a harmonic solution,

$$\{\phi\} = \begin{Bmatrix} \{\mathcal{A}_u\} \\ \{\mathcal{A}_w\} \end{Bmatrix} e^{i\omega t} = \{\mathcal{A}\} e^{i\omega t} \quad (3.35)$$

then,

$$\underbrace{\{[\mathbf{K}_{u,w}] + [\mathbf{K}_p] - \omega^2 [\mathbf{M}_{u,w}]\}}_{\text{Eigenproblem}} \begin{Bmatrix} \{\mathcal{A}_u\} \\ \{\mathcal{A}_w\} \end{Bmatrix} e^{i\omega t} = 0 \quad (3.36)$$

The eigenproblem provides the natural frequencies and vibration modes of a single blade including the pre-stress effects.

3.1.3 Torsional vibration model

Applying Hamilton's principle in the total potential energy for a torsional vibration model (BISHOP *et al.*, 1989), yields:

$$\delta \int_{t_1}^{t_2} (T_\beta - U_\beta) dt = 0 \quad (3.37)$$

where,

$$T_\beta = \frac{1}{2} \int_V \rho_{st} (x^2 + z^2) \left(\dot{\beta} \right)^2 dV \quad (3.38)$$

Eq. (3.38) can also be written as,

$$T_\beta = \frac{1}{2} \int_{R_0}^R I_\theta \rho_{st} \left(\dot{\beta} \right)^2 dx \quad (3.39)$$

as the strain energy U_β ,

$$U_\beta = \frac{1}{2} \int_{R_0}^R GJ \left(\frac{\partial \beta}{\partial x} \right)^2 dx + \frac{1}{2} \int_{R_0}^R E\Gamma \left(\frac{\partial^2 \beta}{\partial x^2} \right)^2 dx \quad (3.40)$$

The proposed formulation accounts for cross-section warping effects, which is the second term $E\Gamma$ of Eq. (3.40). However this effect has been neglected in the analyses presented herein due this parameter not been provided for the SNL100-00 blade. For a Ritz mode solution,

$$\beta = \sum_{j=1}^n \mathcal{N}_j^\beta(\xi(x)) \phi_j^\beta(t) = [\mathcal{N}^\beta] \{\phi_\beta\} \quad (3.41)$$

where hierarchical functions for $\mathcal{N}_j^\beta(\xi(x))$ is found in Appendix A. From Eq. (3.37),

$$\int_{t_1}^{t_2} \{\delta \phi_\beta\}^T \underbrace{\left[[\mathbf{M}_\beta] \{\ddot{\phi}_\beta\} + [\mathbf{K}_{\beta_1}] \{\phi_\beta\} + [\mathbf{K}_{\beta_2}] \{\phi_\beta\} \right]}_{\text{non-trivial solution} = \{0\}} dt = \{0\} \quad (3.42)$$

Assuming a harmonic solution:

$$\{\phi_\beta\} = \{\mathcal{A}_\beta\} e^{i\omega t} \quad (3.43)$$

where $\{\mathcal{A}_\beta\}$ is obtained from the non-trivial solution of Eq. (3.42), expressed in the form of an eigenvalue problem. The matrices of Eq. (3.42) are:

$$[\mathbf{M}_\beta] = \int_{R_0}^R I_\theta \rho_{st} [\mathcal{N}^\beta]^T [\mathcal{N}^\beta] dx \quad (3.44)$$

$$[\mathbf{K}_{\beta_1}] = \int_{R_0}^R GJ [\mathcal{N}_{,x}^\beta]^T [\mathcal{N}_{,x}^\beta] dx \quad (3.45)$$

$$[\mathbf{K}_{\beta_2}] = \int_{R_0}^R E\Gamma [\mathcal{N}_{,xx}^\beta]^T [\mathcal{N}_{,xx}^\beta] dx \quad (3.46)$$

then:

$$\underbrace{\{[\mathbf{K}_{\beta_1}] + [\mathbf{K}_{\beta_2}] - \omega^2 [\mathbf{M}_\beta]\}}_{\text{Eigenproblem}} \{\mathcal{A}_\beta\} e^{i\omega t} = \{0\} \quad (3.47)$$

The eigenproblem provides the natural frequency and vibration modes in torsion for a single blade.

3.2 Unsteady aerodynamic model formulation

The incremental unsteady aerodynamic forces L and M are defined in terms of circulatory and non-circulatory terms (BISPLINGHOFF *et al.*, 1955; YATES Jr, 1966; FUNG, 1969; WRIGHT; COOPER, 2015) as follows,

$$L = \underbrace{\pi \rho_f b^2 \left(\ddot{h}(x, t) + V_{\text{rel}} \dot{\theta}(x, t) - b a \ddot{\theta}(x, t) \right)}_{\text{Non-circulatory}} + \underbrace{c_{l,\alpha} \rho_f V_{\text{rel}} b C(k) \left[\dot{h}(x, t) + V_{\text{rel}} \theta(x, t) + b \left(\frac{c_{l,\alpha}}{2\pi} + a_{c,n} - a \right) \dot{\theta}(x, t) \right]}_{\text{Circulatory}} \quad (3.48)$$

$$M = \underbrace{\pi \rho_f b^2 \left[V_{\text{rel}} \dot{h}(x, t) + b a \ddot{h}(x, t) + V_{\text{rel}}^2 \theta(x, t) - b^2 \left(\frac{1}{8} + a^2 \right) \ddot{\theta}(x, t) \right]}_{\text{Non-circulatory}} - \underbrace{2\pi \rho_f V_{\text{rel}} b^2 \left[\frac{1}{2} - (a - a_{c,n}) C(k) \frac{c_{l,\alpha}}{2\pi} \right] \left[\dot{h}(x, t) + V_{\text{rel}} \theta(x, t) \right]}_{\text{Circulatory}} + \underbrace{b \left(\frac{c_{l,\alpha}}{2\pi} + a_{c,n} - a \right) \dot{\theta}(x, t)}_{\text{Circulatory}} \quad (3.49)$$

where V_{rel} has a different value due to the local position (x) along the blade span as.

$$V_{\text{rel}} = \sqrt{(\Omega x)^2 + (V_\infty)^2} \quad (3.50)$$

The Theodorsen function $C(k)$ is given by,

$$C(k) = \frac{\mathcal{H}_1^{(2)}(k)}{\mathcal{H}_1^{(2)}(k) + i\mathcal{H}_0^{(2)}(k)} \quad (3.51)$$

Although the Theodorsen function was originally proposed for fixed wings, most of aeroelastic studies still use this function for rotating wings neglecting the waking effect caused by the blades. (LOEWY, 1957) considers the shed vorticity of the wind turbine blades. The lift deficiency function $C(k)$ can be replaced by Loewy's function $C'(k, \gamma, \mu)$, which is defined as follows,

$$C'(k, \gamma, \mu) = \frac{\mathcal{H}_1^{(2)}(k) + 2\mathcal{J}_1(k)\Upsilon(k, \gamma, \mu)}{\mathcal{H}_1^{(2)}(k) + i\mathcal{H}_0^{(2)}(k) + 2[\mathcal{J}_1(k) + i\mathcal{J}_0(k)]\Upsilon(k, \gamma, \mu)} \quad (3.52)$$

where,

$$\Upsilon(k, \gamma, \mu) = [e^{k\gamma + 2\pi i\mu} - 1]^{-1}, \quad \mu = \frac{\omega}{\Omega N_{bl}}, \quad \gamma = \frac{2\pi V_\infty}{\Omega b N_{bl}} \quad (3.53)$$

The next procedure follows the aeroelastic formulation describe by (WRIGHT; COOPER, 2015), but their formulation is based on thin-airfoil theory where $c_{l,\alpha} = 2\pi$. As wind turbine blades present unsymetric and thick airfoils the value of $c_{l,\alpha}$ changes as well as the position of the aerodynamic center, then to include the airfoil thickness into the formulation it is followed the work of (YATES Jr, 1966).

Assuming harmonic solution, heave and pitch can also be express as:

$$\begin{aligned} h(x, t) &= f_h(x)e^{i\omega t}, \quad \dot{h}(x, t) = i\omega f_h(x)e^{i\omega t}, \\ \ddot{h}(x, t) &= -\omega^2 f_h(x)e^{i\omega t} \end{aligned} \quad (3.54)$$

$$\begin{aligned} \theta(x, t) &= f_\theta(x)e^{i\omega t}, \quad \dot{\theta}(x, t) = i\omega f_\theta(x)e^{i\omega t}, \\ \ddot{\theta}(x, t) &= -\omega^2 f_\theta(x)e^{i\omega t} \end{aligned} \quad (3.55)$$

By taking the expressions of Eqs. (3.48) and (3.49) for the lift and moment about the elastic axis of the oscillating airfoil and substituting the Eqs. (3.54) and (3.55), the complex form of the lift deficiency function (Theodorsen or Loewy), the heave and pitch motions, then become:

$$\begin{aligned} L = & \left\{ \pi \rho_f b^2 [-\omega^2 f_h(x) + i\omega V_{\text{rel}} f_\theta(x) + \omega^2 b a f_\theta(x)] + c_{l,\alpha} \rho_f V_{\text{rel}} b \right. \\ & \left. (\mathcal{F} + i\mathcal{G}) \left[i\omega f_h(x) + V_{\text{rel}} f_\theta(x) + i\omega b \left(\frac{c_{l,\alpha}}{2\pi} + a_{c,n} - a \right) f_\theta(x) \right] \right\} e^{i\omega t} \end{aligned} \quad (3.56)$$

$$\begin{aligned} M = & \left\{ \pi \rho_f b^2 [i\omega V_{\text{rel}} f_h(x) - \omega^2 b a f_h(x) + V_{\text{rel}}^2 f_\theta(x) + b^2 \omega^2 \dots \right. \\ & \left. \left(\frac{1}{8} + a^2 \right) f_\theta(x) \right] - 2\pi \rho_f V_{\text{rel}} b^2 \left[\frac{1}{2} - (a - a_{c,n}) (\mathcal{F} + i\mathcal{G}) \frac{c_{l,\alpha}}{2\pi} \right] \\ & \left. [i\omega f_h(x) + V_{\text{rel}} f_\theta(x) + i\omega b \left(\frac{c_{l,\alpha}}{2\pi} + a_{c,n} - a \right) f_\theta(x)] \right\} e^{i\omega t} \end{aligned} \quad (3.57)$$

where the complex form is $C(k)$ or $C'(k) = \mathcal{F} + i\mathcal{G}$.

Eqs. (3.56) and (3.57) can be rewritten as follows,

$$\begin{aligned}
 L = \pi \rho_f b^2 & \left[-\frac{k^2 V_{\text{rel}}^2}{b^2} h(x, t) + V_{\text{rel}} \dot{\theta}(x, t) + \frac{k^2 V_{\text{rel}}^2}{b} a \theta(x, t) \right] \\
 & + c_{l,\alpha} \rho_f V_{\text{rel}} b \left[\mathcal{F} \dot{h} - \frac{\mathcal{G} k V_{\text{rel}}}{b} h(x, t) + \mathcal{F} V_{\text{rel}} \theta(x, t) + \frac{b}{k} \mathcal{G} \dot{\theta}(x, t) \right. \\
 & \left. + \mathcal{F} b \left(\frac{c_{l,\alpha}}{2\pi} + a_{c,n} - a \right) \dot{\theta}(x, t) - \mathcal{G} V_{\text{rel}} k \left(\frac{c_{l,\alpha}}{2\pi} + a_{c,n} - a \right) \theta(x, t) \right]
 \end{aligned} \tag{3.58}$$

$$\begin{aligned}
 M = \pi \rho_f b^2 & \left[-\frac{k^2 V_{\text{rel}}^2}{b} a h(x, t) - V_{\text{rel}} b \left(\frac{c_{l,\alpha}}{2\pi} + a_{c,n} - a \right) \dot{\theta}(x, t) \right. \\
 & \left. + b^2 k^2 V_{\text{rel}}^2 \left(\frac{1}{8} + a^2 \right) \theta(x, t) \right] + 2\pi \rho_f V_{\text{rel}} b^2 (a - a_{c,n}) \frac{c_{l,\alpha}}{2\pi} \\
 & \left[\mathcal{F} \dot{h}(x, t) - \mathcal{G} \frac{k V_{\text{rel}}}{b} h(x, t) + \mathcal{F} V_{\text{rel}} \theta(x, t) + \frac{b}{k} \mathcal{G} \dot{\theta}(x, t) \right. \\
 & \left. + \mathcal{F} b \left(\frac{c_{l,\alpha}}{2\pi} + a_{c,n} - a \right) \dot{\theta}(x, t) - \mathcal{G} k V_{\text{rel}} \left(\frac{c_{l,\alpha}}{2\pi} + a_{c,n} - a \right) \theta(x, t) \right]
 \end{aligned} \tag{3.59}$$

To simplify Eqs. (3.58) and (3.59) the following auxiliary variables are defined,

$$\begin{aligned}
 L_h &= -\pi k^2 - c_{l,\alpha} \mathcal{G} k \\
 L_{\dot{h}} &= c_{l,\alpha} \mathcal{F} \\
 L_{\theta} &= \pi k^2 a + c_{l,\alpha} \mathcal{F} - c_{l,\alpha} \mathcal{G} k \left(\frac{c_{l,\alpha}}{2\pi} + a_{c,n} - a \right) \\
 L_{\dot{\theta}} &= \pi + c_{l,\alpha} \mathcal{F} \left(\frac{c_{l,\alpha}}{2\pi} + a_{c,n} - a \right) + c_{l,\alpha} \frac{\mathcal{G}}{k} \\
 L &= \rho_f V_{\text{rel}}^2 \left(L_h h(x, t) + L_{\dot{h}} \frac{b \dot{h}(x, t)}{V_{\text{rel}}} + L_{\theta} b \theta(x, t) + L_{\dot{\theta}} \frac{b^2 \dot{\theta}(x, t)}{V_{\text{rel}}} \right)
 \end{aligned} \tag{3.60}$$

$$\begin{aligned}
M_h &= -\pi k^2 a - c_{l,\alpha} k (a - a_{c,n}) \mathcal{G} \\
M_{\dot{h}} &= c_{l,\alpha} (a - a_{c,n}) \mathcal{F} \\
M_\theta &= \pi k^2 \left(\frac{1}{8} + a^2 \right) + c_{l,\alpha} \mathcal{F} (a - a_{c,n}) \\
&\quad - c_{l,\alpha} k \mathcal{G} (a - a_{c,n}) \left(\frac{c_{l,\alpha}}{2\pi} + a_{c,n} - a \right) \\
M_{\dot{\theta}} &= -\pi k \left(\frac{c_{l,\alpha}}{2\pi} + a_{c,n} - a \right) + c_{l,\alpha} k \mathcal{F} (a - a_{c,n}) \\
&\quad \left(\frac{c_{l,\alpha}}{2\pi} + a_{c,n} - a \right) + c_{l,\alpha} \frac{\mathcal{G}}{k} (a - a_{c,n}) \\
M &= \rho_f V_{\text{rel}}^2 \left(M_h b h(x, t) + M_{\dot{h}} \frac{b^2 \dot{h}(x, t)}{V_{\text{rel}}} + M_\theta b^2 \theta(x, t) + M_{\dot{\theta}} \frac{b^3 \dot{\theta}(x, t)}{V_{\text{rel}}} \right)
\end{aligned} \tag{3.61}$$

Writing in matrix form:

$$\begin{Bmatrix} -L \\ M \end{Bmatrix} = \rho_f [\mathbf{B}] \begin{Bmatrix} \dot{h}(x, t) \\ \dot{\theta}(x, t) \end{Bmatrix} + \rho_f [\mathbf{C}] \begin{Bmatrix} h(x, t) \\ \theta(x, t) \end{Bmatrix} \tag{3.62}$$

where:

$$[\mathbf{B}] = \begin{bmatrix} -b L_{\dot{h}} V_{\text{rel}} & -b^2 L_{\dot{\theta}} V_{\text{rel}} \\ b^2 M_{\dot{h}} V_{\text{rel}} & b^3 M_{\dot{\theta}} V_{\text{rel}} \end{bmatrix} \tag{3.63}$$

$$[\mathbf{C}] = \begin{bmatrix} -L_h V_{\text{rel}}^2 & -b L_\theta V_{\text{rel}}^2 \\ b M_h V_{\text{rel}}^2 & b^2 M_\theta V_{\text{rel}}^2 \end{bmatrix} \tag{3.64}$$

3.3 Aeroelastic model formulation

The aeroelastic model formulation is based on the Hamilton principle combined with the aerodynamic strip theory, given as follows,

$$\delta \int_{t_1}^{t_2} (T_{w,\beta} - U_{w,\beta}) dt + \delta \int_{t_1}^{t_2} W_{\text{NC}} dt - \delta \int_{t_1}^{t_2} V_D dt = 0 \tag{3.65}$$

where:

$$T_{w,\beta} = \frac{1}{2} \int_{R_0}^R \begin{Bmatrix} \dot{h}(x,t) \\ \dot{\theta}(x,t) \end{Bmatrix}^T \begin{bmatrix} m & S_{sc} \\ S_{sc} & \rho_{st} I_\theta \end{bmatrix} \begin{Bmatrix} \dot{h}(x,t) \\ \dot{\theta}(x,t) \end{Bmatrix} dx \quad (3.66)$$

$$\begin{aligned} U_{w,\beta} &= \frac{1}{2} \int_{R_0}^R \begin{Bmatrix} h_{,xx}(x,t) \\ \theta_{,xx}(x,t) \end{Bmatrix}^T \begin{bmatrix} EI & 0 \\ 0 & E\Gamma \end{bmatrix} \begin{Bmatrix} h_{,xx}(x,t) \\ \theta_{,xx}(x,t) \end{Bmatrix} dx \\ &+ \frac{1}{2} \int_{R_0}^R \begin{Bmatrix} h_{,x}(x,t) \\ \theta_{,x}(x,t) \end{Bmatrix}^T \begin{bmatrix} N_x & 0 \\ 0 & GJ \end{bmatrix} \begin{Bmatrix} h_{,x}(x,t) \\ \theta_{,x}(x,t) \end{Bmatrix} dx \end{aligned} \quad (3.67)$$

$$W_{NC} = \int_{R_0}^R \begin{Bmatrix} h(x,t) \\ \theta(x,t) \end{Bmatrix}^T \left(\rho_f [\mathbf{B}] \begin{Bmatrix} \dot{h}(x,t) \\ \dot{\theta}(x,t) \end{Bmatrix} + \rho_f [\mathbf{C}] \begin{Bmatrix} h(x,t) \\ \theta(x,t) \end{Bmatrix} \right) dx \quad (3.68)$$

$$V_D = \int_{R_0}^R \begin{Bmatrix} h(x,t) \\ \theta(x,t) \end{Bmatrix}^T \begin{bmatrix} c_h & 0 \\ 0 & c_\theta \end{bmatrix} \begin{Bmatrix} \dot{h}(x,t) \\ \dot{\theta}(x,t) \end{Bmatrix} dx \quad (3.69)$$

By using the modal superposition principle, $\theta(x,t)$ and $h(x,t)$ can be expressed in terms of an enriched modal base composed by **m**-bending modes and **n**-torsion modes as follows,

$$\begin{aligned} h(x,t) &= \sum_{i=1}^m f_i^h(x) \underline{h}_i(t) = [f_1^h(x) \ f_2^h(x) \ \cdots \ f_m^h(x)] \begin{Bmatrix} \underline{h}_1(t) \\ \underline{h}_2(t) \\ \vdots \\ \underline{h}_m(t) \end{Bmatrix} \\ &= [\mathcal{W}] \{ \underline{h}(t) \} \end{aligned} \quad (3.70)$$

$$\begin{aligned}
\theta(x, t) &= \sum_{i=1}^n f_i^\theta(x) \underline{\theta}_i(t) = \begin{bmatrix} f_1^\theta(x) & f_2^\theta(x) & \cdots & f_n^\theta(x) \end{bmatrix} \begin{Bmatrix} \underline{\theta}_1(t) \\ \underline{\theta}_2(t) \\ \vdots \\ \underline{\theta}_n(t) \end{Bmatrix} \\
&= [\mathcal{B}] \{ \underline{\theta}(t) \}
\end{aligned} \tag{3.71}$$

where,

$$\begin{Bmatrix} h(x, t) \\ \theta(x, t) \end{Bmatrix} = \begin{bmatrix} [\mathcal{W}] & [0]_{1,m} \\ [0]_{1,n} & [\mathcal{B}] \end{bmatrix} \begin{Bmatrix} \{ \underline{h}(t) \} \\ \{ \underline{\theta}(t) \} \end{Bmatrix} \tag{3.72}$$

$$\begin{aligned}
f_i^h(x) &= [\mathcal{N}^w] \{ \mathcal{A}_w^i \} \\
f_i^\theta(x) &= [\mathcal{N}^\beta] \{ \mathcal{A}_\beta^i \}
\end{aligned} \tag{3.73}$$

$[\mathcal{N}^w] \{ \mathcal{A}_w^i \}$ and $[\mathcal{N}^\beta] \{ \mathcal{A}_\beta^i \}$ are the normalized uncoupled modes in bending and torsion respectively. Then Eqs. (3.66) to (3.69) can be written and simplified as follows,

$$\begin{aligned}
T_{w,\beta} &= \frac{1}{2} \int_{R_0}^R \left\{ \begin{Bmatrix} \dot{\underline{h}}(t) \\ \dot{\underline{\theta}}(t) \end{Bmatrix} \right\}^T \begin{bmatrix} [\mathcal{W}] & [0]_{1,m} \\ [0]_{1,n} & [\mathcal{B}] \end{bmatrix}^T \begin{bmatrix} m & S_{sc} \\ S_{sc} & \rho_{st} I_\theta \end{bmatrix} \cdots \\
&\quad \begin{bmatrix} [\mathcal{W}] & [0]_{1,m} \\ [0]_{1,n} & [\mathcal{B}] \end{bmatrix} \begin{Bmatrix} \dot{\underline{h}}(t) \\ \dot{\underline{\theta}}(t) \end{Bmatrix} dx
\end{aligned} \tag{3.74}$$

then,

$$T_{w,\beta} = \frac{1}{2} \left\{ \begin{Bmatrix} \dot{\underline{h}}(t) \\ \dot{\underline{\theta}}(t) \end{Bmatrix} \right\}^T [\tilde{\mathbf{M}}] \begin{Bmatrix} \dot{\underline{h}}(t) \\ \dot{\underline{\theta}}(t) \end{Bmatrix} \tag{3.75}$$

as for,

$$\begin{aligned}
 U_{w,\beta} = & \frac{1}{2} \int_{R_0}^R \left\{ \begin{Bmatrix} \underline{h}(t) \\ \underline{\theta}(t) \end{Bmatrix} \right\}^T \left(\begin{bmatrix} [\mathcal{W}_{,xx}] & [0]_{1,m} \\ [0]_{1,n} & [\mathcal{B}_{,xx}] \end{bmatrix}^T \begin{bmatrix} EI & 0 \\ 0 & E\Gamma \end{bmatrix} \dots \right. \\
 & \left. \begin{bmatrix} [\mathcal{W}_{,xx}] & [0]_{1,m} \\ [0]_{1,n} & [\mathcal{B}_{,xx}] \end{bmatrix} + \begin{bmatrix} [\mathcal{W}_{,x}] & [0]_{1,m} \\ [0]_{1,n} & [\mathcal{B}_{,x}] \end{bmatrix}^T \dots \right. \\
 & \left. \begin{bmatrix} N_x & 0 \\ 0 & GJ \end{bmatrix} \begin{bmatrix} [\mathcal{W}_{,x}] & [0]_{1,m} \\ [0]_{1,n} & [\mathcal{B}_{,x}] \end{bmatrix} \right) \left\{ \begin{Bmatrix} \underline{h}(t) \\ \underline{\theta}(t) \end{Bmatrix} \right\} dx
 \end{aligned} \tag{3.76}$$

then,

$$U_{w,\beta} = \frac{1}{2} \left\{ \begin{Bmatrix} \underline{h}(t) \\ \underline{\theta}(t) \end{Bmatrix} \right\}^T [\tilde{\mathbf{K}}] \left\{ \begin{Bmatrix} \underline{h}(t) \\ \underline{\theta}(t) \end{Bmatrix} \right\} \tag{3.77}$$

$$\begin{aligned}
 W_{\text{NC}} = & \int_{R_0}^R \left\{ \begin{Bmatrix} \underline{h}(t) \\ \underline{\theta}(t) \end{Bmatrix} \right\}^T \begin{bmatrix} [\mathcal{W}] & [0]_{1,m} \\ [0]_{1,n} & [\mathcal{B}] \end{bmatrix}^T (\rho_f [\mathbf{B}] \dots \\
 & \left[\begin{bmatrix} [\mathcal{W}] & [0]_{1,m} \\ [0]_{1,n} & [\mathcal{B}] \end{bmatrix} \left\{ \begin{Bmatrix} \dot{\underline{h}}(t) \\ \dot{\underline{\theta}}(t) \end{Bmatrix} \right\} + \rho_f [\mathbf{C}] \begin{bmatrix} [\mathcal{W}] & [0]_{1,m} \\ [0]_{1,n} & [\mathcal{B}] \end{bmatrix} \left\{ \begin{Bmatrix} \underline{h}(t) \\ \underline{\theta}(t) \end{Bmatrix} \right\} \right) dx
 \end{aligned} \tag{3.78}$$

then,

$$W_{\text{NC}} = \left\{ \begin{Bmatrix} \underline{h}(t) \\ \underline{\theta}(t) \end{Bmatrix} \right\}^T \left(\rho_f [\tilde{\mathbf{B}}] \left\{ \begin{Bmatrix} \dot{\underline{h}}(t) \\ \dot{\underline{\theta}}(t) \end{Bmatrix} \right\} + \rho_f [\tilde{\mathbf{C}}] \left\{ \begin{Bmatrix} \underline{h}(t) \\ \underline{\theta}(t) \end{Bmatrix} \right\} \right) \tag{3.79}$$

$$\begin{aligned}
 V_D = & \int_{R_0}^R \left\{ \begin{Bmatrix} \underline{h}(t) \\ \underline{\theta}(t) \end{Bmatrix} \right\}^T \begin{bmatrix} [\mathcal{W}] & [0]_{1,m} \\ [0]_{1,n} & [\mathcal{B}] \end{bmatrix}^T \begin{bmatrix} c_h & 0 \\ 0 & c_\theta \end{bmatrix} \dots \\
 & \left[\begin{bmatrix} [\mathcal{W}] & [0]_{1,m} \\ [0]_{1,n} & [\mathcal{B}] \end{bmatrix} \left\{ \begin{Bmatrix} \dot{\underline{h}}(t) \\ \dot{\underline{\theta}}(t) \end{Bmatrix} \right\} \right] dx
 \end{aligned} \tag{3.80}$$

then,

$$V_D = \begin{Bmatrix} \{\underline{h}(t)\} \\ \{\underline{\theta}(t)\} \end{Bmatrix}^T [\tilde{\mathbf{D}}] \begin{Bmatrix} \{\dot{\underline{h}}(t)\} \\ \{\dot{\underline{\theta}}(t)\} \end{Bmatrix} \quad (3.81)$$

where the mass and stiffness matrices $[\tilde{\mathbf{M}}]$ and $[\tilde{\mathbf{K}}]$ due bending and torsion, are defined as,

$$[\tilde{\mathbf{M}}] = \int_{R_0}^R \begin{bmatrix} [\mathcal{W}] & [0]_{1,m} \\ [0]_{1,n} & [\mathcal{B}] \end{bmatrix}^T \begin{bmatrix} m & S_{sc} \\ S_{sc} & \rho_{st} I_\theta \end{bmatrix} \begin{bmatrix} [\mathcal{W}] & [0]_{1,m} \\ [0]_{1,n} & [\mathcal{B}] \end{bmatrix} dx \quad (3.82)$$

$$\begin{aligned} [\tilde{\mathbf{K}}] = \int_{R_0}^R & \left(\begin{bmatrix} [\mathcal{W}_{,xx}] & [0]_{1,m} \\ [0]_{1,n} & [\mathcal{B}_{,xx}] \end{bmatrix}^T \begin{bmatrix} EI & 0 \\ 0 & E\Gamma \end{bmatrix} \dots \right. \\ & \left. \begin{bmatrix} [\mathcal{W}_{,xx}] & [0]_{1,m} \\ [0]_{1,n} & [\mathcal{B}_{,xx}] \end{bmatrix} + \begin{bmatrix} [\mathcal{W}_{,x}] & [0]_{1,m} \\ [0]_{1,n} & [\mathcal{B}_{,x}] \end{bmatrix}^T \dots \right. \\ & \left. \begin{bmatrix} N_x & 0 \\ 0 & GJ \end{bmatrix} \begin{bmatrix} [\mathcal{W}_{,x}] & [0]_{1,m} \\ [0]_{1,n} & [\mathcal{B}_{,x}] \end{bmatrix} \right) dx \end{aligned} \quad (3.83)$$

Similarly, the aerodynamic damping, aerodynamic stiffness and structural damping matrices $[\tilde{\mathbf{B}}]$, $[\tilde{\mathbf{C}}]$ and $[\tilde{\mathbf{D}}]$ can be defined respectively as follows,

$$[\tilde{\mathbf{B}}] = \int_{R_0}^R \begin{bmatrix} [\mathcal{W}] & [0]_{1,m} \\ [0]_{1,n} & [\mathcal{B}] \end{bmatrix}^T [\mathbf{B}] \begin{bmatrix} [\mathcal{W}] & [0]_{1,m} \\ [0]_{1,n} & [\mathcal{B}] \end{bmatrix} dx \quad (3.84)$$

$$[\tilde{\mathbf{C}}] = \int_{R_0}^R \begin{bmatrix} [\mathcal{W}] & [0]_{1,m} \\ [0]_{1,n} & [\mathcal{B}] \end{bmatrix}^T [\mathbf{C}] \begin{bmatrix} [\mathcal{W}] & [0]_{1,m} \\ [0]_{1,n} & [\mathcal{B}] \end{bmatrix} dx \quad (3.85)$$

$$[\tilde{\mathbf{D}}] = \int_{R_0}^R \begin{bmatrix} [\mathcal{W}] & [0]_{1,m} \\ [0]_{1,n} & [\mathcal{B}] \end{bmatrix}^T \begin{bmatrix} c_h & 0 \\ 0 & c_\theta \end{bmatrix} \begin{bmatrix} [\mathcal{W}] & [0]_{1,m} \\ [0]_{1,n} & [\mathcal{B}] \end{bmatrix} dx \quad (3.86)$$

Defining,

$$\{\underline{q}\} = \begin{Bmatrix} \{\underline{h}(t)\} \\ \{\underline{\theta}(t)\} \end{Bmatrix} \quad (3.87)$$

The aeroelastic model formulation obtained from Eq. (3.65) then becomes,

$$\begin{aligned} \delta \int_{t_1}^{t_2} \left(\frac{1}{2} \{\dot{\underline{q}}\}^T [\tilde{\mathbf{M}}] \{\dot{\underline{q}}\} - \frac{1}{2} \{\underline{q}\}^T [\tilde{\mathbf{K}}] \{\underline{q}\} - \{\underline{q}\}^T [\tilde{\mathbf{D}}] \{\dot{\underline{q}}\} \right. \\ \left. + \rho_f \{\underline{q}\}^T [\tilde{\mathbf{B}}] \{\dot{\underline{q}}\} + \rho_f \{\underline{q}\}^T [\tilde{\mathbf{C}}] \{\underline{q}\} \right) dt = \{0\} \end{aligned} \quad (3.88)$$

After taking the first variation and integrating by parts leads to,

$$\begin{aligned} \int_{t_1}^{t_2} \{\delta \underline{q}\}^T \left(-[\tilde{\mathbf{M}}] \{\ddot{\underline{q}}\} - [\tilde{\mathbf{K}}] \{\underline{q}\} - [\tilde{\mathbf{D}}] \{\dot{\underline{q}}\} \right. \\ \left. + \rho_f [\tilde{\mathbf{B}}] \{\dot{\underline{q}}\} + \rho_f [\tilde{\mathbf{C}}] \{\underline{q}\} \right) dt = \{0\} \end{aligned} \quad (3.89)$$

For any arbitrary and admissible $\{\delta \underline{q}\} \neq \{0\}$, then Eq. (3.89) becomes,

$$-[\tilde{\mathbf{M}}] \{\ddot{\underline{q}}\} - [\tilde{\mathbf{K}}] \{\underline{q}\} - [\tilde{\mathbf{D}}] \{\dot{\underline{q}}\} + \rho_f [\tilde{\mathbf{B}}] \{\dot{\underline{q}}\} + \rho_f [\tilde{\mathbf{C}}] \{\underline{q}\} = \{0\} \quad (3.90)$$

using the relation,

$$[\mathbf{I}] \{\dot{\underline{q}}\} - [\mathbf{I}] \{\dot{\underline{q}}\} = \{0\} \quad (3.91)$$

then, by combining Eqs. (3.90) and (3.91), it gets,

$$\begin{Bmatrix} \{\dot{\underline{q}}\} \\ \{\ddot{\underline{q}}\} \end{Bmatrix} - [Q] \begin{Bmatrix} \{\underline{q}\} \\ \{\dot{\underline{q}}\} \end{Bmatrix} = \begin{Bmatrix} \{0\} \\ \{0\} \end{Bmatrix} \quad \text{or} \quad \{\dot{\mathbf{x}}\} - [Q]\{\mathbf{x}\} = \{0\} \quad (3.92)$$

where,

$$[Q] = \begin{bmatrix} [0] & [\mathbf{I}] \\ [\tilde{\mathbf{M}}]^{-1} (\rho_f [\tilde{\mathbf{C}}] - [\tilde{\mathbf{K}}]) & [\tilde{\mathbf{M}}]^{-1} (\rho_f [\tilde{\mathbf{B}}] - [\tilde{\mathbf{D}}]) \end{bmatrix} \quad (3.93)$$

By assuming $\mathbf{x} = \mathbf{x}_0 e^{\lambda t}$, then the eigenproblem becomes:

$$\{[\mathbf{I}]\lambda - [\mathbf{Q}]\} \mathbf{x}_0 = \{0\} \text{ or } \{[\mathbf{Q}] - \lambda[\mathbf{I}]\} \mathbf{x}_0 = \{0\} \quad (3.94)$$

The eigenvalues λ of the system matrix \mathbf{Q} occur in complex conjugate pairs and are in the form:

$$\begin{aligned} \lambda_s &= -\zeta_s \omega_s \pm i \omega_s \sqrt{1 - \zeta_s^2} \\ \text{for } \rightarrow s &= 1, \dots, (\mathbf{m} + \mathbf{n}) \times 2 \end{aligned} \quad (3.95)$$

$$\omega_s = \sqrt{(\text{Real}(\lambda_s))^2 + (\text{Imag}(\lambda_s))^2}; \quad \zeta_s = \frac{\text{Real}(\lambda_s)}{\omega_s} \quad (3.96)$$

The corresponding eigenvectors appear in complex conjugate columns and take the form:

$$\{\mathbf{x}_0\}_s = \begin{Bmatrix} \{\underline{q}\}_s \\ \lambda_s \{\underline{q}\}_s \end{Bmatrix} \quad (3.97)$$

It is characterize flutter when the real part of the complex conjugate eigenvalues becomes positive.

In the case that the imaginary part of λ reaches zero, λ will not be in complex conjugate pair anymore. The real part of the eigenvalue will split in to two different values, which will characterize divergence if one of the real part of the eigenvalue becomes positive.

The solution procedure employed to solve the eigenproblem given by Eq. (3.94) is based on a modified version of the PK method, whose implementation flowchart is depicted in Fig. 3.2.

It should be noticed that to get a range of Ω 's the first input Ω should be a lower value, because to lower rotations the flutter frequency values is near the free vibration frequency, where the frequencies found in the eigenproblems given by Eqs. (3.36) and (3.47) will be used, it is also important to state that V_{rel} can not be zero due to a singularity appears in the reduced frequency (k), then if $V_{\infty} = 0$ the Ω has to be > 0 . As the rotation increases it is difficult to find a possible frequency guessing value because flutter and free vibration frequency are not close enough to converge, so a good solution is to use small steps between Ω 's values and use the previous flutter frequency response obtained from Eq. (3.94) as a initial guess for the next Ω .

It is worth mentioning that the numerical integration method used was Legendre-

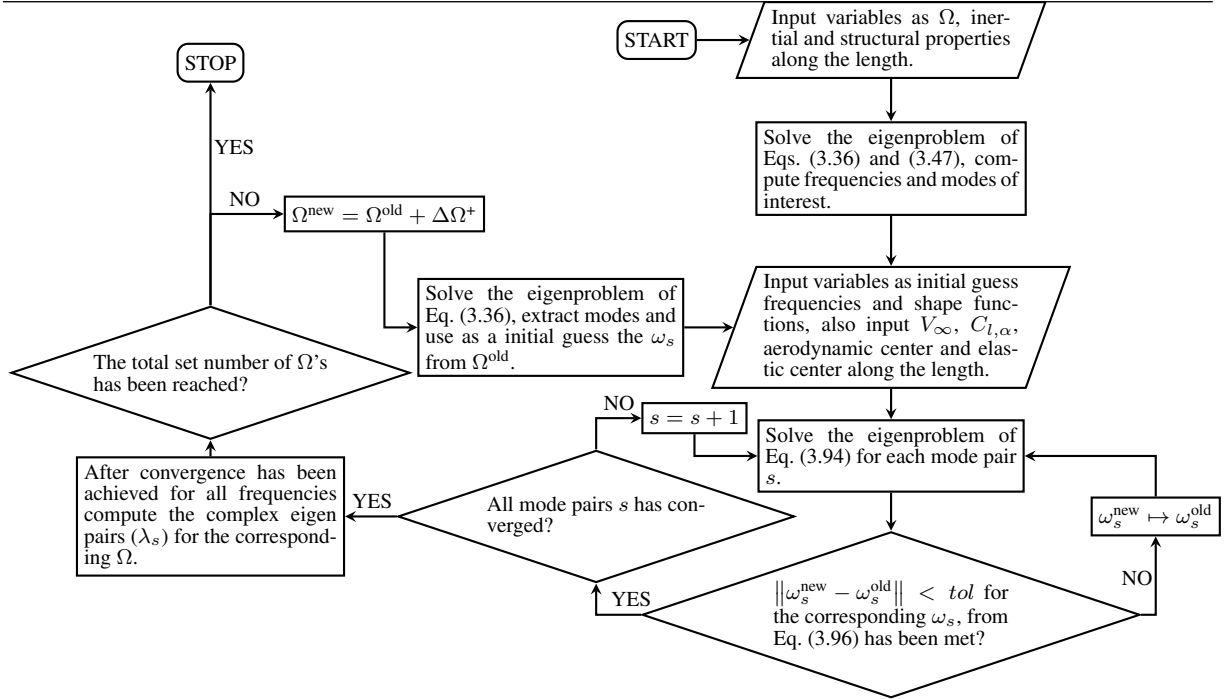


FIGURE 3.2 – Flowchart explaining the PK method adapted to a rotating wing.

Gauss quadrature with 50 weight functions, the number of hierarchical functions was eight and two contour terms to satisfy the boundary conditions. The inertial, stiffness and geometric properties of the SNL100-00 blade vary along the blade length and their values are available in (Sandia National Laboratories, 2018) website and can be also found in Appendix B, the structural damping has also been neglected due to not be available for the SNL100-00 blade, then $c_h = c_\theta = 0$.

4 Results and discussion

This chapter shows a study case carried out using the proposed model focused on the dynamic and aeroelastic analyses for the SNL 100-00 wind turbine blade. The modal frequencies due to centrifugal and gravitational loads are presented. The aeroelastic analyses show the differences of Loewy and Theodorsen reduced lift functions in diagrams that aid in the determination of flutter and divergence predicted velocities.

4.1 Modal analysis

In the present work it is noticed that the natural frequency changes with the angle position (φ) of the blade in relation to the rotating area due the gravitational load, however it presents a small role in the frequency response to the flapwise bending modes, as shown in Table 4.1. It can also be noticed that when the blade is positioned at $\varphi = 0$ or $\varphi = \pi$ no influence is caused by the gravity in the frequency as to $\pi/2$ the frequency decreases and $3\pi/2$ the frequency increases, those effects is caused by N_x which makes the blade more or less stiff.

Blade position	0 rad	$\pi/2$ rad	π rad	$3\pi/2$ rad
1 st flapwise	0.32 Hz	0.31 Hz	0.32 Hz	0.34 Hz
2 nd flapwise	0.92 Hz	0.91 Hz	0.92 Hz	0.94 Hz
3 rd flapwise	2.06 Hz	2.04 Hz	2.06 Hz	2.07 Hz
4 th flapwise	3.69 Hz	3.67 Hz	3.69 Hz	3.71 Hz
5 th flapwise	5.66 Hz	5.64 Hz	5.66 Hz	5.67 Hz
1 st torsion	3.48 Hz	3.48 Hz	3.48 Hz	3.48 Hz
2 nd torsion	6.38 Hz	6.38 Hz	6.38 Hz	6.38 Hz

TABLE 4.1 – Modal frequencies of the SNL 100-00 blade with different blade angle position.

As the centrifugal effects, it has a more significant effect on the natural frequency response (AKSENCER; AYDOGDU, 2015; ROSTAMI *et al.*, 2016; RAFIEE *et al.*, 2017), while increases with Ω as show by Table 4.2 the flapwise frequency mode changes, this is also due to the blade stiffening caused by the centrifugal axial load in N_x .

Rotations	0 rpm	15 rpm	30 rpm
1 st flapwise	0.32 Hz	0.55 Hz	0.90 Hz
2 nd flapwise	0.92 Hz	1.20 Hz	1.79 Hz
3 rd flapwise	2.06 Hz	2.36 Hz	3.10 Hz
4 th flapwise	3.69 Hz	3.99 Hz	4.81 Hz
5 th flapwise	5.66 Hz	5.96 Hz	6.81 Hz
1 st torsion	3.48 Hz	3.48 Hz	3.48 Hz
2 nd torsion	6.38 Hz	6.38 Hz	6.38 Hz

TABLE 4.2 – Modal frequencies of the SNL 100-00 blade in the position of 0 rad.

Observing Fig. 4.1 it is noticed that the effect of the centrifugal load has changed the mode shape for different Ω 's, where it is more visible in the 1st flapwise (Fig. 4.1a).

The torsional frequency and mode shape (Figs. 4.1f and 4.1g) remains the same regardless the rotation and blade position, because they are not dependent on the external loads.

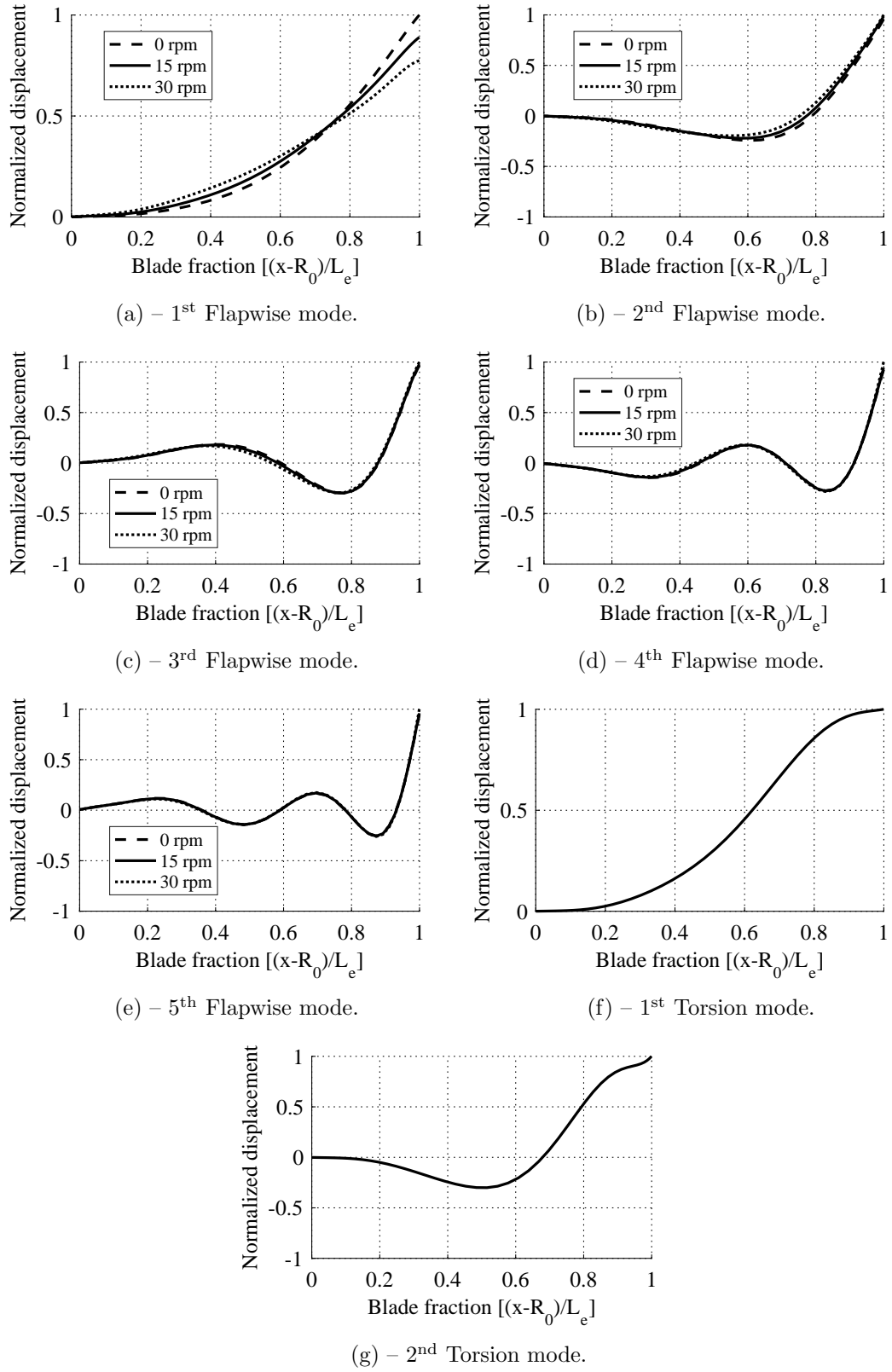


FIGURE 4.1 – Mode shapes of the SNL 100-00 blade due centrifugal loads.

4.2 Aeroelastic analysis using Theodorsen's function

The aeroelastic response using Theodorsen function is shown in Figs. 4.2 to 4.4 for 0, 10 and 20 m/s of wind velocity (V_∞) respectively, the first five flapwise bending modes and the first two torsional modes were plotted with different colors to represent each mode computed using the modified version of the PK method.

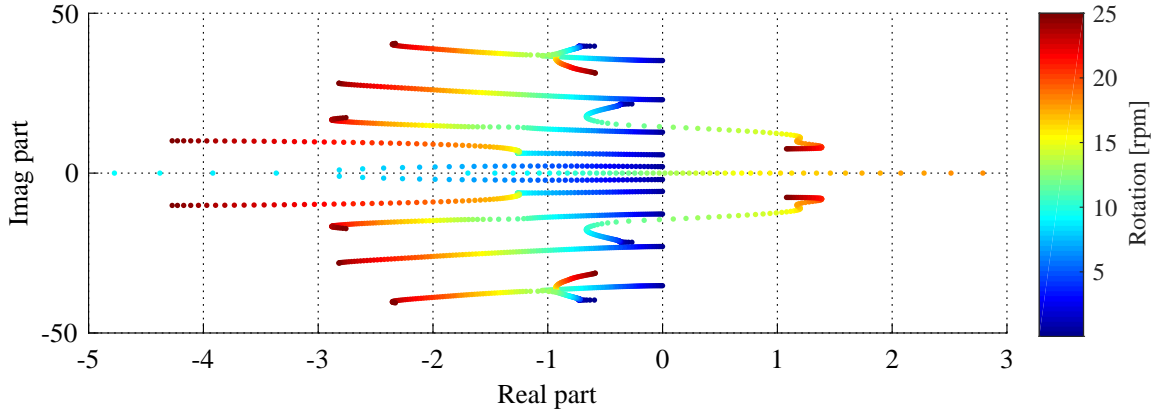
The flutter occurs in 12.35 rpm as shown by Fig. 4.2 considering only the rotation of the blade. The flutter takes the influence of all modes but it is the 1st torsional mode that the flutter occurs when the damping becomes negative (Fig. 4.2b) or when the real part of the complex conjugate pairs of the mode becomes positive as shown in Fig. 4.2a. The cause for the modes to intersect observed in Fig. 4.2c is believed to be the pre-stress effects associated with the centrifugal and gravitational loads. The model has also predicted a divergence in 13.03 rpm when the imaginary part of eigenvalues (λ) related to the 1st flapwise bending mode becomes zero and the real part positive as can be seen in the Fig. 4.2a. For the flutter speed considering only the blade rotation, the results were in the same range as the ones found in the literature as shown on Table 4.3, but unfortunately the other authors did not compute the divergence speed to compare the results.

Author	Flutter speed (rpm)
Present work	12.35
(RESOR <i>et al.</i> , 2012)	9.37
(OWENS <i>et al.</i> , 2013)	13.05
(POURAZARM <i>et al.</i> , 2016)	16.91

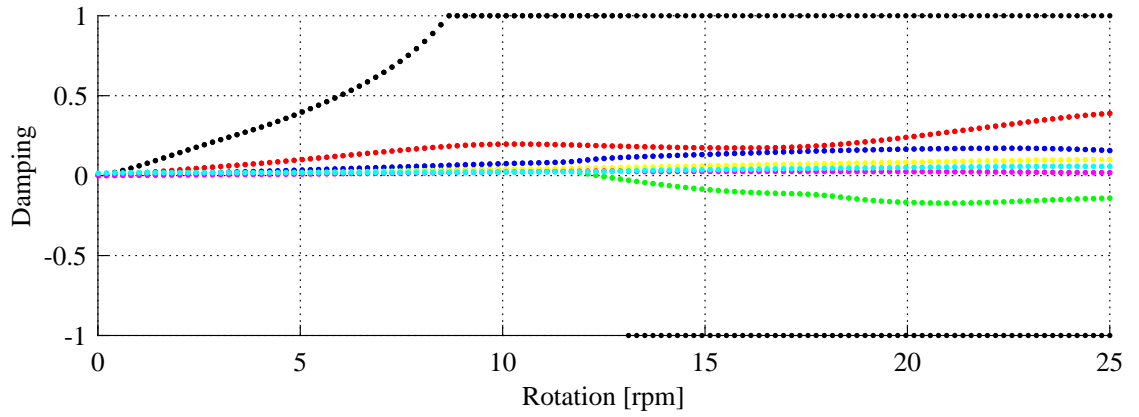
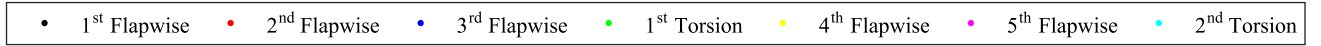
TABLE 4.3 – Flutter speed comparison with other authors.

Figs. 4.3 and 4.4 indicate flutter occurrence at 12.29 and 12.15 rpm, respectively, which is slightly lower than Fig. 4.2, as it is consequence of the wind velocity that increases V_{rel} in Eq. (3.50). The results also indicate a divergence velocity at 12.97 and 12.82 rpm, respectively. It can be observed from Figs. 4.3b and 4.4b that the 1st flapwise bending mode damping is slightly above in comparison with Fig. 4.2b for low Ω 's, this is also due V_{rel} which influence the aerodynamic matrices.

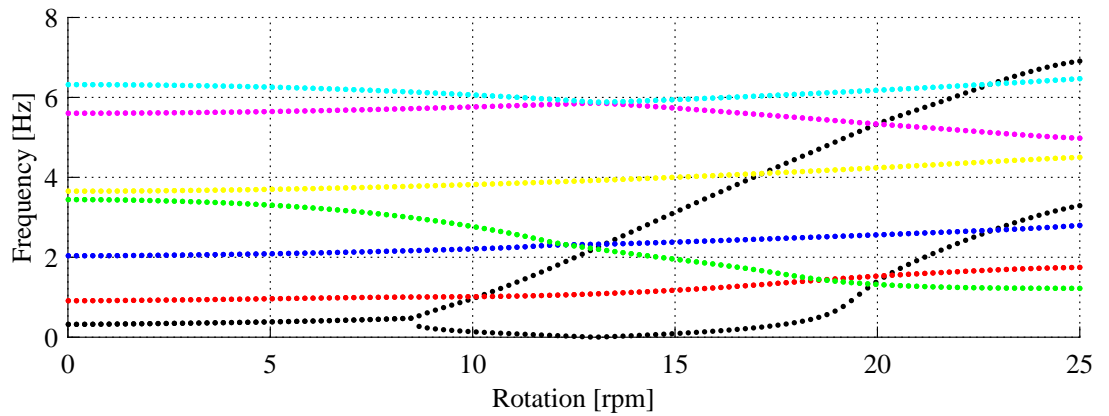
For all plots the Theodorsen function has given satisfactory convergence results in relation to the prediction of coupled mode flutter.



(a) – Root-loci of SNL100-00 blade.

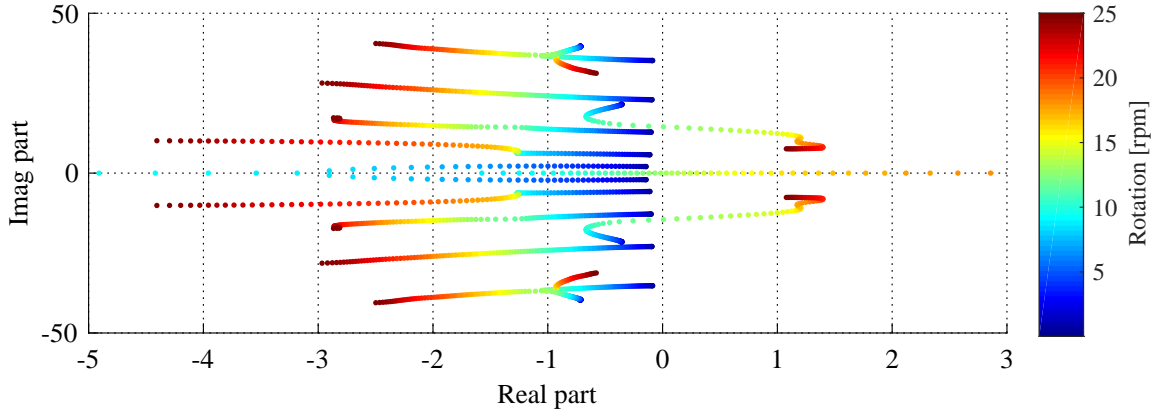


(b) – Damping of SNL100-00 blade.

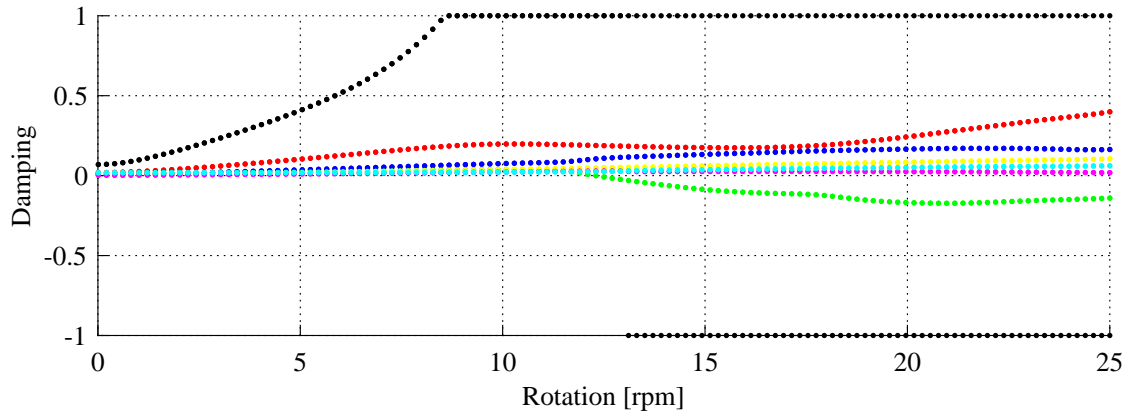
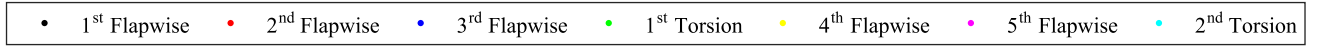


(c) – Frequency response of SNL100-00 blade.

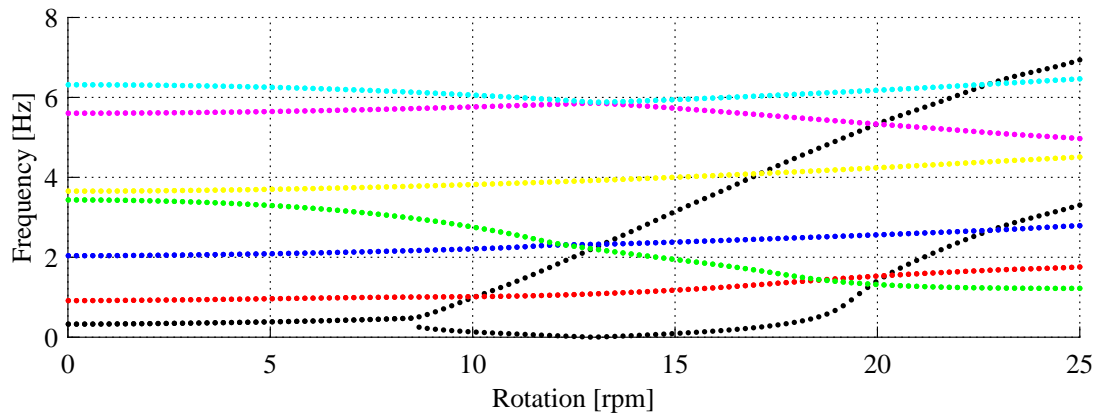
FIGURE 4.2 – Aeroelastic prediction of SNL100-00 blade using Theodorsen function in rotation only.



(a) – Root-loci of SNL100-00 blade.

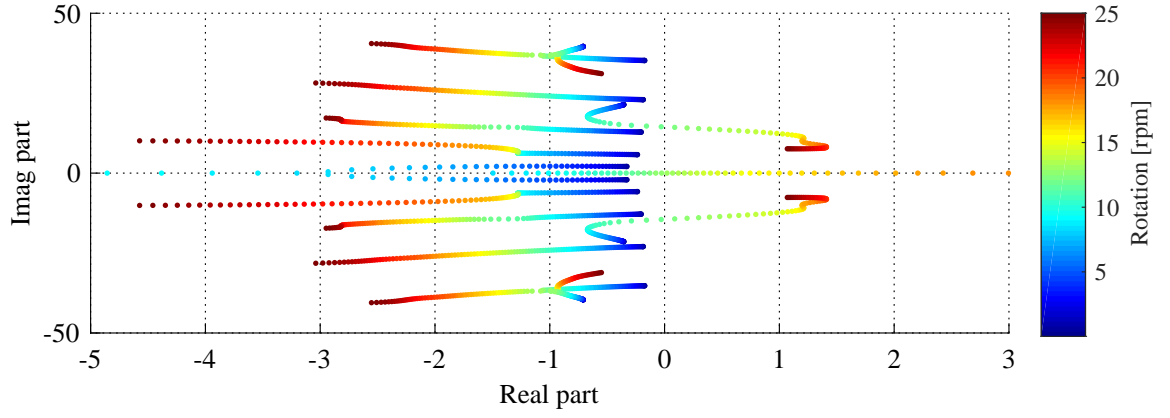


(b) – Damping of SNL100-00 blade.

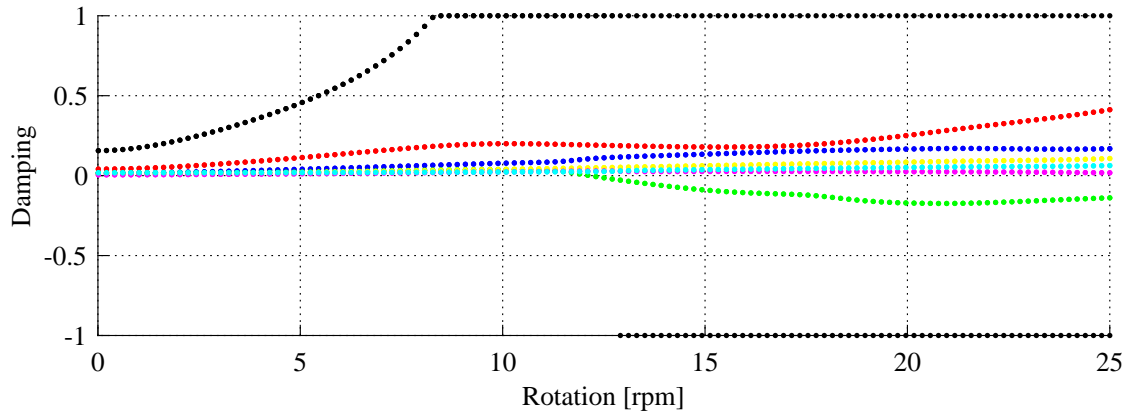
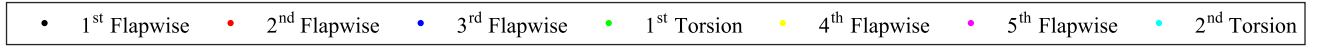


(c) – Frequency response of SNL100-00 blade.

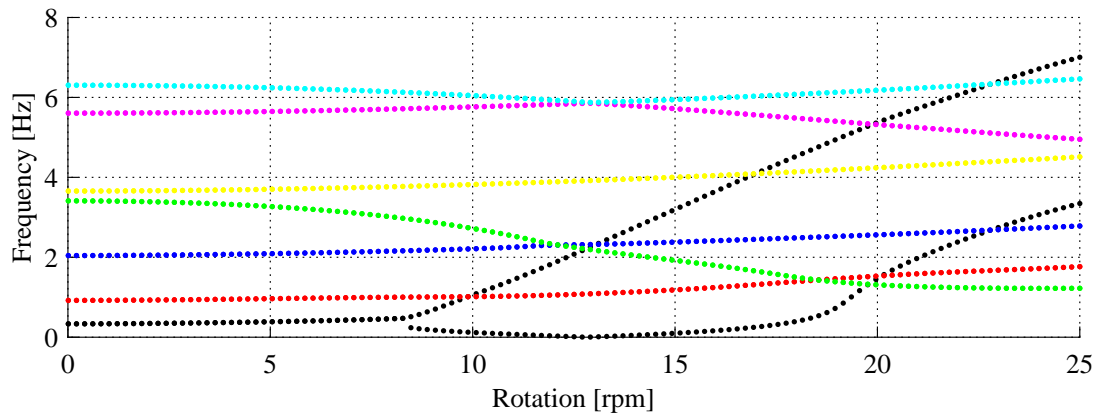
FIGURE 4.3 – Aeroelastic prediction of SNL100-00 blade using Theodorsen function with $V_\infty = 10$ m/s.



(a) – Root-loci of SNL100-00 blade.



(b) – Damping of SNL100-00 blade.



(c) – Frequency response of SNL100-00 blade.

FIGURE 4.4 – Aeroelastic prediction of SNL100-00 blade using Theodorsen function with $V_\infty = 20$ m/s.

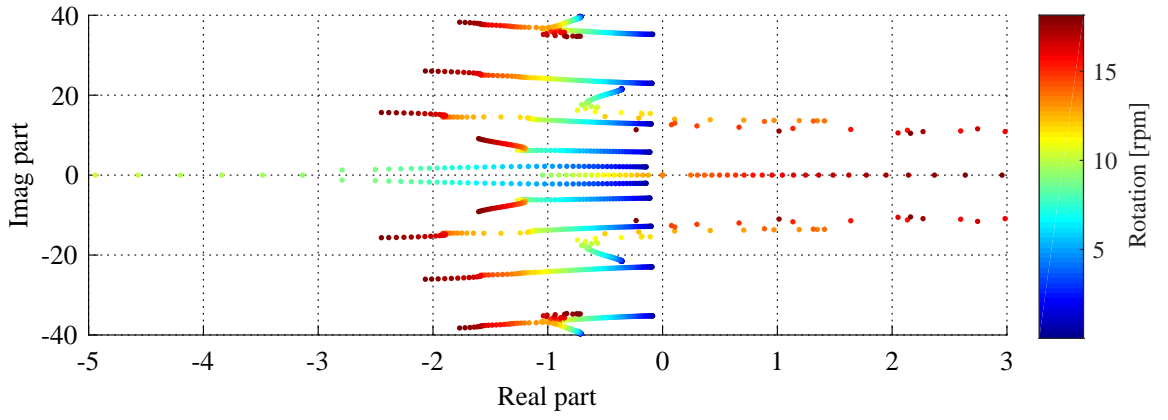
4.3 Aeroelastic analysis using Loewy's function

As the effects of blades wake can not be neglected, instead of using C , the Loewy's function C' gives a better representation for rotating blades because it considers the flow velocity of the wind in the shed vorticity of each blade. Figs. 4.5 and 4.6 shows the frequency and damping response for a wind velocity of 10 and 20 m/s respectively.

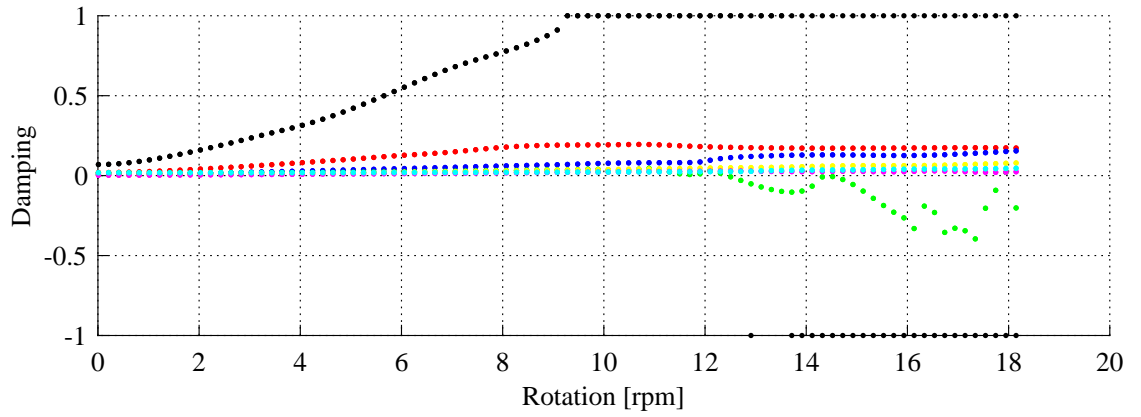
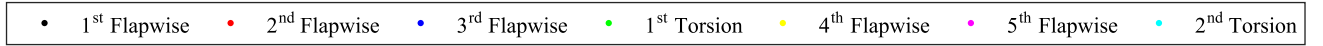
Loewy's function responses shows that the flutter rotational speed slightly increases with the wind velocity in comparison with Theodorsen's function. For 10 and 20 m/s the flutter rotation speeds are 12.44 and 12.23 rpm, respectively and the divergence occurs in 12.91 and 12.71 rpm, respectively. However this method presents numerical convergence instability problems in the 1st torsion mode when the rotation is increased, mostly for lower V_∞ 's, which is the reason why the $V_\infty = 0$ m/s was not shown. For the case of 10 m/s the numerical convergence instability starts in 15.93 rpm and for 20 m/s it starts in 18.14 rpm. This issue is maybe a limitation of the PK method with Loewy's function.

As the rotation increases in Figs. 4.5b and 4.6b the oscillatory behavior of the damping plot related to the 1st torsional mode appears. This behavior is common for Loewy's function which has been discussed in its own work (LOEWY, 1957) and also discussed recently in (FILIPPI; CARRERA, 2015). This happens because the value of γ start to decrease due the increase in Ω , then the amplitude of oscillatory behavior increases as shown in the damping diagram Figs. 4.5b and 4.6b.

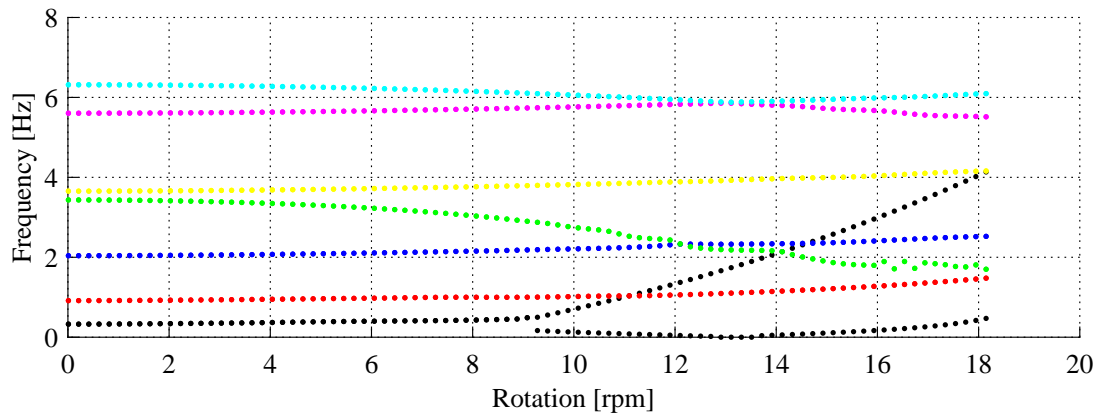
The Loewy's function gets near to Theodorsen's function when the wind velocity is high, this decreases the shed vorticity effect seen by each blade of the rotor, then the oscillatory behavior decreases because γ increases. The Loewy's function tends to yield the same results of Theodorsen's function as γ increases and so the method has a better convergence. The variation of γ and μ is show in Fig. 4.7.



(a) – Root-loci of SNL100-00 blade.

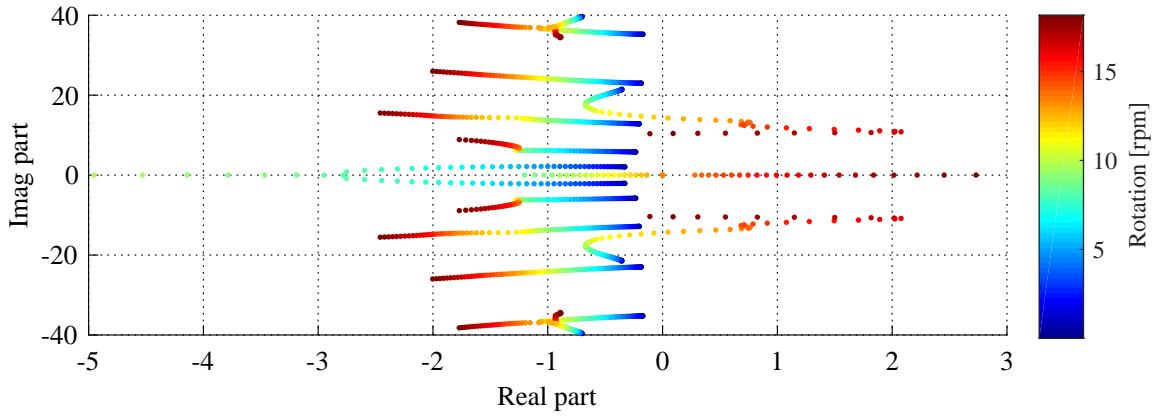


(b) – Damping of SNL100-00 blade.

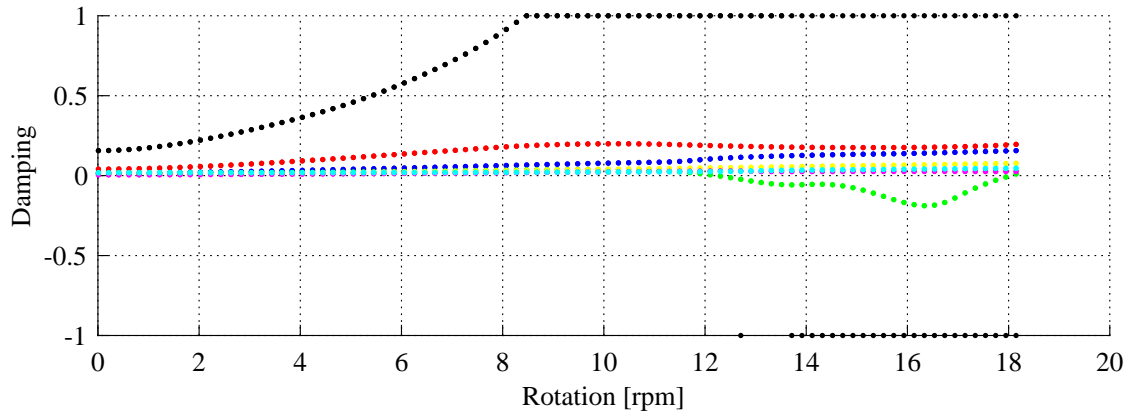
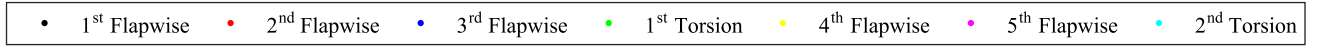


(c) – Frequency response of SNL100-00 blade.

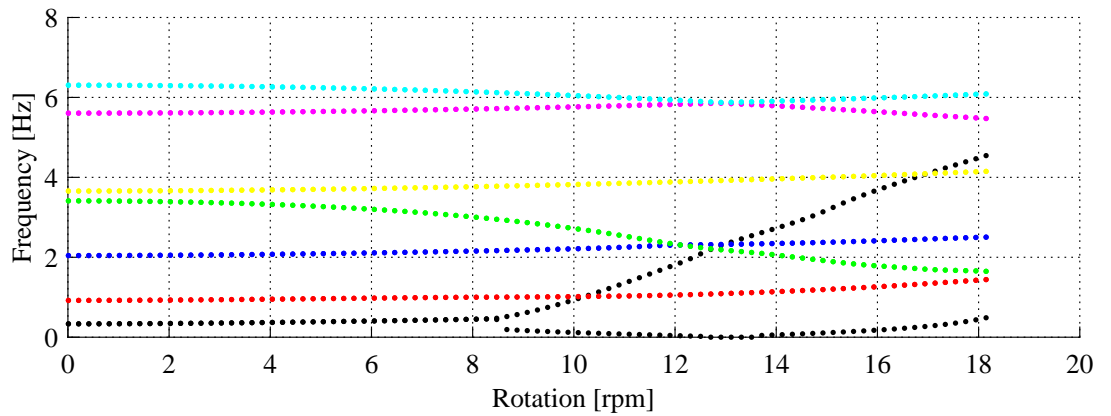
FIGURE 4.5 – Aeroelastic prediction of SNL100-00 blade using Loewy function with $V_\infty = 10$ m/s.



(a) – Root-loci of SNL100-00 blade.

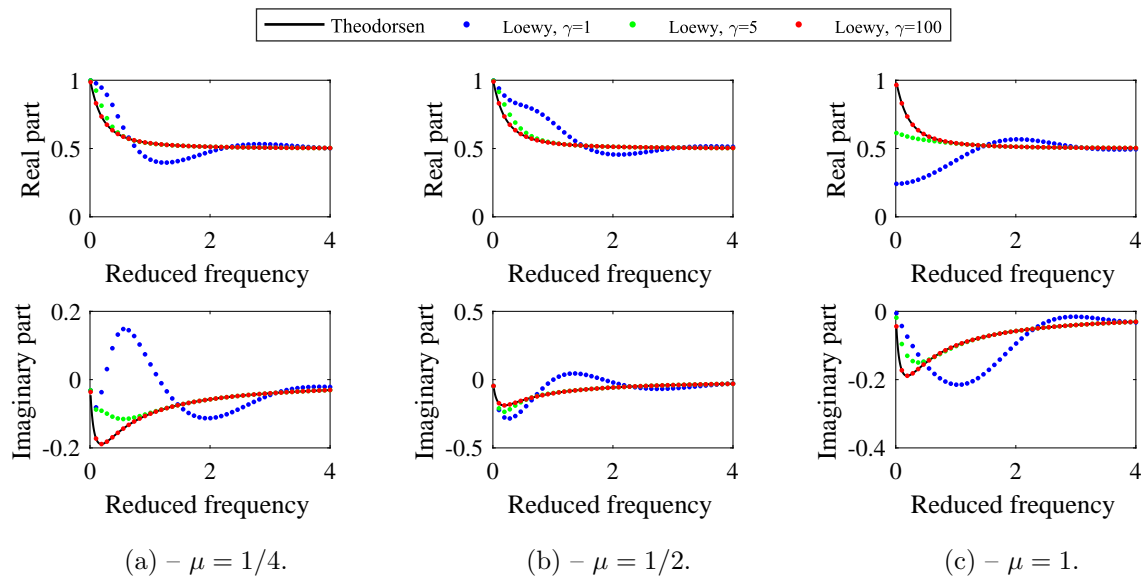


(b) – Damping of SNL100-00 blade.



(c) – Frequency response of SNL100-00 blade.

FIGURE 4.6 – Aeroelastic prediction of SNL100-00 blade using Loewy function with $V_\infty = 20$ m/s.

FIGURE 4.7 – Theodorsen's and Loewy's function with different μ 's and γ 's.

5 Other applications

This chapter has the objective to show different applications that uses the same hierarchical Rayleigh-Ritz based model described in the Chapters 3 and 4 by comparing results with literature models as (DONADON *et al.*, 2010) and (RUGGERI, 2015).

(DONADON *et al.*, 2010) proposed a variational model based on the Hamilton principle combined with the Rayleigh-Ritz method to predict the natural frequencies of an idealized gas turbine blade under different rotation speeds. The results predicted by Donadon's model were compared with FE results obtained using ANSYS.

(RUGGERI, 2015) developed an analysis using Abaqus/ZAERO and MSC.Nastran/ZAERO using the subsonic ZONA6 g-Method in a half-wing with a ballast on the tip. (RUGGERI, 2015) studied both the linear and non-linear geometric case, but as means to validate the present work only the linear case is compared.

5.1 Gas turbine blade

The current section presents the formulation and a modal analysis of a gas turbine blade developed in the work of (DONADON *et al.*, 2010). The material properties and dimensions of the blade is show in Table 5.1. A simplified image describing the geometry and dynamic system of the rotor is show in Fig. 5.1.

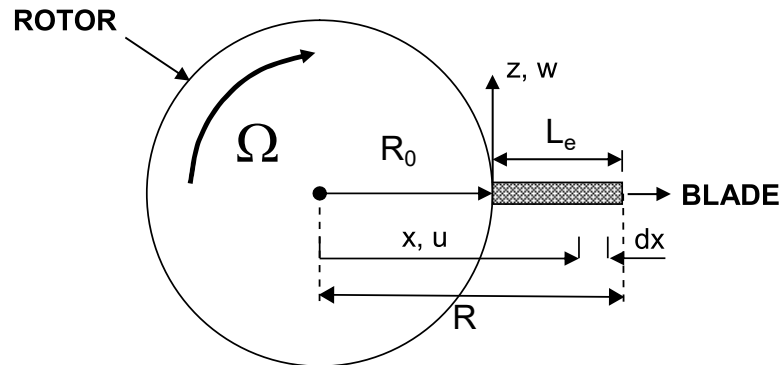


FIGURE 5.1 – Simplified dynamic model of a gas turbine rotor, (DONADON *et al.*, 2010).

To compute the stress stiffening effect caused by the blade rotation as the influence in

Material	Conventional steel
ρ_{st}	7800 kg/m ³
Elastic modullus (E)	200 GPa
Shear modullus (G)	80 GPa
L_e	0.84 m
Thickness	0.02 m
Wide	0.14 m

TABLE 5.1 – Material properties of the cantilever beam.

the bending vibration model. As describe in Section 3.1.1 the same procedure was applied but neglecting the effect of the blade position or considering in $\varphi = 0^\circ$. Then, neglecting the effect of gravity, $EAu_{,x}$ is,

$$EA \frac{\partial u}{\partial x} = m\Omega \left[\frac{(R_0 + L_e)^2}{2} - \frac{x^2}{2} \right] \quad (5.1)$$

5.1.1 Modal analysis

The current analysis has used the same number of terms in (DONADON *et al.*, 2010), where it was six hierarchical polynomials and two boundary terms. The mode shape of the bending modes is show in Fig. 5.2. The frequency response with $\Omega = 0$ rpm and $\Omega = 9550$ rpm is show in Tables 5.2 and 5.3.

Bending modes	ANSYS model	(DONADON <i>et al.</i> , 2010) model	Present work
1	23.30 Hz	23.11 Hz	23.1857 Hz
2	145.64 Hz	144.83 Hz	145.3020 Hz
3	406.82 Hz	405.55 Hz	406.8504 Hz

TABLE 5.2 – $\Omega = 0$ rpm.

It should be notice that ANSYS model was also employed in (DONADON *et al.*, 2010). The results with the hierarchical Rayleigh-Ritz shows that the employed method has a good agreement with the results reported by (DONADON *et al.*, 2010).

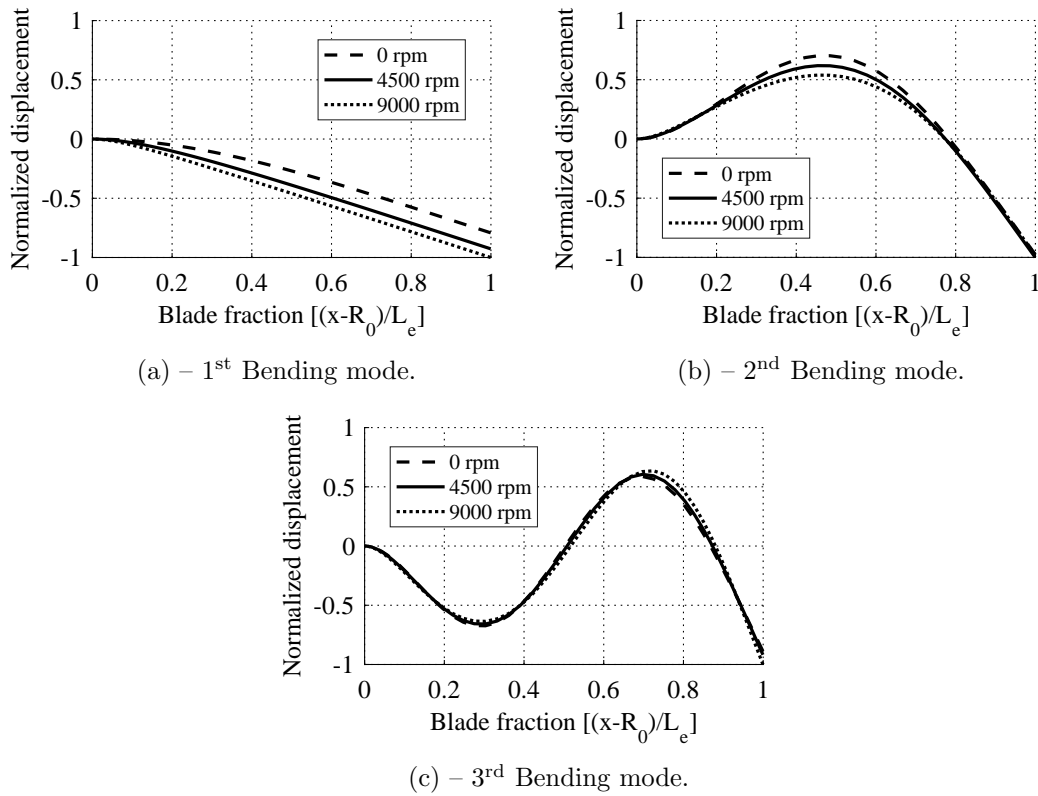


FIGURE 5.2 – Bending modes.

Bending modes	ANSYS model	(DONADON <i>et al.</i> , 2010) model	Present work
1	166.42 Hz	167.31 Hz	166.4564 Hz
2	426.24 Hz	431.80 Hz	426.4381 Hz
3	772.22 Hz	794.39 Hz	772.9926 Hz

TABLE 5.3 – $\Omega = 9550$ rpm

5.2 Half plate like wing with a ballast on the tip

This section presents the formulation as modal and aeroelastic analyses of a fixed half-wing with a ballast attached to the tip where the ballast has a $d_{\text{offset}} = -5$ mm offset backwards from the half-wing center of gravity as shown in Fig. 5.3, the material and geometric properties is shown in Table 5.4.

The proposed aeroelastic model was validated with the work of (RUGGERI, 2015).

The half-wing structural model formulation includes the bending and torsional vibration model, the unsteady aerodynamic model assumes the plate with $C_{l,\alpha} = 5.34$ computed in the work of (RUGGERI, 2015) and the aerodynamic center is positioned at the quarter chord.

Half-wing properties	
Material	Aluminium 2024-T3
ρ_{st}	2780 kg/m ³
Elastic modullus (E)	69 GPa
Shear modullus (G)	25.94 GPa
L_{hw}	0.35 m
h_{hw}	8.124E-4 m
b_{hw}	0.04 m
Ballast properties	
m_{bl}	0.03458 kg
I_{xx}	1.858E-5 kg.m ²

TABLE 5.4 – Material and geometric properties of the half-wing and ballast.

5.2.1 Bending vibration model

The bending vibration model different from Section 3.1.2 does not account any pre-stress effect for a fixed wing, but it has a concentrated mass on the tip, then T_w and U_w becomes,

$$T_w = \frac{1}{2} \int_0^{L_{hw}} \rho_{st} A (\dot{w})^2 dx + \frac{1}{2} m_{bl} (\dot{w})^2 \Big|_{L_{hw}} \quad (5.2)$$

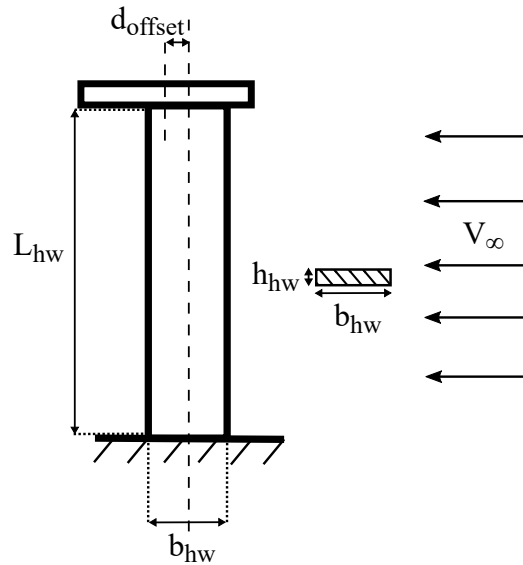


FIGURE 5.3 – Half-wing with a ballast on the tip.

$$U_w = \frac{1}{2} \int_0^{L_{hw}} EI \left(\frac{\partial^2 w}{\partial x^2} \right)^2 dx \quad (5.3)$$

Applying Hamilton's principle,

$$\delta \int_{t_1}^{t_2} (T_w - U_w) dt = 0 \quad (5.4)$$

The eigenproblem becomes,

$$\underbrace{\{[\mathbf{K}_w] - \omega^2 [\mathbf{M}_w]\}}_{\text{Eigenproblem}} \{\mathcal{A}_w\} e^{i\omega t} = 0 \quad (5.5)$$

where,

$$[\mathbf{M}_w] = \rho_{st} A \int_0^{L_{hw}} [\mathcal{N}^w]^T [\mathcal{N}^w] dx + m_{bl} [\mathcal{N}^w]^T [\mathcal{N}^w] \Big|_{L_{hw}} \quad (5.6)$$

$$[\mathbf{K}_w] = \int_0^{L_{hw}} EI [\mathcal{N}_{,xx}^w]^T [\mathcal{N}_{,xx}^w] dx \quad (5.7)$$

5.2.2 Torsional vibration model

For the torsional vibration model due to the mass on the tip, it is applied the parallel axis theorem, then T_β becomes,

$$T_\beta = \frac{1}{2} \int_0^{L_{hw}} I_\theta \rho_{st} (\dot{\beta})^2 dx + \frac{1}{2} I_\theta^{bl} (\dot{\beta})^2 \Big|_{L_{hw}} \quad (5.8)$$

where,

$$I_\theta = \frac{b_{hw} h_{hw}^3}{12} + \frac{h_{hw} b_{hw}^3}{12}; \quad I_\theta^{bl} = I_{xx} + m_{bl} d_{\text{offset}}^2 \quad (5.9)$$

As the strain energy U_β ,

$$U_\beta = \frac{1}{2} \int_0^{L_{hw}} GJ \left(\frac{\partial \beta}{\partial x} \right)^2 dx + \frac{1}{2} \int_0^{L_{hw}} E\Gamma \left(\frac{\partial^2 \beta}{\partial x^2} \right)^2 dx \quad (5.10)$$

After applying Hamilton's principle the eigenproblem becomes,

$$\underbrace{\{[\mathbf{K}_{\beta_1}] + [\mathbf{K}_{\beta_2}] - \omega^2[\mathbf{M}_{\beta}]\}}_{\text{Eigenproblem}} \{\mathcal{A}_{\beta}\} e^{i\omega t} = \{0\} \quad (5.11)$$

where,

$$[\mathbf{M}_{\beta}] = \int_0^{L_{hw}} I_{\theta} \rho_{st} [\mathcal{N}^{\beta}]^T [\mathcal{N}^{\beta}] dx + I_{\theta}^{bl} [\mathcal{N}^{\beta}]^T [\mathcal{N}^{\beta}] \Big|_{L_{hw}} \quad (5.12)$$

$$[\mathbf{K}_{\beta_1}] = \int_0^{L_{hw}} GJ [\mathcal{N}_{,x}^{\beta}]^T [\mathcal{N}_{,x}^{\beta}] dx \quad (5.13)$$

$$[\mathbf{K}_{\beta_2}] = \int_0^{L_{hw}} E\Gamma [\mathcal{N}_{,xx}^{\beta}]^T [\mathcal{N}_{,xx}^{\beta}] dx \quad (5.14)$$

5.2.3 Unsteady aerodynamic model formulation

The unsteady aerodynamic formulation now considering $c_{l,\alpha} = 5.34$ for the entire wing as the position of the aerodynamic center is in the quarter chord, then $a_{c,n} = (a.c - b)/b = -0.5$ (RUGGERI, 2015). Using the same procedure as describe in Section 3.2, L and M are,

$$\begin{aligned} L = & \pi \rho_f b^2 \left(\ddot{h}(x, t) + V_{\infty} \dot{\theta}(x, t) - ba \ddot{\theta}(x, t) \right) \\ & + c_{l,\alpha} \rho_f V_{\infty} b C(k) \left[\dot{h}(x, t) + V_{\infty} \theta(x, t) + b \left(\frac{c_{l,\alpha}}{2\pi} - \frac{1}{2} - a \right) \dot{\theta}(x, t) \right] \end{aligned} \quad (5.15)$$

$$\begin{aligned} M = & \pi \rho_f b^2 \left[ba \ddot{h}(x, t) - V_{\infty} b \left(\frac{c_{l,\alpha}}{2\pi} - \frac{1}{2} - a \right) \dot{\theta}(x, t) - b^2 \left(\frac{1}{8} + a^2 \right) \ddot{\theta}(x, t) \right] \\ & + c_{l,\alpha} \rho_f V_{\infty} b^2 \left(a + \frac{1}{2} \right) C(k) \left[\dot{h}(x, t) + V_{\infty} \theta(x, t) + b \left(\frac{c_{l,\alpha}}{2\pi} - \frac{1}{2} - a \right) \dot{\theta}(x, t) \right] \end{aligned} \quad (5.16)$$

Now expressing L and M in a real form,

$$\begin{aligned}
L_h &= -\pi k^2 - c_{l,\alpha} \mathcal{G} k \\
L_{\dot{h}} &= c_{l,\alpha} \mathcal{F} \\
L_\theta &= \pi k^2 a + c_{l,\alpha} \mathcal{F} - c_{l,\alpha} \mathcal{G} k \left(\frac{c_{l,\alpha}}{2\pi} - \frac{1}{2} - a \right) \\
L_{\dot{\theta}} &= \pi + c_{l,\alpha} \mathcal{F} \left(\frac{c_{l,\alpha}}{2\pi} - \frac{1}{2} - a \right) + c_{l,\alpha} \frac{\mathcal{G}}{k} \\
L &= \rho_f V_\infty^2 \left(L_h h(x, t) + L_{\dot{h}} \frac{b \dot{h}(x, t)}{V_\infty} + L_\theta b \theta(x, t) + L_{\dot{\theta}} \frac{b^2 \dot{\theta}(x, t)}{V_\infty} \right)
\end{aligned} \tag{5.17}$$

$$\begin{aligned}
M_h &= -\pi k^2 a - c_{l,\alpha} k \left(a + \frac{1}{2} \right) \mathcal{G} \\
M_{\dot{h}} &= c_{l,\alpha} \left(a + \frac{1}{2} \right) \mathcal{F} \\
M_\theta &= \pi k^2 \left(\frac{1}{8} + a^2 \right) + c_{l,\alpha} \mathcal{F} \left(a + \frac{1}{2} \right) \\
&\quad - c_{l,\alpha} k \mathcal{G} \left(a + \frac{1}{2} \right) \left(\frac{c_{l,\alpha}}{2\pi} - \frac{1}{2} - a \right) \\
M_{\dot{\theta}} &= -\pi k \left(\frac{c_{l,\alpha}}{2\pi} - \frac{1}{2} - a \right) + c_{l,\alpha} k \mathcal{F} \left(a + \frac{1}{2} \right) \left(\frac{c_{l,\alpha}}{2\pi} - \frac{1}{2} - a \right) \\
&\quad + c_{l,\alpha} \frac{\mathcal{G}}{k} \left(a + \frac{1}{2} \right) \\
M &= \rho_f V_\infty^2 \left(M_h b h(x, t) + M_{\dot{h}} \frac{b^2 \dot{h}(x, t)}{V_\infty} + M_\theta b^2 \theta(x, t) + M_{\dot{\theta}} \frac{b^3 \dot{\theta}(x, t)}{V_\infty} \right)
\end{aligned} \tag{5.18}$$

Writing in matrix form:

$$\begin{Bmatrix} -L \\ M \end{Bmatrix} = \rho_f V_\infty [\mathbf{B}] \begin{Bmatrix} \dot{h}(x, t) \\ \dot{\theta}(x, t) \end{Bmatrix} + \rho_f V_\infty^2 [\mathbf{C}] \begin{Bmatrix} h(x, t) \\ \theta(x, t) \end{Bmatrix} \tag{5.19}$$

where:

$$[\mathbf{B}] = \begin{bmatrix} -b L_{\dot{h}} & -b^2 L_{\dot{\theta}} \\ b^2 M_{\dot{h}} & b^3 M_{\dot{\theta}} \end{bmatrix} \tag{5.20}$$

$$[\mathbf{C}] = \begin{bmatrix} -L_h & -bL_\theta \\ bM_h & b^2M_\theta \end{bmatrix} \quad (5.21)$$

5.2.4 Aeroelastic model formulation

For the aeroelastic model formulation, the same process of Section 3.3 is applied, the difference are that the mass on the tip of the half plate generates a coupling between the bending and twisting terms as show by $T_{w,\beta}$, where,

$$\begin{aligned} T_{w,\beta} = & \frac{1}{2} \int_0^{L_{hw}} \begin{Bmatrix} \dot{h}(x,t) \\ \dot{\theta}(x,t) \end{Bmatrix}^T \begin{bmatrix} m & S_{sc} \\ S_{sc} & \rho_{st}I_\theta \end{bmatrix} \begin{Bmatrix} \dot{h}(x,t) \\ \dot{\theta}(x,t) \end{Bmatrix} dx \\ & + \frac{1}{2} \begin{Bmatrix} \dot{h}(x,t) \\ \dot{\theta}(x,t) \end{Bmatrix}^T \begin{bmatrix} m_{bl} & S_{sc}^{bl} \\ S_{sc}^{bl} & I_\theta^{bl} \end{bmatrix} \begin{Bmatrix} \dot{h}(x,t) \\ \dot{\theta}(x,t) \end{Bmatrix} \Big|_{L_{hw}} \end{aligned} \quad (5.22)$$

where,

$$\begin{aligned} S_{sc} &= x_\theta \rho_{st} A & S_{sc}^{bl} &= x_\theta^{bl} \rho_{st} A \\ x_\theta &= c.g - e.a & x_\theta^{bl} &= c.g - e.a - d_{\text{offset}} \end{aligned} \quad (5.23)$$

Then Eq. (5.22) can be written and simplified as follows,

$$\begin{aligned} T_{w,\beta} = & \frac{1}{2} \int_0^{L_{hw}} \begin{Bmatrix} \{\underline{\dot{h}}(t)\} \\ \{\underline{\dot{\theta}}(t)\} \end{Bmatrix}^T \begin{bmatrix} [\mathcal{W}] & [0]_{1,m} \\ [0]_{1,n} & [\mathcal{B}] \end{bmatrix}^T \begin{bmatrix} m & S_{sc} \\ S_{sc} & \rho_{st}I_\theta \end{bmatrix} \begin{bmatrix} [\mathcal{W}] & [0]_{1,m} \\ [0]_{1,n} & [\mathcal{B}] \end{bmatrix} \begin{Bmatrix} \{\underline{\dot{h}}(t)\} \\ \{\underline{\dot{\theta}}(t)\} \end{Bmatrix} dx \\ & + \frac{1}{2} \begin{Bmatrix} \{\underline{\dot{h}}(t)\} \\ \{\underline{\dot{\theta}}(t)\} \end{Bmatrix}^T \begin{bmatrix} [\mathcal{W}] & [0]_{1,m} \\ [0]_{1,n} & [\mathcal{B}] \end{bmatrix}^T \begin{bmatrix} m_{bl} & S_{sc}^{bl} \\ S_{sc}^{bl} & I_\theta^{bl} \end{bmatrix} \begin{bmatrix} [\mathcal{W}] & [0]_{1,m} \\ [0]_{1,n} & [\mathcal{B}] \end{bmatrix} \begin{Bmatrix} \{\underline{\dot{h}}(t)\} \\ \{\underline{\dot{\theta}}(t)\} \end{Bmatrix} \Big|_{L_{hw}} \end{aligned} \quad (5.24)$$

then,

$$T_{w,\beta} = \frac{1}{2} \begin{Bmatrix} \{\underline{\dot{h}}(t)\} \\ \{\underline{\dot{\theta}}(t)\} \end{Bmatrix}^T [\tilde{\mathbf{M}}] \begin{Bmatrix} \{\underline{\dot{h}}(t)\} \\ \{\underline{\dot{\theta}}(t)\} \end{Bmatrix} \quad (5.25)$$

The mass, stiffness and damping matrices are written as,

$$\begin{aligned} [\tilde{\mathbf{M}}] &= \int_0^{L_{hw}} \begin{bmatrix} [\mathcal{W}] & [0]_{1,m} \\ [0]_{1,n} & [\mathcal{B}] \end{bmatrix}^T \begin{bmatrix} m & S_{sc} \\ S_{sc} & \rho I_\theta \end{bmatrix} \begin{bmatrix} [\mathcal{W}] & [0]_{1,m} \\ [0]_{1,n} & [\mathcal{B}] \end{bmatrix} dx \\ &+ \left. \begin{bmatrix} [\mathcal{W}] & [0]_{1,m} \\ [0]_{1,n} & [\mathcal{B}] \end{bmatrix}^T \begin{bmatrix} m_{bl} & S_{sc}^{bl} \\ S_{sc}^{bl} & I_\theta^{bl} \end{bmatrix} \begin{bmatrix} [\mathcal{W}] & [0]_{1,m} \\ [0]_{1,n} & [\mathcal{B}] \end{bmatrix} \right|_{L_{hw}} \end{aligned} \quad (5.26)$$

$$\begin{aligned} [\tilde{\mathbf{K}}] &= \int_0^{L_{hw}} \left(\begin{bmatrix} [\mathcal{W}_{,xx}] & [0]_{1,m} \\ [0]_{1,n} & [\mathcal{B}_{,xx}] \end{bmatrix}^T \begin{bmatrix} EI & 0 \\ 0 & E\Gamma \end{bmatrix} \dots \right. \\ &\quad \left. \begin{bmatrix} [\mathcal{W}_{,xx}] & [0]_{1,m} \\ [0]_{1,n} & [\mathcal{B}_{,xx}] \end{bmatrix} + \begin{bmatrix} [\mathcal{W}_{,x}] & [0]_{1,m} \\ [0]_{1,n} & [\mathcal{B}_{,x}] \end{bmatrix}^T \dots \right. \\ &\quad \left. \begin{bmatrix} 0 & 0 \\ 0 & GJ \end{bmatrix} \begin{bmatrix} [\mathcal{W}_{,x}] & [0]_{1,m} \\ [0]_{1,n} & [\mathcal{B}_{,x}] \end{bmatrix} \right) dx \end{aligned} \quad (5.27)$$

$$[\tilde{\mathbf{B}}] = \int_0^{L_{hw}} \begin{bmatrix} [\mathcal{W}] & [0]_{1,m} \\ [0]_{1,n} & [\mathcal{B}] \end{bmatrix}^T [\mathbf{B}] \begin{bmatrix} [\mathcal{W}] & [0]_{1,m} \\ [0]_{1,n} & [\mathcal{B}] \end{bmatrix} dx \quad (5.28)$$

$$[\tilde{\mathbf{C}}] = \int_0^{L_{hw}} \begin{bmatrix} [\mathcal{W}] & [0]_{1,m} \\ [0]_{1,n} & [\mathcal{B}] \end{bmatrix}^T [\mathbf{C}] \begin{bmatrix} [\mathcal{W}] & [0]_{1,m} \\ [0]_{1,n} & [\mathcal{B}] \end{bmatrix} dx \quad (5.29)$$

$$[\tilde{\mathbf{D}}] = \int_0^{L_{hw}} \begin{bmatrix} [\mathcal{W}] & [0]_{1,m} \\ [0]_{1,n} & [\mathcal{B}] \end{bmatrix}^T \begin{bmatrix} c_h & 0 \\ 0 & c_\theta \end{bmatrix} \begin{bmatrix} [\mathcal{W}] & [0]_{1,m} \\ [0]_{1,n} & [\mathcal{B}] \end{bmatrix} dx \quad (5.30)$$

From Section 3.3, then,

$$[Q] = \begin{bmatrix} [0] & [\mathbf{I}] \\ [\tilde{\mathbf{M}}]^{-1} \left(\rho_f [\tilde{\mathbf{C}}] - [\tilde{\mathbf{K}}] \right) & [\tilde{\mathbf{M}}]^{-1} \left(\rho_f [\tilde{\mathbf{B}}] - [\tilde{\mathbf{D}}] \right) \end{bmatrix} \quad (5.31)$$

As $\mathbf{x} = \mathbf{x}_0 e^{\lambda t}$, then the eigenproblem is:

$$\{[\mathbf{I}]\lambda - [Q]\} \mathbf{x}_0 = \{0\} \text{ or } \{[Q] - \lambda[\mathbf{I}]\} \mathbf{x}_0 = \{0\} \quad (5.32)$$

The eigenvalues λ of the system matrix Q :

$$\lambda_s = \zeta_s \omega_s \pm i \omega_s \sqrt{1 - \zeta_s^2} \quad (5.33)$$

for $\rightarrow s = 1, \dots, (\mathbf{m} + \mathbf{n}) \times 2$

$$\omega_s = \sqrt{(\text{Real}(\lambda_s))^2 + (\text{Imag}(\lambda_s))^2}; \quad \zeta_s = -\frac{\text{Real}(\lambda_s)}{\omega_s} \quad (5.34)$$

The corresponding eigenvectors take the form:

$$\{\mathbf{x}_0\}_s = \begin{Bmatrix} \{\underline{q}\}_s \\ \lambda_s \{\underline{q}\}_s \end{Bmatrix} \quad (5.35)$$

The PK method for a fixed wing is shown in Fig. 5.4.

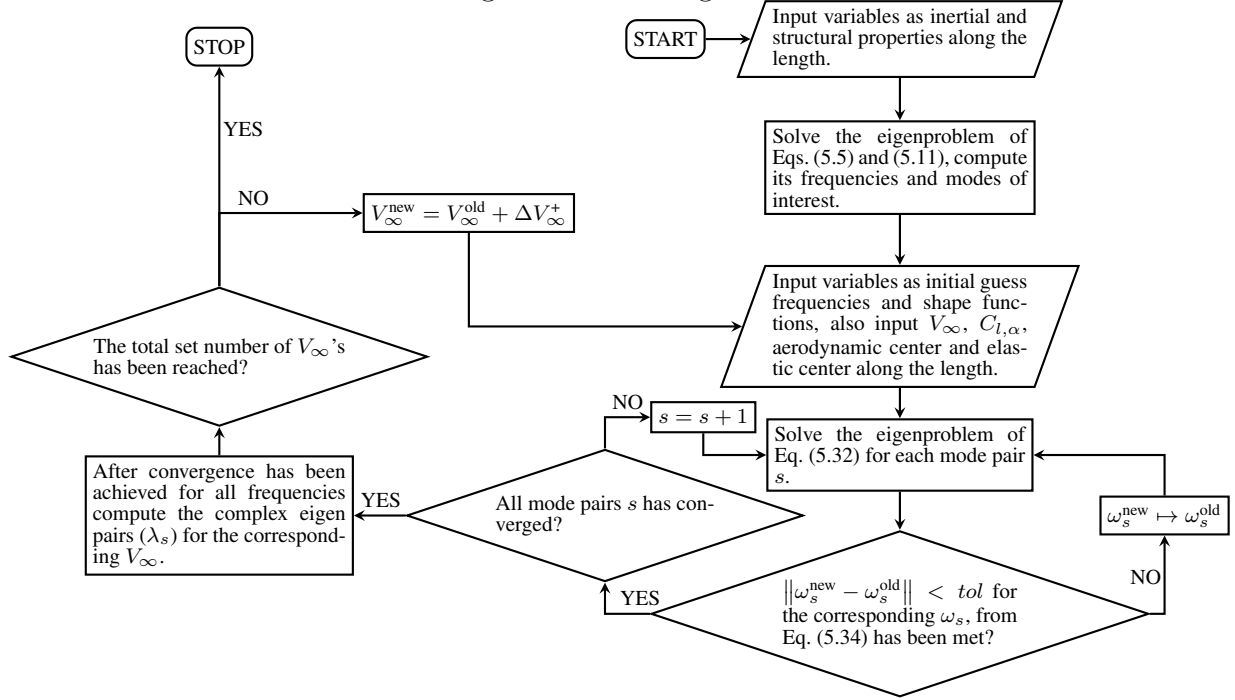
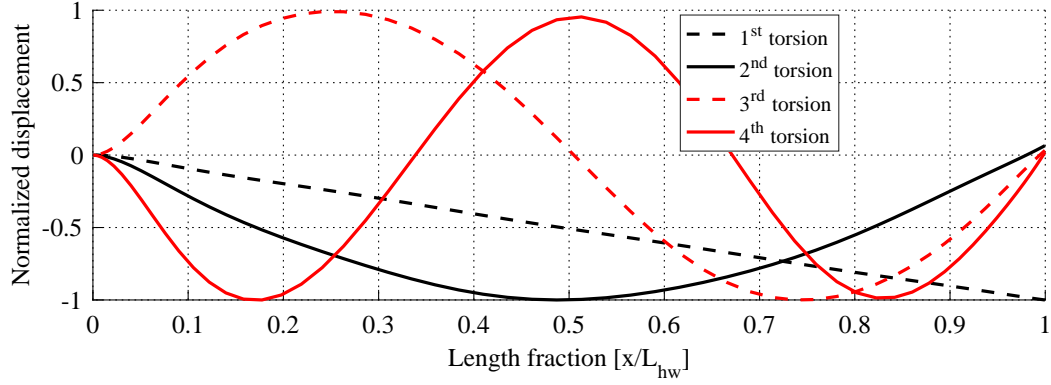


FIGURE 5.4 – Flowchart explaining the PK method for a fixed wing.

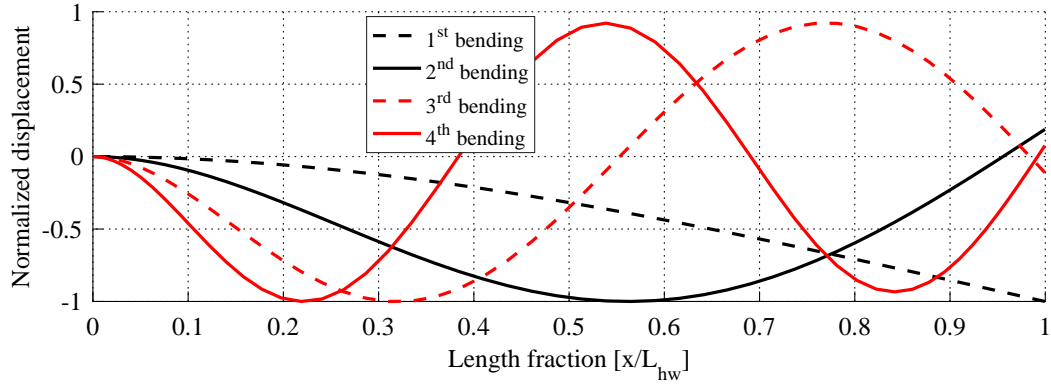
The main difference from the fixed wing PK method to the rotating wing PK method is the variation of velocity intensity along the length due Ωx . This makes the lift and moment vary along the length either, and also induces stiffening effect due the centrifugal force.

5.2.5 Modal analysis

The modal analyses were performed using eight hierarchical polynomials and two boundary terms. Fig. 5.5 shows the predicted vibration modes. Table 5.5 shows predicted frequencies.



(a) – Torsional modes.



(b) – Bending modes.

FIGURE 5.5 – Modes.

Modes	Bending	Torsion
1 st	2.28 Hz	25.52 Hz
2 nd	24.49 Hz	182.61 Hz
3 rd	76.88 Hz	359.47 Hz
4 th	159.12 Hz	537.72 Hz

TABLE 5.5 – Frequency response for each mode.

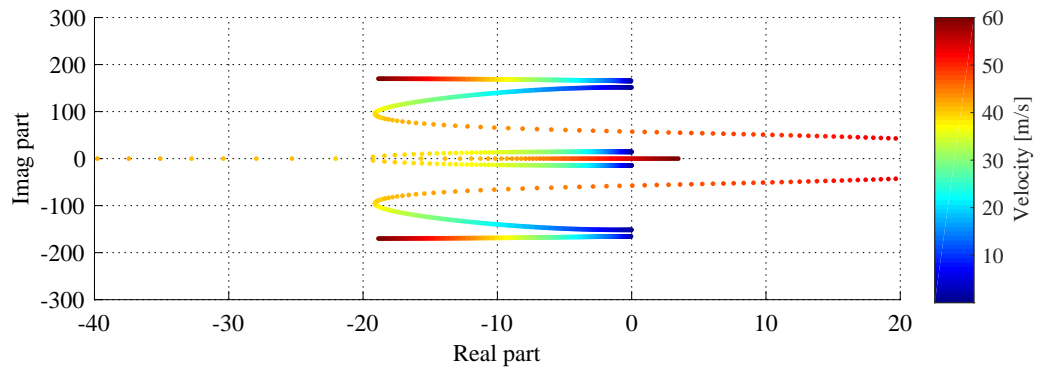
5.2.6 Aeroelastic analysis

This section presents the results obtained using the proposed model for the plate like wing aeroelastic system. The results are show in Fig. 5.6. The predicted flutter velocities is show in Table 5.6.

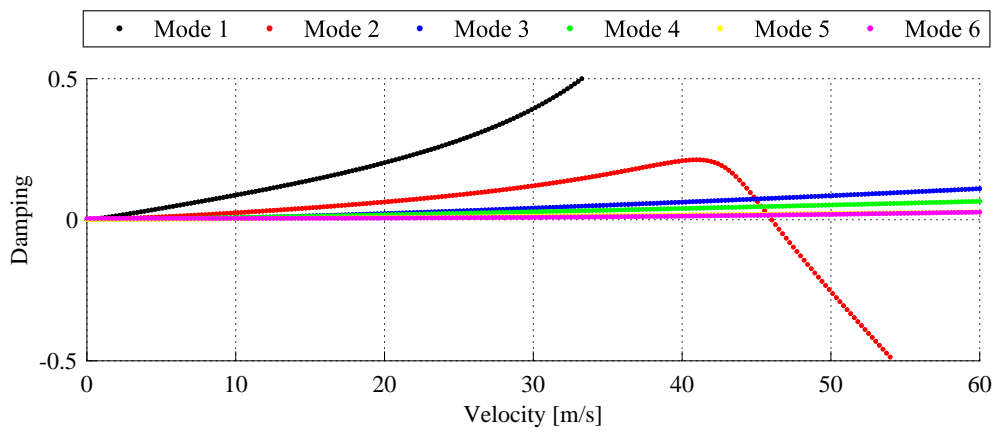
Predictions obtained using the proposed model correlate remarkably well with (RUGGERI, 2015) results, which proves the efficiency of the hierarchical Raleigh-Ritz method with lower computational cost.

Instability	(RUGGERI, 2015)	Present work
Flutter	46.54 m/s	46.02 m/s
Divergence	—	54.34 m/s

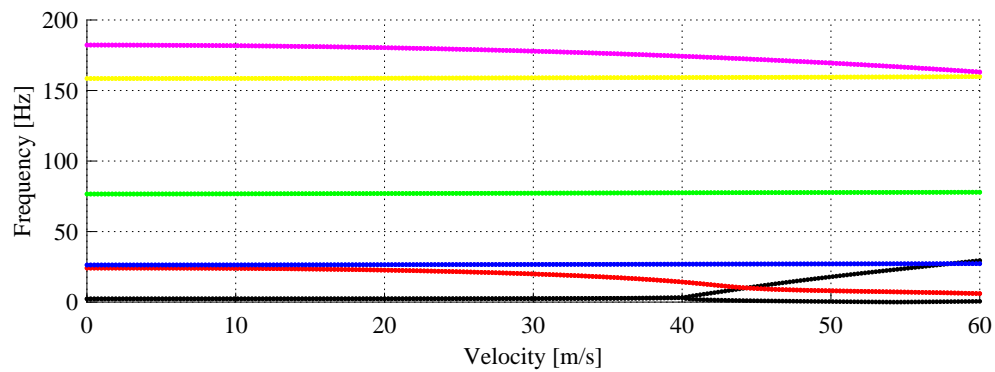
TABLE 5.6 – Aeroelastic results.



(a) – Root-loci.



(b) – Damping.



(c) – Frequency.

FIGURE 5.6 – Aeroelastic prediction of the half-wing where $d_{\text{offset}} = -5$ mm.

6 Conclusion

This work presented a hierarchical Rayleigh-Ritz based model to predict the flutter velocity in large wind turbine blades. The results predicted using the proposed model have been compared with results reported in the open literature for the SNL100-00 wind turbine blade. The results predicted using the proposed model in terms modal and flutter analyses agree fairly well with results reported by other authors in the open literature.

The model has successfully predicted the modal frequency to moderate displacements, considering its gravitational and centrifugal loads. It was concluded that the gravity has a negligible effect on the blade natural frequency, but while the rotation increases the centrifugal load presents a major effect on the natural frequency. The hierarchical Rayleigh-Ritz based model have also predicted with a good accuracy the natural frequencies and modes of a gas turbine blade developed in the work of (DONADON *et al.*, 2010) as predicted the flutter velocity of a fixed half-wing (RUGGERI, 2015) using Theodorsen function.

The aeroelastic representation using the PK method describe by (WRIGHT; COOPER, 2015) and the $c_{l,\alpha}$ and $a_{c,n}$ correction proposed by (YATES Jr, 1966) were employed to compute the aeroelastic flutter of the SNL 100-00 blade in rotation with Theodorsen's and Loewy's function. Theodorsen function does not considers the effect of shed vorticity of each blade, but by neglecting this effect the model converges perfectly for all rotational speeds. Loewy's function is more suitable for a wind turbine blade due the shed vorticity effect consideration, but it is difficult to ensure convergence using the PK method while the rotation increases. Based on these results it could be concluded that Theodorsen's and Loewy's aerodynamic models provide similar results for the cases where wind velocity is different from zero, where flutter velocity predictions obtained using Theodorsen's model lead to slightly more conservative results in comparison with Loewy's model. The simulations carried out using both model also indicate divergence immediately after flutter for the wind turbine blade studied herein. The semi-analytical model presented in the paper allows parametric studies at low computational cost, being suitable for blade design optimization of large wind turbine blades.

6.1 Future works

The suggested topics to improve the present work are:

- Develop a computational tool using the present model that can couple with other softwares available as NREL's PreComp and SNL's NuMAD which calculates the structural properties of the blade.
- Unify the present model with BEMT.
- Perform more tests in the model using different types of blades, mainly large and BTC blades.

Bibliography

AKSENCER, T.; AYDOGDU, M. Flapwise vibration of rotating composite beams. **Composite Structures**, Elsevier, v. 134, p. 672–679, 2015.

BARDELL, N. Free vibration analysis of a flat plate using the hierarchical finite element method. **Journal of Sound and Vibration**, v. 151, n. 2, p. 263–289, 1991.

BERG, J. C.; RESOR, B. R. **Numerical Manufacturing And Design Tool (NuMAD v2 . 0) for Wind Turbine Blades : User ' s Guide**. Albuquerque, New Mexico, 2012. 93 p.

BIR, G. **User's Guide to PreComp (Pre-Processor for Computing Composite Blade Properties)**. Golden, Colorado, 2005. 31 p.

BISHOP, R. E. D.; CANNON, S. M.; MIAO, S. On coupled bending and torsional vibration of uniform beams. **Journal of Sound and Vibration**, v. 131, n. 3, p. 457–464, 1989.

BISPLINGHOFF, R. L.; ASHLEY, H.; HALFMAN, R. L. **Aeroelasticity**. Toronto, Ontario: Addison-Wesley, 1955.

BOTTASSO, C.; CAMPAGNOLO, F.; CROCE, A.; TIBALDI, C. Optimization-based study of bend-twist coupled rotor blades for passive and integrated passive/active load alleviation. **Wind Energy**, Wiley Online Library, v. 16, n. 8, p. 1149–1166, aug 2012.

BRØNDSTED, P.; LILHOLT, H.; LYSTRUP, A. Composite materials for wind power turbine blades. **Annual Review of Materials Research**, Annual Reviews, v. 35, p. 505–538, 2005.

BURTON, T.; SHARPE, D.; JENKINS, N.; BOSSANYI, E. **Wind Energy Handbook**. Chichester: John Wiley & Sons, 2001.

CESNIK, C. E. S.; HODGES, D. H. VABS: A New Concept for Composite Rotor Blade Cross-Sectional Modeling. **Journal of the American Helicopter Society**, v. 42, n. 1, p. 27–38, 1997.

de MATOS JUNIOR, O. D.; DONADON, M. V.; CASTRO, S. G. P. Aeroelastic behavior of stiffened composite laminated panel with embedded SMA wire using the hierarchical Rayleigh-Ritz method. **Composite Structures**, Elsevier, v. 181, p. 26–45, 2017.

- DONADON, M. V.; BRINGHENTI, C.; MENEZES, J. C. the Stress Stiffening Effects on the Natural Frequencies. In: **Congresso Nacional de Engenharia Mecânica - CONEM**. Campina Grande - Paraíba: Associação Brasileira de Engenharia e Ciências Mecânicas - ABCM, 2010.
- DRELA, M. XFOIL: An analysis and design system for low Reynolds number airfoils. In: **Low Reynolds number aerodynamics**. [S.l.]: Springer, 1989. p. 1–12.
- FARSADI, T.; KAYRAN, A. Aeroelastic stability evaluation of bend-twist coupled composite wind turbine blades designed for load alleviation in wind turbine systems. In: **34th Wind Energy Symposium**. Reston, Virginia: American Institute of Aeronautics and Astronautics, 2016.
- FILIPPI, M.; CARRERA, E. Flutter analysis of fixed and rotary wings through a one-dimensional unified formulation. **Composite Structures**, Elsevier, v. 133, p. 381–389, 2015.
- FUNG, Y. C. **An introduction to the theory of aeroelasticity**. New York: Dover Publications, 1969.
- GOEIJ, W. de; TOOREN, M. van; BEUKERS, A. Implementation of bending-torsion coupling in the design of a wind-turbine rotor-blade. **Applied Energy**, Elsevier, v. 63, n. 3, p. 191–207, jul 1999.
- GRIFFITH, D. T.; ASHWILL, T. D. **The Sandia 100-meter All-glass Baseline Wind Turbine Blade : SNL100-00**. Albuquerque, New Mexico, 2011. 1–67 p.
- HANSEN, M. O.; SØRENSEN, J. N.; VOUTSINAS, S.; SØRENSEN, N.; MADSEN, H. A. State of the art in wind turbine aerodynamics and aeroelasticity. **Progress in Aerospace Sciences**, v. 42, n. 4, p. 285–330, 2006.
- HAYAT, K.; HA, S. K. Load mitigation of wind turbine blade by aeroelastic tailoring via unbalanced laminates composites. **Composite Structures**, Elsevier, v. 128, p. 122–133, sep 2015.
- HAYAT, K.; LECEA, A. G. M. de; MORIONES, C. D.; HA, S. K. Flutter performance of bend-twist coupled large-scale wind turbine blades. **Journal of Sound and Vibration**, Academic Press, v. 370, p. 149–162, may 2016.
- HODGES, D. H.; DOWELL, E. **Nonlinear equations of motion for the elastic bending and torsion of twisted nonuniform rotor blades**. Washington, D.C, 1974.
- LARWOOD, S.; SENCENBAUGH, J.; ACKER, B. Controlled Velocity Testing of an 8-kW Wind Turbine. In: **AWEA Windpower**. Washington, D.C: U.S. Department of Energy, 2001.
- LOBITZ, D.; LAINO, D. Load mitigation with twist-coupled HAWT blades. In: **37th Aerospace Sciences Meeting and Exhibit**. Reston, Virginia: American Institute of Aeronautics and Astronautics, 1999.
- LOBITZ, D. W. Aeroelastic stability predictions for a MW-sized blade. **Wind Energy**, Wiley Online Library, v. 7, n. 3, p. 211–224, 2004.

- LOBITZ, D. W.; ASHWILL, T. D. **Aeroelastic effects in the structural dynamic analysis of vertical axis wind turbines**. Albuquerque, NM (USA), 1986.
- LOEWY, R. G. A Two-Dimensional Approximation to the Unsteady Aerodynamics of Rotary Wings. **Journal of the Aeronautical Sciences**, v. 24, n. 2, p. 81–92, 1957.
- MALCOLM, D. J.; LAIRD, D. L. Extraction of equivalent beam properties from blade models. **Wind Energy**, Wiley Online Library, v. 10, n. 2, p. 135–157, 2007.
- MANWELL, J. F.; MCGOWAN, J. G.; ROGERS, A. L. **Wind energy explained: theory, design and application**. Chichester: John Wiley & Sons, 2009. 577 p.
- OWENS, B.; RESOR, B.; HURTADO, J.; GRIFFITH, D. T. **Impact of Modeling Approach on Flutter Predictions for Very Large Wind Turbine Blade Designs**. Albuquerque, New Mexico, 2013.
- POURAZARM, P.; MODARRES-SADEGHI, Y.; LACKNER, M. A parametric study of coupled-mode flutter for MW-size wind turbine blades. **Wind Energy**, Wiley Online Library, v. 19, n. 3, p. 497–514, 2016.
- RAFIEE, M.; NITZSCHE, F.; LABROSSE, M. Dynamics, vibration and control of rotating composite beams and blades: A critical review. **Thin-Walled Structures**, v. 119, n. January, p. 795–819, 2017.
- RAFIEE, R.; TAHANI, M.; MORADI, M. Simulation of aeroelastic behavior in a composite wind turbine blade. **Journal of Wind Engineering and Industrial Aerodynamics**, v. 151, p. 60–69, 2016.
- RESOR, B.; OWENS, B. C.; GRIFFITH, D. T. Aeroelastic Instability of Very Large Wind Turbine Blades. **European Wind Energy Conference and Exhibition 2006**, 2012.
- ROSTAMI, H.; Rahbar Ranji, A.; BAKHTIARI-NEJAD, F. Free in-plane vibration analysis of rotating rectangular orthotropic cantilever plates. **International Journal of Mechanical Sciences**, Pergamon, v. 115–116, p. 438–456, 2016.
- RUGGERI, M. C. **Development of methodologies of aeroelastic analysis for the design of flexible aircrafts wings**. 202 p. Tese (Master's dissertation) — Instituto Tecnológico de Aeronáutica - ITA, 2015.
- Sandia National Laboratories. **Offshore Wind RD&D: Large Offshore Rotor Development - Sandia Energy**. 2018. Disponível em: <<http://energy.sandia.gov/>>.
- SCHUBEL, P. J.; CROSSLEY, R. J. Wind turbine blade design. **Energies**, v. 5, n. 9, p. 3425–3449, 2012.
- SCOTT, S.; CAPUZZI, M.; LANGSTON, D.; BOSSANYI, E.; MCCANN, G.; WEAVER, P. M.; PIRRERA, A. Effects of aeroelastic tailoring on performance characteristics of wind turbine systems. **Renewable Energy**, Pergamon, v. 114, p. 887–903, dec 2017.
- SICARD, J.; SIROHI, J. Aeroelastic stability of a flexible ribbon rotor blade. **Journal of Fluids and Structures**, Elsevier, v. 67, n. April, p. 106–123, 2016.

WRIGHT, J. R.; COOPER, J. E. **Introduction to aircraft aeroelasticity and loads**. Chichester: John Wiley & Sons, 2015.

YATES Jr, E. C. Modified-strip-analysis method for predicting wing flutter at subsonic to hypersonic speeds. **Journal of Aircraft**, v. 3, n. 1, p. 25–29, 1966.

ZIENKIEWICZ, O. C.; GAGO, J. P. D. S. R.; KELLY, D. W. The hierarchical concept in finite element analysis. **Computers and Structures**, v. 16, n. 1-4, p. 53–65, 1983.

Appendix A - Hierarchical functions

A hierarchical function means that a increasing number of terms does not alter the shape functions (ZIENKIEWICZ *et al.*, 1983). The proposed shape functions to satisfy the essential boundary conditions are derived from the Rodrigues' form of the Legendre orthogonal polynomials (BARDELL, 1991; de MATOS JUNIOR *et al.*, 2017), as the recursive function is defined as follows,

$$\mathcal{N}_j^{\mathcal{V}}(\xi(x)) = \sum_{r=0}^{j/2} \frac{(-1)^r (2j-2r-7)!!}{2^r r! (j-2r-1)!} \xi(x)^{j-2r-1}, \quad j > 4 \quad (\text{A.1})$$

where \mathcal{V} refers to the displacement field of interest that can represent the u , w and β , "j" is the current term number, as $j!! = j(j-2) \cdots (2 \text{ or } 1)$, $0!! = (-1)!! = 1$ and $j/2$ denotes its own integer part and the non-dimensional coordinate $\xi(x) = (2x/R - 1)$. However the first four terms are:

$$\begin{aligned} \mathcal{N}_1^{\mathcal{V}}(\xi(x)) &= \frac{1}{2} - \frac{3}{4}\xi(x) + \frac{1}{4}\xi(x)^3 \\ \mathcal{N}_2^{\mathcal{V}}(\xi(x)) &= \frac{1}{8} - \frac{1}{8}\xi(x) - \frac{1}{8}\xi(x)^2 + \frac{1}{8}\xi(x)^3 \\ \mathcal{N}_3^{\mathcal{V}}(\xi(x)) &= \frac{1}{2} + \frac{3}{4}\xi(x) - \frac{1}{4}\xi(x)^3 \\ \mathcal{N}_4^{\mathcal{V}}(\xi(x)) &= -\frac{1}{8} - \frac{1}{8}\xi(x) + \frac{1}{8}\xi(x)^2 + \frac{1}{8}\xi(x)^3 \end{aligned} \quad (\text{A.2})$$

The first two terms correspond to the zero displacement and rotation of the one edge of the beam, respectively, as the other two is also a constrain of rotation and displacement in the other extreme edge, then as the present work correspond to a cantilever beam problem (one edge clamped and the other edge free) the first two terms are neglected.

Appendix B - Blade information

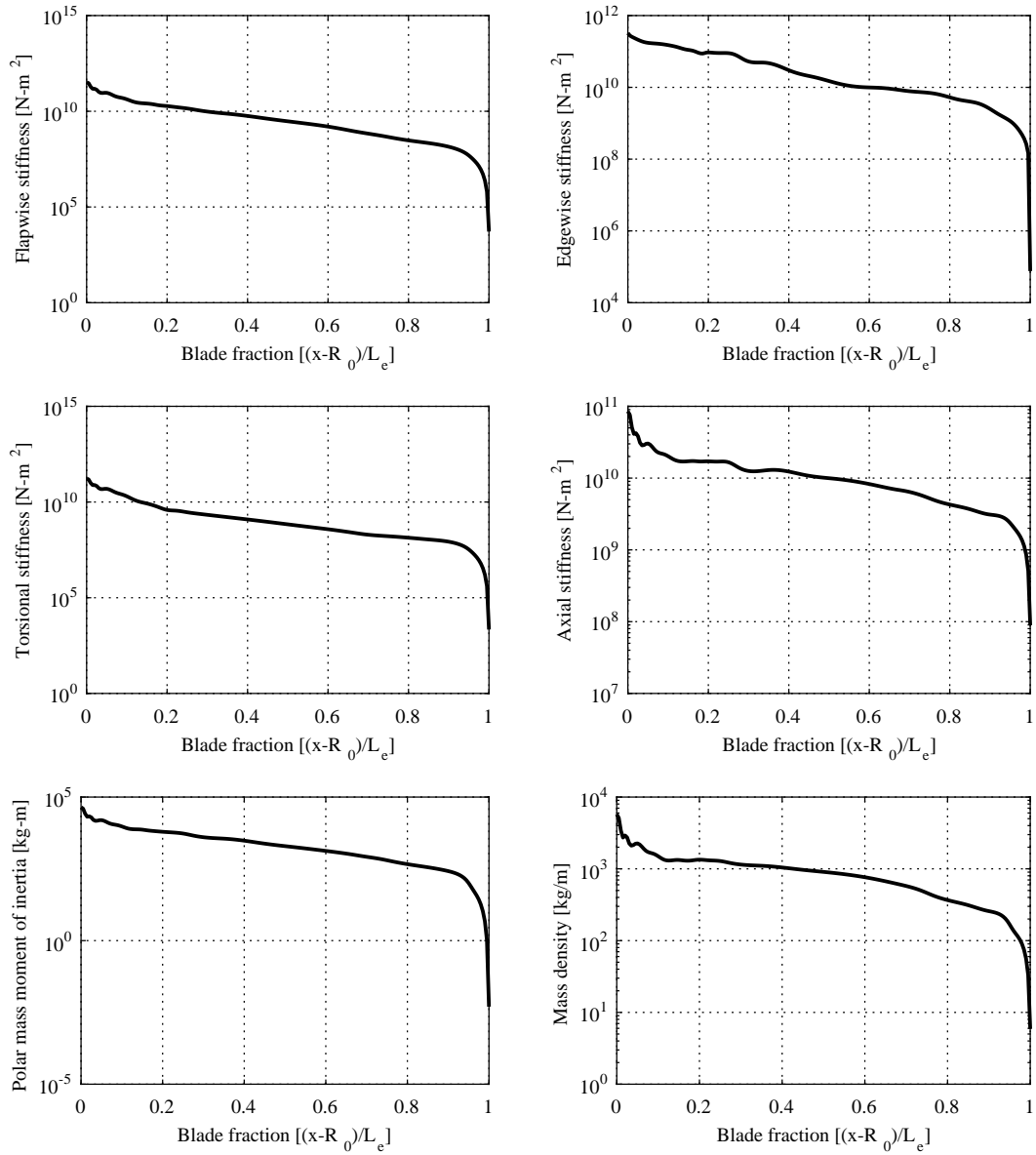


FIGURE B.1 – Inertial and mass properties.

The SNL100-00 blade properties obtained from the (Sandia National Laboratories, 2018) are shown in Figs. B.1 and B.2, its airfoil profiles used in each blade section are also provided in its website.

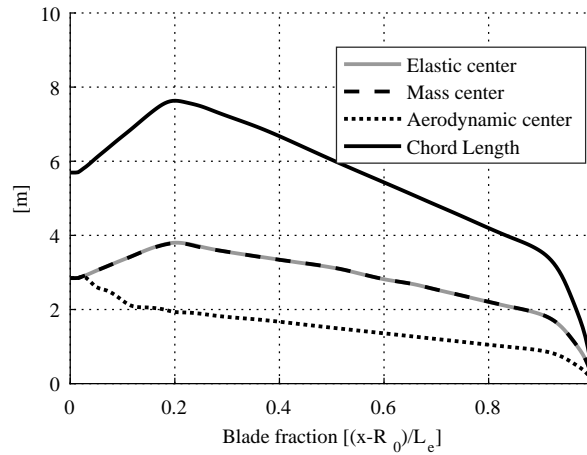


FIGURE B.2 – Geometric properties.

The cross-coupled stiffness properties, inertia properties, blade elastic center and mass center (Fig. B.1) of the SNL composite blade were computed using PreComp (BIR, 2005) (Pre-Processor for Computing Composite Blade Properties), developed by the National Renewable Energy Laboratory (NREL) as described in (OWENS *et al.*, 2013), other tools can be used to determine the effective section properties of a wind turbine composite blade (CESNIK; HODGES, 1997; MALCOLM; LAIRD, 2007). The present model also can be integrated with the SNL blade design tool NuMAD (BERG; RESOR, 2012) where it simplifies the process of creating a three-dimensional model of a wind turbine composite blade.

Fig. B.3 shows graphically the laminate placement and shear web locations for the data listed in Table B.1. The trailing edge reinforcement is highlighted in orange. The spar cap placement is highlighted in blue. The two principal shear webs are located to the top and bottom sides of the spar cap. The third shear web location is shown by the red line in Fig. B.3. The leading edge panel is defined as the gray area between the leading edge and the beginning of the spar cap. The aft panel is defined as the gray area between the spar cap and trailing edge reinforcement. The third shear web resides within the aft panel region.

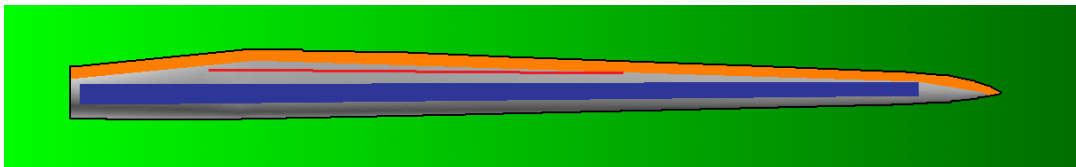


FIGURE B.3 – Planform of Sandia 100-m Baseline Blade with Laminate Designations (Blue: Spar Cap, Orange: trailing edge reinforcement, Red: Third Shear Web).

The amount of material use in the confection as the description of laminates/materials placement of the SNL blade is listed in Table B.2. The bill of materials summary is provided in Table B.3. The general properties of the SNL wind turbine are show in

Station Number	Blade Fraction	Root Buildup	Spar Cap	TE Reinforcement	LE Panel	Aft Panel
		Triax/EP-3	E-LT-5500/EP-3	E-LT-5500/EP-3, Foam	Foam	Foam
	(-)	(mm)	(mm)	(mm)	(mm)	(mm)
1	0.000	160				
2	0.005	140	1	1		
3	0.007	120	2	2		
4	0.009	100	3	3		
5	0.011	80	4	5		
6	0.013	70	10	7	1	1
7	0.024	63	13	8	3.5	3.5
8	0.026	55	13	9	13	13
9	0.047	40	20	13, 0	30	100
10	0.068	25	30	18, 0	50	100
11	0.089	15	51	25, 60	60	100
12	0.114	5	68	33, 60	60	100
13	0.146	*	94	40, 60	60	100
14	0.163		111	50, 60	60	60
15	0.179		119	60, 60	60	60
16	0.195		136	60, 60	60	60
17	0.222		136	60, 60	60	60
18	0.249		136	60, 60	60	60
19	0.277		128	30, 40	60	60
20	0.358		119	30, 40	60	60
21	0.439		111	15, 20	60	60
22	0.521		102	8, 10	60	60
23	0.602		85	4, 10	60	60
24	0.667		68	4, 10	60	60
25	0.683		64	4, 10	55	55
26	0.732		47	4, 10	45	45
27	0.765		34	4, 10	30	30
28	0.846		17	4, 10	15	15
29	0.895		9	4, 10	10	10
30	0.944		5	4, 10	5	*
31	0.957		5	4, 10	5	
32	0.972		5	4, 10	5	
33	0.986		5	4, 10	5	
34	1.000		*	*	*	

TABLE B.1 – Laminate Schedule for Sandia 100-m Baseline Blade (* indicates termination)

Table B.4. More information about the blade can be found in (GRIFFITH; ASHWILL, 2011).

Material	Usage/Location	Mass (kg)	Percent blade mass
E-LT-5500/EP-3	Spar caps, trailing edge reinforcement	49,527	42.8 %
SNL Triax	Root build-up, internal & external surfaces	38,908	33.6 %
Foam	Core panels, shear webs	15,333	13.3 %
Extra Resin	extra weight (interior surface)	6,863	5.9 %
Saertex/EP-3	Shear webs	4,112	3.6 %
Gelcoat	Coating	920	0.8 %

TABLE B.2 – Materials Usage Summary for Sandia 100-m Baseline Blade.

Material	Description	Mass (kg)	Percent blade mass
E-LT-5500	Uni-axial Fiberglass	37,647	32.5 %
Saertex	Double Bias Fiberglass	10,045	8.7 %
EP-3	Resin	51,718	44.7 %
Foam	Foam	15,333	13.3 %
Gelcoat	Coating	920	0.8 %

TABLE B.3 – Bill of Materials for Sandia 100-m Baseline Blade.

Property	Value
Rotor radius (R)	102.5 m
Hub radius (R_0)	2.5 m
Number of blades	3
Blade mass	114,172 kg
Class	IB
Max rotor speed	7.44 rpm
Rated wind speed	11.3 m/s
Cut-in	3 m/s
Cut-out	25 m/s

TABLE B.4 – General SNL wind turbine properties.

Appendix C - Blade airfoil sections curve slope

The SNL100-00 geometry shape can be seen in Fig. C.1. It can be seen that each section has different airfoil and chord length, then to compute $c_{l,\alpha}$ the software X-foil was used (DRELA, 1989), to extract each $C_l \times \alpha$ for each blade station with different Ω 's. the first step is to setup the air properties as show in Table C.1.

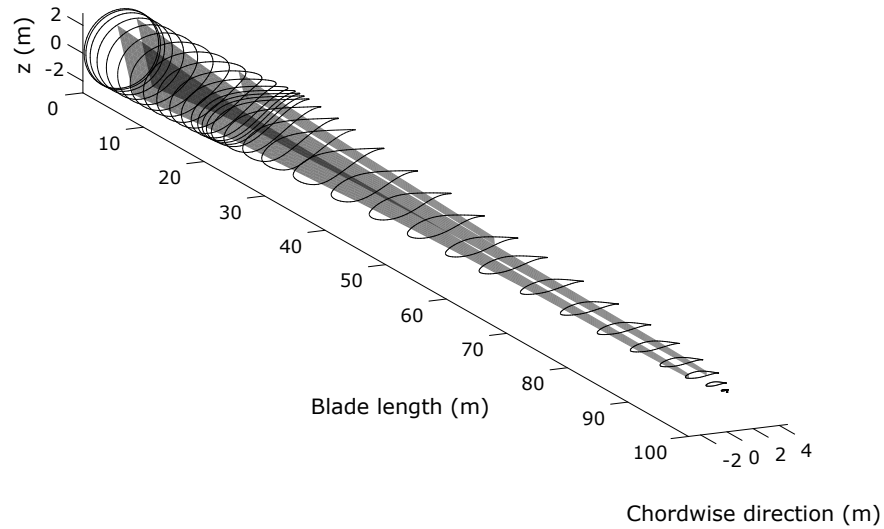


FIGURE C.1 – Geometric shape of the SNL100-00 blade.

TABLE C.1 – Parameters of the air.

Air density (ρ_f)	1.225 kg/m ³
Dynamic viscosity of the air (ν_f)	18.27E-6 Pa.s
Specific gas constant (R_{spec})	0.287E+3 J/(kg.K)
Boltzmann constant (κ)	1.4
Temperature (T_e)	288.15 K

It is also needed the chord length (c_y) of each blade station that is show in Table C.2.

Then it is calculated the Mach number (Ma) and Reynolds number (Re),

$$Ma = \frac{V_{rel}}{\sqrt{\kappa R_{spec} T_e}} \quad (C.1)$$

$$Re = \frac{\rho_f V_{rel} c_y}{\mathbf{v}_f} \quad (C.2)$$

The Reynolds and Mach number for the current blade are show in Figs. C.2 and C.3.

The curve slope ($C_{l,\alpha}$) were calculated by varying the angle of attack (α) from 0° to 6° for each airfoil section and applying a linear regression. Xfoil provides the values of C_l for each α then by employing a linear regression to obtain a first order polynomial function and deriving it gets $C_{l,\alpha}$ as shown,

$$C_l = \alpha C_{l,\alpha} + cte \implies \frac{\partial C_l}{\partial \alpha} = C_{l,\alpha} \quad (C.3)$$

All the $C_{l,\alpha}$'s with its local Ma and Re are shown in Fig. C.4.

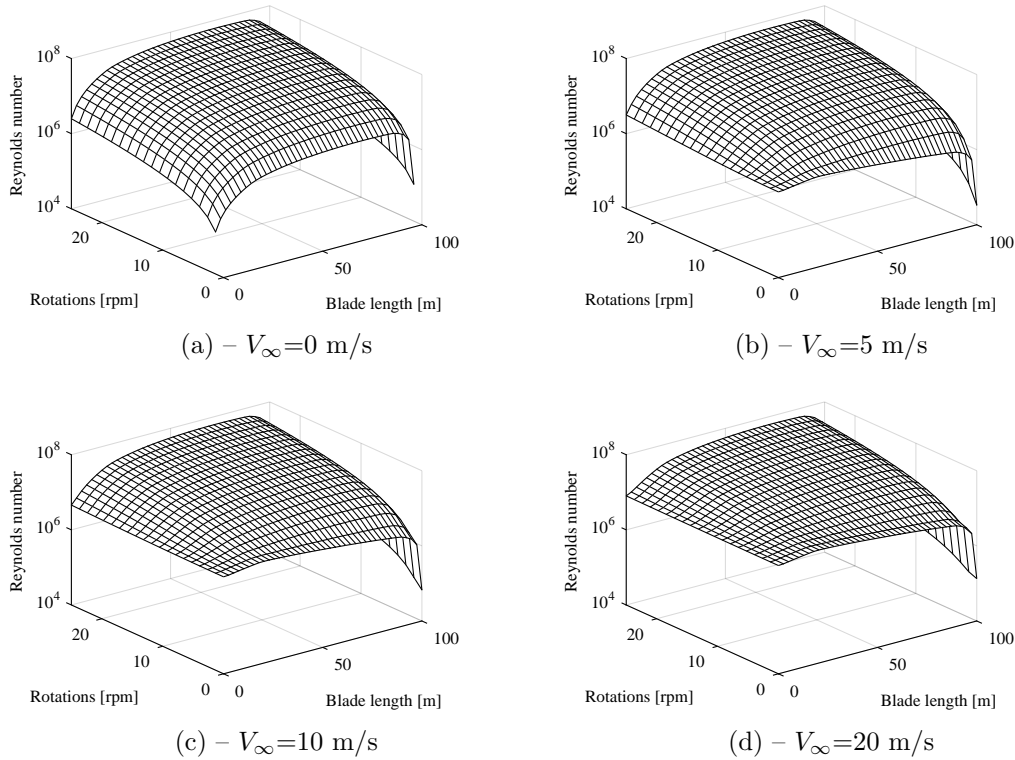


FIGURE C.2 – Reynolds number.

TABLE C.2 – Sandia 100-m Baseline Blade Airfoil and Chord Properties.

Station Number	Blade Fraction	Chord (m)	Pre-twist (deg)	Pitch Axis (Fraction)	Airfoil Description
1	0.000	5.694	13.308	0.500	Cylinder
2	0.005	5.694	13.308	0.500	Cylinder
3	0.007	5.694	13.308	0.500	Transition (99.25%)
4	0.009	5.694	13.308	0.500	Transition (98.5%)
5	0.011	5.694	13.308	0.500	Transition (97.75%)
6	0.013	5.694	13.308	0.500	Ellipse (97%)
7	0.024	5.792	13.308	0.499	Ellipse (93.1%)
8	0.026	5.811	13.308	0.498	Ellipse (92.5%)
9	0.047	6.058	13.308	0.483	Transition (84%)
10	0.068	6.304	13.308	0.468	Transition (76%)
11	0.089	6.551	13.308	0.453	Transition (68%)
12	0.114	6.835	13.308	0.435	Transition (60%)
13	0.146	7.215	13.308	0.410	Transition (51%)
14	0.163	7.404	13.177	0.400	Transition (47%)
15	0.179	7.552	13.046	0.390	Transition (43.5%)
16	0.195	7.628	12.915	0.380	DU99-W-405
17	0.222	7.585	12.133	0.378	DU99-W-405 (38%)
18	0.249	7.488	11.350	0.377	DU99-W-350 (36%)
19	0.276	7.347	10.568	0.375	DU99-W-350 (34%)
20	0.358	6.923	9.166	0.375	DU97-W-300
21	0.439	6.429	7.688	0.375	DU91-W2-250 (26%)
22	0.520	5.915	6.180	0.375	DU93-W-210 (23%)
23	0.602	5.417	4.743	0.375	DU93-W-210
24	0.667	5.019	3.633	0.375	NACA-64-618 (19%)
25	0.683	4.920	3.383	0.375	NACA-64-618 (18.5%)
26	0.732	4.621	2.735	0.375	NACA-64-618
27	0.764	4.422	2.348	0.375	NACA-64-618
28	0.846	3.925	1.380	0.375	NACA-64-618
29	0.894	3.619	0.799	0.375	NACA-64-618
30	0.943	2.824	0.280	0.375	NACA-64-618
31	0.957	2.375	0.210	0.375	NACA-64-618
32	0.972	1.836	0.140	0.375	NACA-64-618
33	0.986	1.208	0.070	0.375	NACA-64-618
34	1.000	0.100	0.000	0.375	NACA-64-618

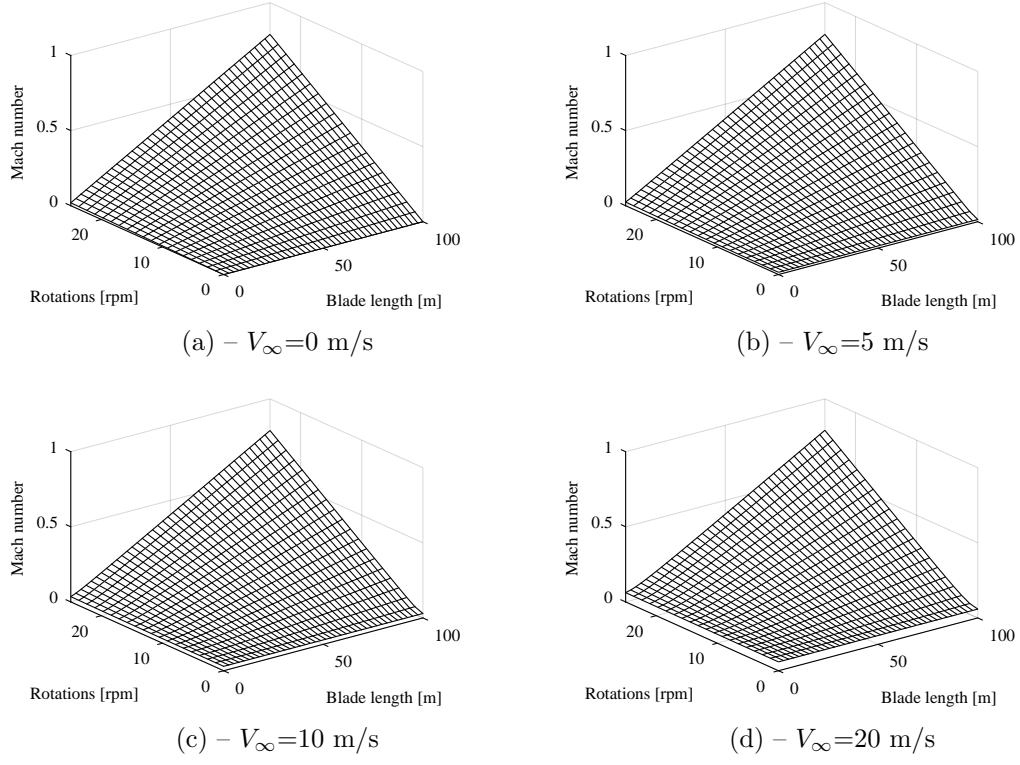


FIGURE C.3 – Mach number.

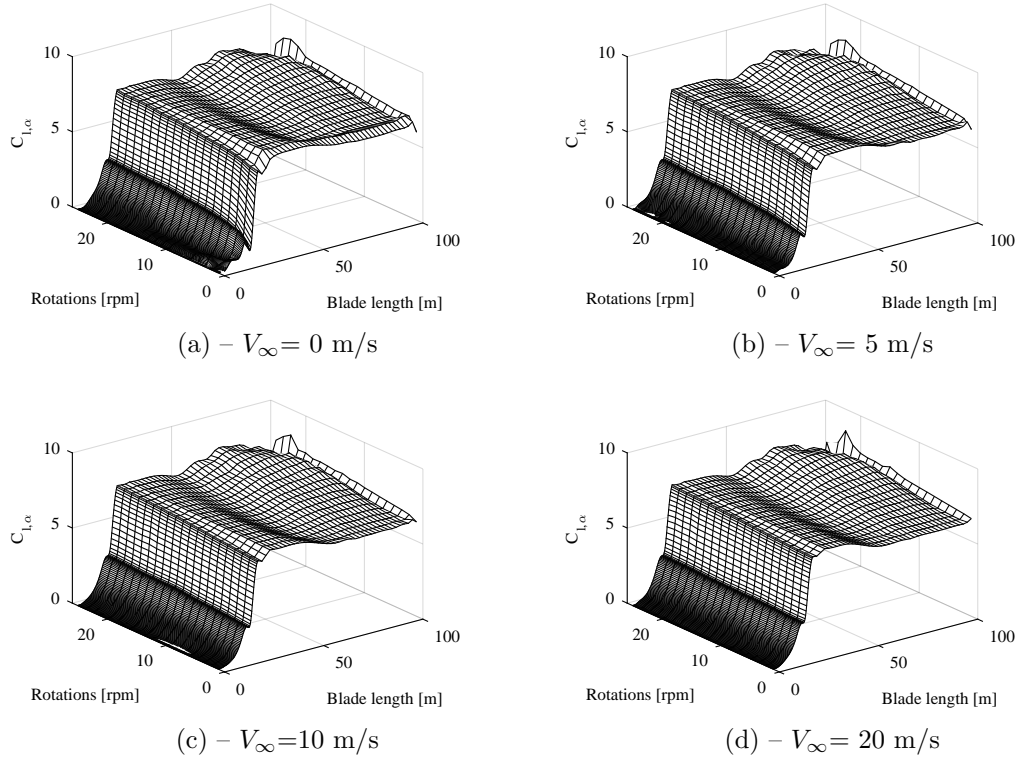


FIGURE C.4 – Curve slopes.

FOLHA DE REGISTRO DO DOCUMENTO

1. CLASSIFICAÇÃO/TIPO DM	2. DATA 17 de dezembro de 2018	3. DOCUMENTO Nº DCTA/ITA/DM-018/2015	4. Nº DE PÁGINAS 85
5. TÍTULO E SUBTÍTULO: A hierarchical Rayleigh-Ritz based model for aeroelastic analysis of wind turbine blades			
6. AUTOR(ES): Gustavo Monteiro Farias			
7. INSTITUIÇÃO(ÕES)/ÓRGÃO(S) INTERNO(S)/DIVISÃO(ÕES): Instituto Tecnológico de Aeronáutica – ITA			
8. PALAVRAS-CHAVE SUGERIDAS PELO AUTOR: Hierarchical Rayleigh-Ritz; Aeroelastic analysis; Wind turbine blades			
9. PALAVRAS-CHAVE RESULTANTES DE INDEXAÇÃO: Hierarchical Rayleigh-Ritz; Aeroelastic analysis; Wind turbine blades			
10. APRESENTAÇÃO: (X) Nacional () Internacional ITA, São José dos Campos. Curso de Mestrado. Programa de Pós-Graduação em Engenharia Aeronáutica e Mecânica. Área de Projeto Aeronáutico, Estruturas e Sistemas Aeroespaciais. Orientador: Prof. Dr. Maurício Vicente Donadon. Coorientador: Prof. Dr. Roberto Gil Annes da Silva. Defesa em 20/11/2018. Publicada em 2018.			
11. RESUMO: O presente trabalho propõe um modelo de Rayleigh-Ritz hierárquico para análise da resposta aeroelástica de pás de aerogeradores. A pá é modelada como uma viga em balanço, o modelo estrutural leva em consideração as pre-cargas induzidas pelas forças centrífugas e gravitacionais. A formulação é baseada no princípio de Hamilton combinado com o método de Rayleigh-Ritz. Um modelo aerodinâmico não estacionário é utilizado para calcular o incremento das forças aerodinâmicas no domínio da frequência utilizando as funções de Theodorsen e Loewy. A solução resultante de um problema de autovalor é baseado no método PK. A ocorrência do <i>flutter</i> aeroelástico é observada nos diagramas $\Omega - \omega$ e $\Omega - g$ em função da rotação das pás e da velocidade do vento. Os resultados numéricos previstos utilizando o modelo semi-analítico proposto foram comparados com resultados numéricos reportados na literatura para a pá projetada por Sandia National Laboratories, confeccionada em fibra de vidro e de 100 metros de comprimento. No geral uma boa concordância entre as previsões obtidas utilizando o modelo proposto e os resultados reportados na literatura foi obtida.			
12. GRAU DE SIGILO: (X) OSTENSIVO () RESERVADO () SECRETO			